STRAIN INHOMOGENEITIES DURING PLASTICITY AND CREEP OF METALS: REPRESENTATIVE VOLUME ELEMENTS AND MICROSCALE STRAIN PREDICTIONS

BY

RENATO BICHARA VIEIRA

DISSERTATION

Submitted in partial fulfillment of the requirements
for the degree of Doctor of Philosophy in Aerospace Engineering
in the Graduate College of the
University of Illinois Urbana-Champaign, 2021

Urbana, Illinois

Doctoral Committee:

Professor John Lambros, Chair and Director of Research
Professor Ioannis Chasiotis
Professor Huck Beng Chew
Professor Huseyin Sehitoglu

Abstract

This work investigated microscale strain inhomogeneities during plasticity and creep of an austenitic stainless steel alloy, namely stainless steel 709. Digital image correlation (DIC) was employed to experimentally measure strain fields at the microstructural level (defined as a level comparable to the grain scale) and combined with electron backscatter diffraction (EBSD) data of the microstructure. The overarching goal of this work was to investigate the dependence of such microscale strain inhomogeneities on loading type, on temperature, and on microstructural parameters.

The first part of this work explored the microscale response of austenitic stainless steel 709 to plasticity and creep loading. Macroscale experiments were performed in which far-field load-displacement data and in situ DIC measurements were made. These macroscale experiments were used to determine specific loading conditions to be investigated in more detail with high resolution microscale measurements. Subsequently, a high-resolution digital image correlation technique (HiDIC) was successfully applied to measure strain fields at the grain level of samples subjected to plasticity and creep loading conditions over a range of maximum stresses, temperatures (room temperature, 300°C, 500°C, 650°C), and hold times (from 15 s to 30 min). The measured microscale strain fields were compared, and showed that both creep and plasticity produce similar highly inhomogeneous strain fields. Furthermore, localization of strains primarily near grain boundaries was observed for all cases investigated, with no visible difference in the patterns of strain accumulation for creep and plasticity.

In the second part of this work, the strain-based representative volume element (RVE) resulting from the plastic and creep loading of alloy 709 samples was explored. The RVE is a key concept behind homogenization techniques used to correlate microscale behavior with macroscale

(i.e., far-field) response of the material. Therefore knowledge of the RVE size is an essential piece in many multiscale modeling frameworks. A robust experimental method to measure the strain-based RVE size from HiDIC microscale strain fields was developed through the exploration of the statistical nature of the RVE. The proposed stereological approach takes randomly selected boxes from within a measured strain field and determines the statistical distribution of the size of the strain-based RVE from the average strains for different box sizes. The proposed method was then applied to measure strain-based RVE sizes on samples subjected to creep and plasticity loading conditions, over a range of temperatures (room temperature, 300°C, 500°C, and 800°C), maximum stresses (25% below and 25% above yield strength) and hold times (5 min to 1 h), with the relationship between the loading conditions and the strain-based RVE size being explored. Through a relevant coordinate transformation, local strain accumulations near grain boundaries (mantle regions) were resolved and their correlation to the strain-based RVE size was also explored. Samples with higher local normal to shear strain ratios were seen to have larger strain-based RVE sizes. The reason that both the RVE size and the local normal to shear strain ratios near grain boundaries behave in s similar fashion is because that are both controlled by the same underlying deformation mechanisms.

In the final part of this work, a methodology for applying neural-network algorithms to predict microscale strain fields was employed. The approach used each correlation point from HiDIC strain fields as an input data point for the training of a neural network, allowing for a large quantity of training data (up to 70,000 data points in each case) to be obtained from a relatively small number of experiments. The grain boundary inclination angle to the loading direction was shown to be a good predictor for the average residual strain accumulated inside the mantle regions (i.e., near grain boundaries) for all cases investigated, even when used as the sole input parameter.

Acknowledgments

I am very grateful to a number of people who have supported me during my time as a Ph.D. student at the University of Illinois. Professor John Lambros was an exceptional advisor, from whom I have learned a lot more than just how to properly conduct research and analysis. He taught me how to focus on what matters and to not doubt your own work. I will always carry his life teachings with me.

During the development of a large portion of my studies, Professor Huseyin Sehitoglu provided valuable insight during our research group weekly meetings, and I am very grateful for that. I also want to thank my committee members Professor Ioannis Chasiotis and Professor Huck Beng Chew, for pointing out the paths I should pursue and how I should pursue them. Their observations were essential for the development of the final work.

Thanks to Peter Kurath for all the indispensable help setting up and running the majority of all my experiments conducted at the Advanced Materials Testing and Evaluation Laboratory (AMTEL). I also need to thank C.Q Chen, from whom I have learned a lot about scanning electron microscopes and how to use them at the Material Research Laboratory (MRL). This research was performed in part using funding received from the Department of Energy Office of Nuclear Energy's Nuclear Energy University Program under grant number DE-NE0008436 (Project number 15-8432). This material is based upon work supported by the National Science Foundation under Grant No. CMMI 18-25466.

All the labmates I had during these years played an important role, be it in helping with research or helping with everything else. Sidharth Ravi has a special place among them for being present the whole time, for all the conversations and insights into graduate student life. I also need to remember Robert Waymel, Manue Martinez, Arthur Ding, Raeann VanSickle, David Foehring,

Devanjith Fonseka, Franco Cubas, Samuel Fayad, Yiguang Zhang and Raymundo Barrios, for all the good times in the lab and out of it.

Last, but not least, I owe a great deal to my family. The older I get the more I recognize how fundamental my parents were in molding my character. They taught me the value of education and encouraged me all the way to the finish line. I would not have made it without their constant support. My girlfriend deserves immense recognition for enduring the long distance relationship and for all the encouragement, the daily talks and for helping me stay connected to aspects of my life other than work. Too many friends have been fundamental for the entire process, I am extremely grateful to have the best friends anyone could ask for.

Table of Contents

List of Figures

List of Tables

Chapter 1: Introduction

Through both experimental and numerical efforts, highly inhomogeneous deformation has been widely observed to occur at the microscale (grain and sub-grain scale) of polycrystalline metals during plasticity and creep (e.g., Delaire et al., 2000). Such heterogeneity can ultimately be attributed to the underlying mechanisms of deformation that govern the interactions between anisotropic grains. Furthermore, it is increasingly accepted that the inhomogeneous microscale response of a metal during deformation is the driving force behind its macroscale response, damage accumulation, and eventual failure. Thus, the development of mechanism-based models capable of predicting macroscopic behavior requires the fundamental understanding of the microscopic behavior and its dependence on microstructural factors (e.g., grain boundaries, misorientation angles, grain sizes etc.) as well as loading conditions (e.g., stress, temperature, hold times etc.).

1.1 Background

1.1.1 Microscale Strain Inhomogeneities in Plasticity and Creep

Many authors have explored the inhomogeneous strain fields arising at the microscale of polycrystalline metals, with a majority of existing studies concerning the response of these materials to plastic and fatigue loading. Delaire et al. (2000) used a grid-based technique to measure the strain field at the grain scale of a copper sample made of a single layer of grains. After plastic deformation, they compared the measured strains with finite element simulation predictions from a physically-based model for the deformation of centered cubic crystals. Raabe et al. (2001) used Digital Image Correlation (DIC) to achieve the same goal of comparing finite element simulation predictions with experimental strain measurements for a plastically loaded

polycrystalline aluminum sample with a quasi-2D single layer of coarse grains. Bartali et al. (2009) performed *in situ* microscopic DIC measurements of strain evolution during low-cycle fatigue of a duplex stainless steel, and made observations on the micromechanisms of fatigue damage accumulation. Walley et al. (2010) used a scanning electron microscope to obtain *in situ* images for DIC strain measurements during quasi-isostatic room temperature tensile tests of a nickel-based superalloy and related the inhomogeneous strain field with grain orientations. Padilla et al. (2012) used DIC to measure strain fields at the microscale of highly texturized zirconium, the statistical correlation between crystal orientation (Schmid factors) and inhomogeneities in the strain fields. Abuzaid et al. (2012) used DIC to measure strain fields at the microscale of a plastically loaded nickel superalloy, studying the correlation between crystal orientations and accumulation of strains near grain boundaries. Carroll et al. (2013) used the same DIC technique from (Abuzaid et al., 2012) to study the interactions between grain-boundary strain accumulation and fatigue crack nucleation. Di Gioacchino and Quinta da Fonseca (2013) applied an SEM-based DIC technique to capture the formation of slip bands during the plastic deformation of stainless steel. Mello et al. (2017) also used an SEM-based DIC technique to measure strains at the grain scale of a Ni-based superalloy during cyclic loading at different temperatures, reporting a deformation mechanisms map based on those results.

The above is only a short listing, the ones most relevant to the present study, of the numerous such efforts that exist for the investigation of grain-scale response under plastic loading. In contrast, far fewer authors have explored the development of microscale strain fields during creep loading. Parker and Stratford (1996) estimated strains from the change in shape of grains observed before and after creep loading of a 1.25Cr 0.5Mo steel, recognizing that the strains were heterogeneous and pointing to microstructural parameters (such as grain size and precipitates) as

the culprits for strain localization. Carter et al. (2012) applied an *in situ* SEM-based DIC technique to measure the strain evolution with time during creep loading of multiple Ni-based superalloys, heat treated to produce different microstructures. They made observations on the dominant creep mechanisms behind deformation of each sample and correlated the different characteristics of the microstructure with a change in in mechanism. Slone and Mills (2016) used an *ex situ* SEM-based DIC technique to measure strains at the microscale of another Ni-based superalloy, reporting that high angle grain boundaries presented preferential spots for strain accumulation during creep. Since ultimately both plasticity and creep are related through the microstructural mechanisms active in both, in the present effort both are of concern.

With the goal of producing predictive models based on the microscale response of a material, the relationship between the inhomogeneous microscale strain fields and the macroscale behavior of the material is also of importance (Raabe et al., 2001). One way of relating results from the different length scales is through the use of homogenization techniques, largely based on the concept of the Representative Volume Element (RVE). The RVE can be understood as the smallest volume of material capable of reproducing the average value of some property of the bulk material (Hill, 1963). Therefore, a study on the nature of the RVE and its size under plasticity and creep loading conditions is discussed in the present work.

1.1.2 Digital Image Correlation

Throughout all chapters of this work, the experimental technique of digital image correlation (DIC) is used extensively. Two dimensional DIC is a technique capable of producing full-filed in-plane displacement and strain measurements by comparing digital images taken from the surface of a sample before and after deformation. A brief review on the general application of

this technique is presented here. For more details on the specifics of the correlation algorithm the reader is referred to Sutton et al. (1983, 2009).

The DIC technique tracks the displacement of markers on the surface of a specimen between two images acquired one before and one after deformation. Full-field measurement is achieved by tracking multiple markers placed randomly throughout the surface in what is usually referred to as a random speckle pattern. Fig. 1.1 shows an example of a random speckle pattern for DIC. No scale bar is shown in this figure, because DIC is a scale-less method, which means that no matter the scale of the random speckle pattern, the correlation will still work the same way and calculate the displacements in pixel units provided that a speckle pattern of sufficient quality is present.

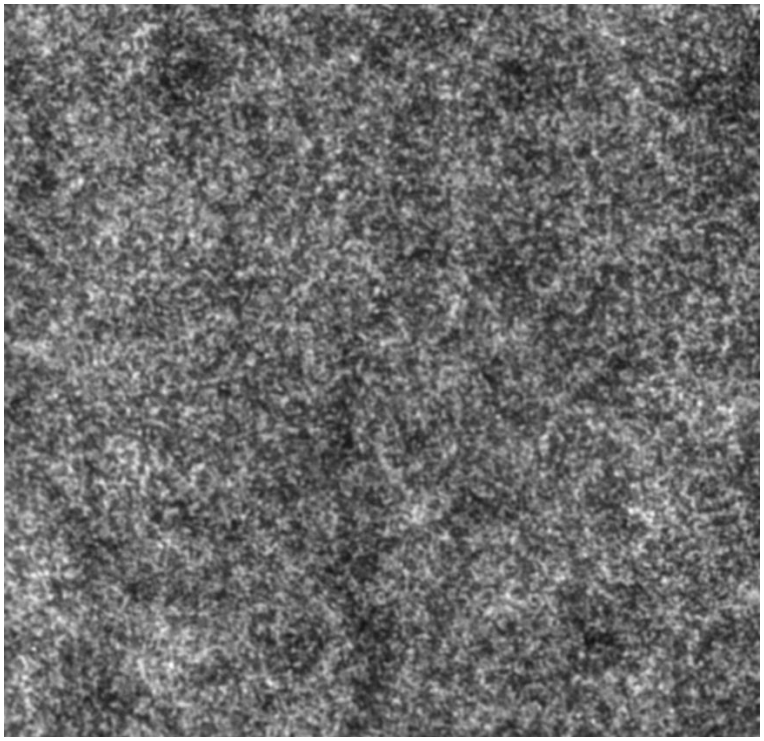

Fig. 1.1. Example of a DIC random speckle pattern.

Since pixel intensity values are clearly not unique within an image, DIC tracks the average gray level inside square groupings of pixels, called *subsets*. This approach is usually referred to as

"local DIC", as opposed to the "global DIC" approach in which the minimization process of tracking the average gray levels is done over the entire region of interest through a finite element mesh (Hild and Roux, 2012)). In local DIC, after defining the subsets on the reference (undeformed) image of the surface, optimization techniques are used to find the best matching subset in the deformed image, resulting in a displacement vector assigned to the center of that subset, referred to as the correlation point. Correlation of each subset is done individually, making the local DIC approach robust to speckle pattern inaccuracies, although since each correlation is done individually on each subset, compatibility is not necessarily guaranteed (unlike the global DIC approach). Fig. 1.2 helps in the understanding of how local DIC maps a subset to its deformed location in order to produce a displacement measurement for each correlation point (the center point of each subset). Assuming a homogeneously deforming subset, the location of an arbitrary point within the deformed subset ($\tilde{x}$,$\tilde{y}$) is given by an expansion around the center point, *P*, of the reference subset (x_0,y_0), such that:

$$\tilde{x} = x_0 + u_0 + \frac{\partial u}{\partial x}\Delta x + \frac{\partial u}{\partial y}\Delta y + \frac{1}{2}\frac{\partial^2 u}{\partial x^2}\Delta x^2 + \frac{1}{2}\frac{\partial^2 u}{\partial y^2}\Delta y^2 + \frac{\partial^2 u}{\partial x \partial y}\Delta x \Delta y, \tag{1.1}$$

$$\tilde{y} = y_0 + v_0 + \frac{\partial v}{\partial x}\Delta x + \frac{\partial v}{\partial y}\Delta y + \frac{1}{2}\frac{\partial^2 v}{\partial x^2}\Delta x^2 + \frac{1}{2}\frac{\partial^2 v}{\partial y^2}\Delta y^2 + \frac{\partial^2 v}{\partial x \partial y}\Delta x \Delta y, \tag{1.2}$$

where (*x*,*y*) are the coordinates of the point in the reference frame, *u* and *v* are the horizontal and vertical displacements, respectively, u_0 and v_0 are the horizontal and vertical displacements of the center point, and $\Delta x = x - x_0$, $\Delta y = y - y_0$. The presence of displacement derivatives in the expansions of eq. 1.1 and eq. 1.2 allow the deformed subset to change shape according to material deformation, without necessarily remaining a square, as can be seen in Fig. 1.2.

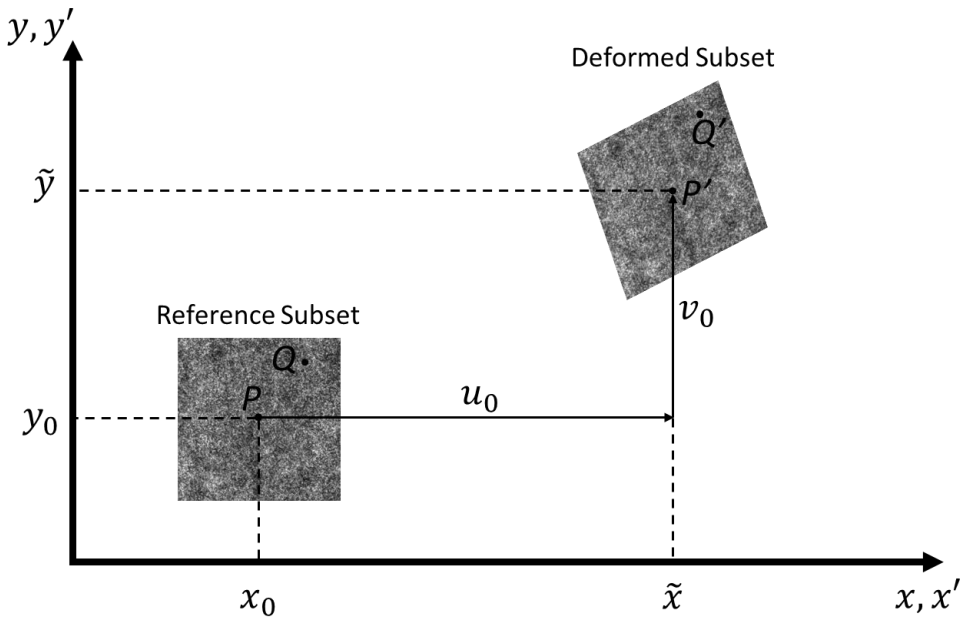

Fig. 1.2. DIC subset mapping to determine displacement for each correlation point

Since each subset results in a single correlation point, to which the displacement measurement is assigned, it is clear that the measurement resolution of DIC is controlled by the size of the subset. However, since the size of the subset is not a fixed parameter, DIC does not have an inherent length scale, which makes it an ideal technique for multiscale applications. The limiting factors that determine the length scale of DIC measurements are the resolution of the correlated images (size of a pixel) and the suitability of the speckle pattern applied to the surface of the specimen, with a successful DIC correlation requiring at least three speckles inside each subset (Sutton et al., 2009), which places a lower bound on the size of the subset for a given speckle pattern. The fundamental assumptions of the local DIC approach are that the pixel intensities (gray levels) are unchanged during deformation and that the deformation inside each subset is homogeneous (eq. 1.1 and 1.2).

All the DIC results discussed in this work were obtained using the commercially available Vic2D software which has default values for subset sizes ranging from 21 x 21 pixels to 201 x 201

pixels. Larger subsets sizes result in more speckles inside each subset, which makes the correlation more robust. The density of correlation points is determined by the spacing between subset centers (step size), which usually ranges from 5 to 25 pixels in each direction, allowing adjacent subsets to overlap significantly. Because of this overlap, there is a connection between the subset size and the spatial resolution of the displacement measurements from DIC, with larger subsets resulting in lower resolutions. The recommended ratio between step size and subset size is around 1:4 (a subset size of 101 by 101 pixels would go along a step size of 25 pixels) (Sutton et al., 2009). Thus, the subset size is a function of the size of the speckles in the speckle pattern and the resolution of images taken of the surface, and it indirectly determines both the spatial resolution of displacement measurements from DIC and the density of correlation points. After correlation, the displacements are differentiated to obtain the components of strain, which are used in all chapters of this work.

1.2 Objectives

The overall objective of this work is to study the inhomogeneous microscale strain fields resulting from plasticity and creep deformation of a polycrystalline metal under a range of different loading conditions, including changes in temperature, maximum stress and hold times. Understanding the differences between these strain fields and their dependence on microstructural and loading parameters will aid in the eventual development of corresponding predictive models. The specific objectives of this work are to:

1. Study the inhomogeneous microscale strain accumulation patterns formed during creep and plasticity loading of a polycrystalline stainless steel alloy, especially in the vicinity of grain boundaries. The formation of such heterogeneities in likely controlled by the underlying deformation mechanisms and thus could be a function of loading type (creep vs. plasticity). Here we want to explore whether different loading types produce different

microscale strain inhomogeneity patterns, and to investigate their possible differences and similarities. To accomplish this, an ultra-high-resolution Digital Image Correlation (HiDIC) technique was applied to measure the microscale strain fields, which are then aligned to microstructural data obtained from Electron Backscatter Diffraction (EBSD) scans. Experiments at both room temperature and at elevated temperatures were conducted and the resulting microscale strain fields are compared and contrasted.

2. Investigate the relationship between the accumulation of residual strains, during plasticity and creep, and microstructural features. Different microstructural features are known to have an effect on the deformation mechanisms that control the response of a polycrystalline material, and thus could also have an effect on the microscale strain accumulation patterns. The experimentally measured strain fields are rotated into local grain-boundary coordinates, allowing for better visualization of the response of the material to deformation at regions in the vicinity of grain boundaries. The influence of microstructural parameters, such as grain-boundary misorientation angle and grain-boundary inclination with respect to the loading axes, is explored.

3. Study the possible dependence of the strain-based Representative Volume Element (RVE) on loading and its relation to strain concentrations in the vicinity of grain boundaries. Although the RVE is often used as a deterministic quantity, it is statistical in nature and could possibly depend on both type and amount of loading. Here we want to explore if and how the RVE size (or distribution) depends on both different type of loading (e.g., creep vs. plasticity) and loading conditions (e.g., temperature, stress level, hold time). A new robust method of experimentally measuring strain-based RVEs is proposed and applied to measure the resulting strain-based RVE in samples subjected to

creep and plasticity loading, with a range of different maximum stresses, temperatures and hold times.

4. Predict microscale plastic strain fields directly from experimental data, through the use of a neural-network algorithm, avoiding highly complex and computation-heavy crystal plasticity simulations. With sufficient experimental training data, a machine learning algorithm such as a neural network should have enough information on the relationships between microstructural parameters and the patterns of strain accumulation to generate good prediction. A new approach in the use of neural networks for material microscale response prediction is proposed, where each experimental measurement point from the combined DIC-EBSD dataset is used as an input in the training of a fitting neural network, essentially obtaining a very large quantity of data points from a single experiment.

1.3 Thesis Outline

This section provides an overview of the work presented in each chapter of this thesis. Chapter 2 presents a brief study of the macroscale response of an austenitic stainless steel to plasticity, creep and creep-fatigue loading, serving as a baseline and starting point for the microscale study that follows. Chapter 3 presents the initial study of the microscale response of the material to plasticity, creep and creep-fatigue loading, both at room temperature and at 650°C. The high resolution DIC (HiDIC) technique introduced in chapter 3, along with the improvements to its alignment procedure to EBSD data, are used throughout all the following chapters to measure residual strain fields at the grain scale of the austenitic stainless steel alloy. Chapter 4 introduces the concept of the strain-based RVE as a means of comparing different strain fields and their underlying degree of inhomogeneity. A new method of measuring strain-based RVEs is proposed

and its robustness is compared to previous methods, showing that it is capable of producing more reliable RVE measurements. In Chapter 5, the RVE-measurement method proposed in Chapter 4 is used to measure RVE sizes from residual strain fields obtained from samples loaded with different temperatures, maximum stresses and hold times, making it possible quantitatively compare strain fields resulting from plasticity and creep. A coordinate transformation is applied to the residual strain fields so that strains in the vicinity of grain boundaries can be observed in a coordinate frame with tangential and normal (to the grain boundary) components. This transformation allows for easier exploration of the relationship between the microstructure and strain accumulation patterns, with a correlation between strain-based RVE sizes and the normal to shear strain ratio near grain boundaries being reported. Chapter 6 builds upon observations from chapter 5, where grain boundary inclination angle was found to have high correlation with strain accumulation near grain boundaries, to propose a single-input neural-network approach for predicting strains in the vicinity of grain boundaries. Finally, Chapter 7 presents the final conclusions and suggestions for future work.

Chapter 2: Macroscale Creep-Fatigue Response of an Austenitic Stainless Steel

This chapter presents a brief study of the macroscopic response of austenitic stainless steel 709 to plasticity and creep-fatigue loading. It serves as a baseline for the microscale studies that follow in Chapters 3, 4, 5 and 6.

2.1 Stainless Steel 709

The material investigated in all experiments presented throughout this work is the stainless steel alloy 709, a relatively new alloy that is being considered as a candidate for applications in sodium fast reactors by the US Department of Energy (DOE). Alloy 709 is a highly alloyed austenitic stainless steel with macroscopic behavior similar to the well-known 316 stainless steel, but with improved properties, especially under high temperatures. Table 2.1 shows the composition of the as received batch of stainless steel 709 (Heat #011594) (Porter et al., 2021), while Fig. 2.1 shows a typical microstructure as obtained from: (a) an optical image of an etched sample and (b) an Electron Backscatter Diffraction (EBSD) scan, with no preferential direction or texture observed in the microstructure. Fig. 2.1c shows the distribution of grain-boundary misorientation angles, with prevalent Σ3 boundaries. Both the sample preparation for EBSD and the etching procedures used to obtain images such as those shown in the figure are described later on in section 3.1. Fig. 2.2 shows the resulting grain size distribution obtained from the EBSD scans, using the standard line intercept method of Mtex, an open source Matlab toolbox for EBSD analysis (Hielscher and Schaeben, 2008).

Table 2.1. Composition of stainless steel 709 (Heat #011594) (wt. pct.).

Heat ID	C	Mn	Si	Ni	Cr	Mo	Ti	Nb	N	S	P	B
011594	0.078	0.9	0.39	25.01	19.89	1.51	<0.01	0.25	0.14	0.0006	<0.005	0.0037

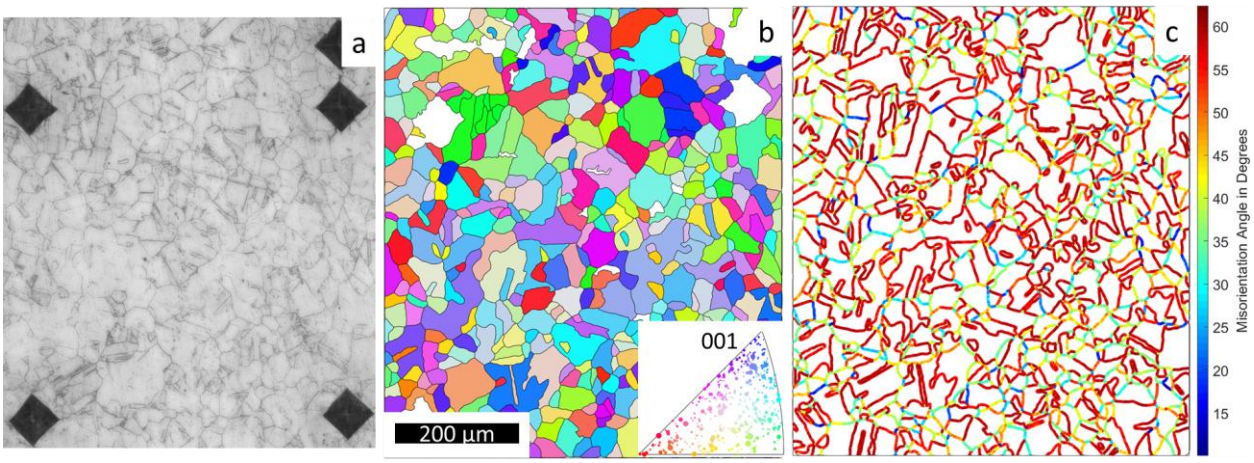

Fig. 2.1. (a) Typical optical image of etched surface; (b) Typical EBSD scan result, colored by first Euler angle; and (c) Grain boundaries colored by misorientation angle.

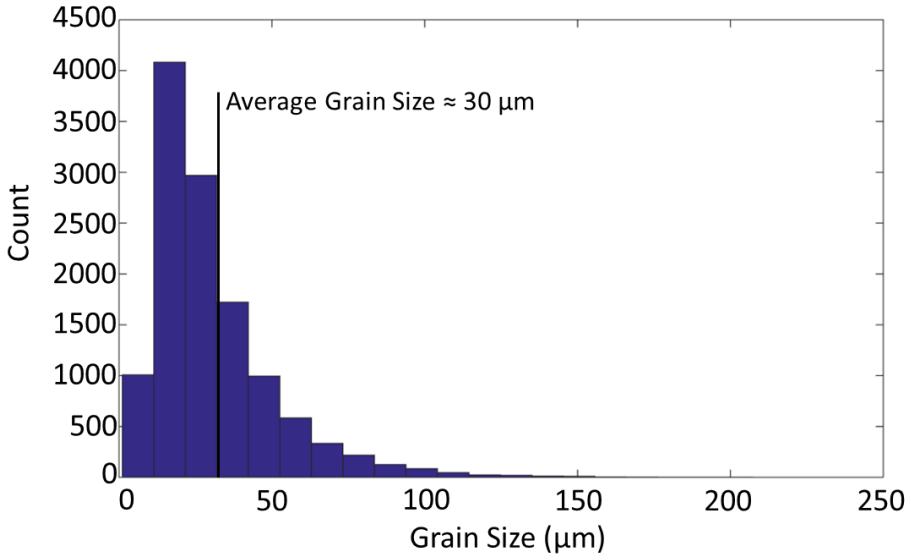

Fig. 2.2. Grain size distribution for stainless steel 709.

Even though the as received material did not present any preferential direction or texture in its microstructure, all samples were machined along the rolling direction of the bulk material through electrical discharge machining (EDM). Two sample geometries were used for the experiments presented throughout all the chapters of this work. Fig. 2.3 shows drawings for both the (a) hourglass and (b) dog-bone sample geometries. The hourglass geometry was used in all experiments where the accumulation of strains (and damage) at a controlled region of interest was

desired. Because of its short gauge and overall length, the hourglass sample geometry also allows for better control of temperature during long tests. The dog-bone geometry was used for all experiments where uniform spatial distributions of stresses and temperatures were needed (e.g., to obtain uniaxial stress-strain curves). Because of its long and thin gage length, the dog-bone geometry is very susceptible to buckling and therefore not a viable option for experiments where compression was present.

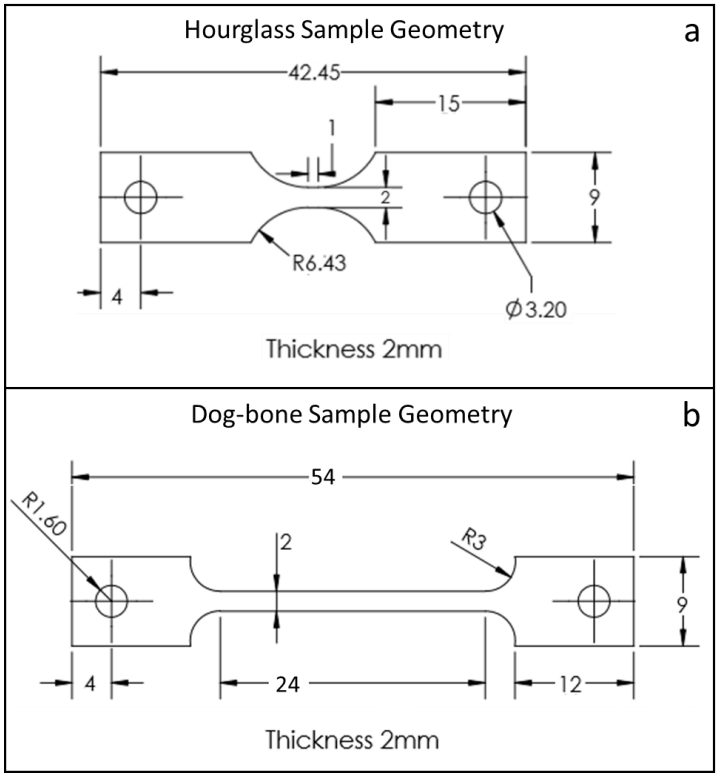

Fig. 2.3. (a) Drawing of the hourglass sample geometry; (b) drawing of the dog-bone sample geometry.

2.2 Experimental Setup

All samples had the front and back surfaces polished using a crystallographic polishing machine with silicon carbide disks of grits 200 and 600. The front surface had further polishing steps applied to it for experiments where EBSD or high-resolution Digital Image Correlation

(HiDIC) was used, with more specific sample preparation being discussed in Chapter 3. For all samples that were tested at high temperature a matte black coating (VHT Flameproof Coating, Flat Finish) was applied to the back surface, allowing for non-contact temperature measurements through an infrared (IR) thermometer. The micro-epsilon thermometer CTLaser with CF2 lens was used for all temperature measurements. The IR thermometer's factory calibration was verified through an experiment with simultaneous thermocouple and infrared temperature measurements, on a sample heated from room temperature to 850°C.

All the tensile, creep, and fatigue experiments shown in this work were performed using an Instron servo-hydraulic machine, equipped with a 4 KN load cell. Fig. 2.4 shows the experimental set up used for all experiments, with the IR thermometer marked as A, the induction heater (LEPEL 5 KW) marked as B, a camera and lens set used for *in situ* DIC strain measurements (PointGrey 1.4 Megapixels CCD camera with 12x Navitar HD lens) marked as C, the cooled grips (Instron) and custom loading fixtures marked as D, and the custom made induction heater coil wrapped around the sample marked as E. The schematic drawing to the right of the photo shows how the sample was placed inside the coil, with gaps between the central turns to allow for *in situ* DIC and infrared temperature measurements of the front and back surfaces, respectively.

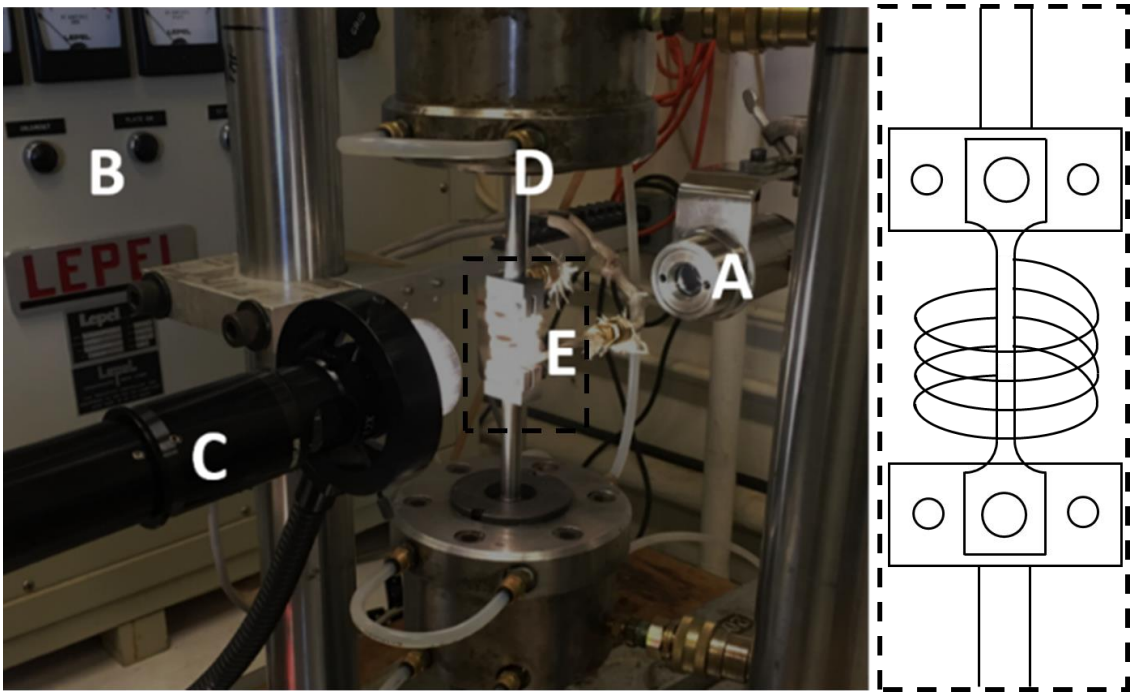

Fig. 2.4. Loading frame set up. A – Infrared thermometer; B – Induction heater; C – *In situ* DIC camera and lens; D – Cooled grips and custom loading fixtures; E – Induction heater coil around sample (as shown in schematic to the right).

2.3 Macroscopic Response of Alloy 709

Investigations on the macroscopic tensile properties of stainless steel 709 have been published in the literature. Naoi et al. (1993) authored the technical report from Nippon Steel, the initial developers of the alloy. Brnic et al. (2010) presented a series of macroscopic experimental results for uniaxial tensile and creep experiments under temperatures ranging from -70°C to 600°C. More recently, Ding et al. (2019) conducted a series of uniaxial tensile tests and studied the effect of aging on the microstructure and mechanical properties of alloy 709. Fig. 2.5 shows stress vs. strain curves obtained in the present work for four stainless steel 709 dog-bone samples, as shown in Fig. 2.3b, loaded at room temperature (RT), 300°C, 500°C and 650°C. The figure also shows a table with mechanical properties obtained from these experiments. The samples were loaded under displacement control with a strain rate of 0.05% s^{-1}. The yield strength, ultimate strength and

maximum strain values obtained agree with what is reported in the literature. The serrated flow observed during plastic deformation has also been reported by previous authors, being attributed to dynamic strain aging resulting from the interaction between solute atoms and moving dislocations during deformation (Ding et al., 2019).

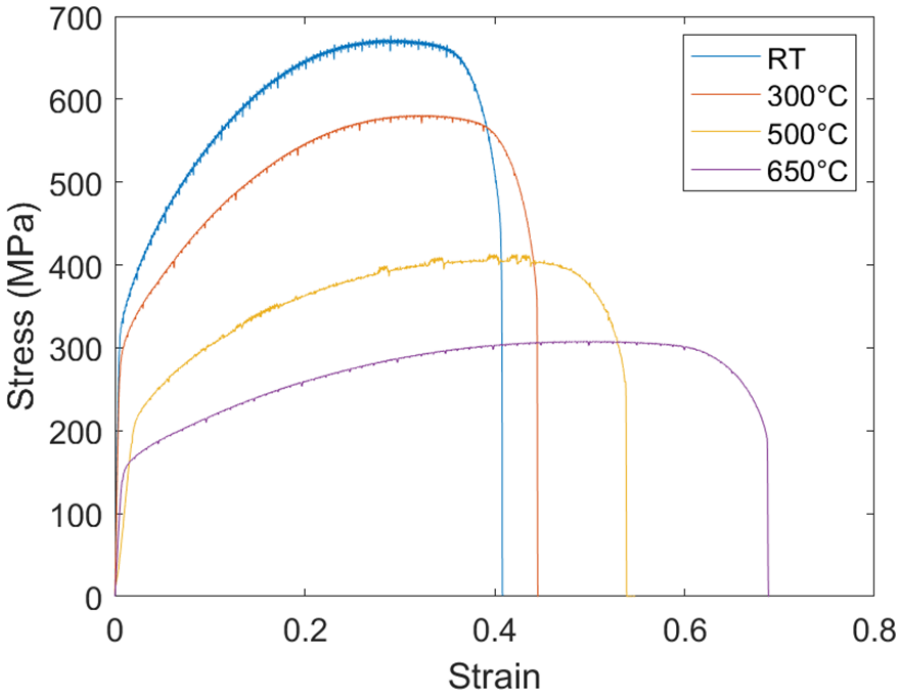

Temperature (°C)	Yield Strength (MPa)	Ultimate Strength (MPa)	Failure Strain (mm/mm)
RT	315	685	0.41
300	285	590	0.44
500	200	400	0.54
650	155	305	0.69

Fig. 2.5. Stress vs. strain curves for stainless steel 709 dog-bone samples loaded at: Room temperature (RT), 300°C, 500°C and 650°C.

2.3.1 Hold Times and Creep

The creep response of alloy 709 has also been discussed previously in the literature. Zhao et al. (2011) investigated the microstructural evolution and corresponding change in hardness

during creep of alloy 709 at 650°C, finding that creep deformation was responsible for elongating the grains which the authors related to an observed increase in hardness. Yi et al. (2019) studied the short-term (ranging from 1h to 400h) creep response of alloy 709 at 700°C, 750°C and 800°C. They also applied a new creep model they had proposed in an earlier study to predict the long-term creep response from the short-term data, finding that 650°C would be the maximum applicable temperature if the 60 years creep rupture strength required is at least 100 MPa. Taylor et al. (2019) studied the creep response of alloy 709 at 700°C loaded at stresses ranging from 125-250 MPa, finding that at these loading conditions the material presented "brief primary creep, an insignificant secondary creep and a prolonged tertiary creep stage". They also investigated the resulting creep failure surfaces using scanning electron microscopy and optical microscopy, observing ductile failure surfaces with dimple-like features resulting from microvoid coalescence and transgranular cracking.

A brief study of macroscopic creep response was also conducted in the present work, before proceeding to the study of the microscopic behavior. The introduction of hold times at maximum stress during a stress-controlled uniaxial tensile experiment allows us to study how strains accumulate during creep. Motivated by the work of Taylor et al. (2019), we initially concentrated mainly on the primary creep regime. Fig. 2.6 shows stress vs. strain curves for two alloy 709 dog-bone samples loaded in stress control at room temperature (RT) and at 650°C. The sample loaded at RT was loaded up to 500 MPa (~60% above yield at RT) and was held there for 1800 seconds. The sample loaded at 650°C was loaded up to 250 MPa (~60% above yield at 650°C) and held for 120 seconds. The curves show how during the hold time, both samples accumulated some amount of strain, meaning that for stresses above yield alloy 709 experiences (plastic) creep even at RT. The thick portion of the lines indicate the period during which the stress was held at maximum,

and it is clear that the sample loaded at 650°C accumulated more strain during 120 s than the sample loaded at RT did in 1800 s, indicating, as expected, that higher temperatures promote higher creep deformation.

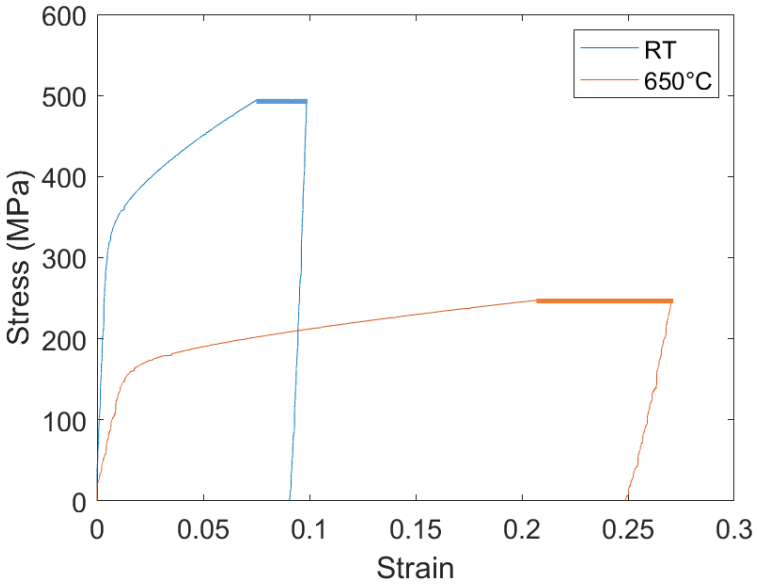

Fig. 2.6. Stress vs. stain curves for two dog-bone alloy 709 samples loaded at room temperature and 650°C, with 1800 s and 120 s hold times at maximum stress, respectively (the thick portion of the curve indicates the hold period).

To illustrate secondary and tertiary creep regimes and to better observe the effect of temperature on the creep behavior of alloy 709, longer hold times were considered. Fig. 2.7a shows the displacement vs. time curves obtained for two hourglass samples loaded at RT and 650°C. The maximum stresses were again 500 MPa for the RT sample and 250 MPa for the 650°C sample. The curves show that for these loading conditions, the RT sample deforms faster at the start of hold, with the 650°C samples overtaking it during the tertiary creep stage. This result might seem counterintuitive at first, but can be explained by the difference in maximum stresses. Fig. 2.7b shows the compliance (strain/stress) evolution with time, to account for this difference in maximum stress, resulting in a much more intuitive result that clearly shows that creep at 650°C is much more severe (deformation occurs at much higher rate) than at RT. After 10.5 h of hold

time the 650°C sample was well within tertiary creep stage (it failed after about 11 h), while the RT sample was still within the secondary creep stage (the RT sample did not fail). Here, as these are results from an hourglass sample, the strain values used to calculate compliance were obtained by dividing the machine displacement by a length value (18.5mm). This length was obtained through a calibration done by matching *in situ* DIC strains with the machine displacement divided by a length.

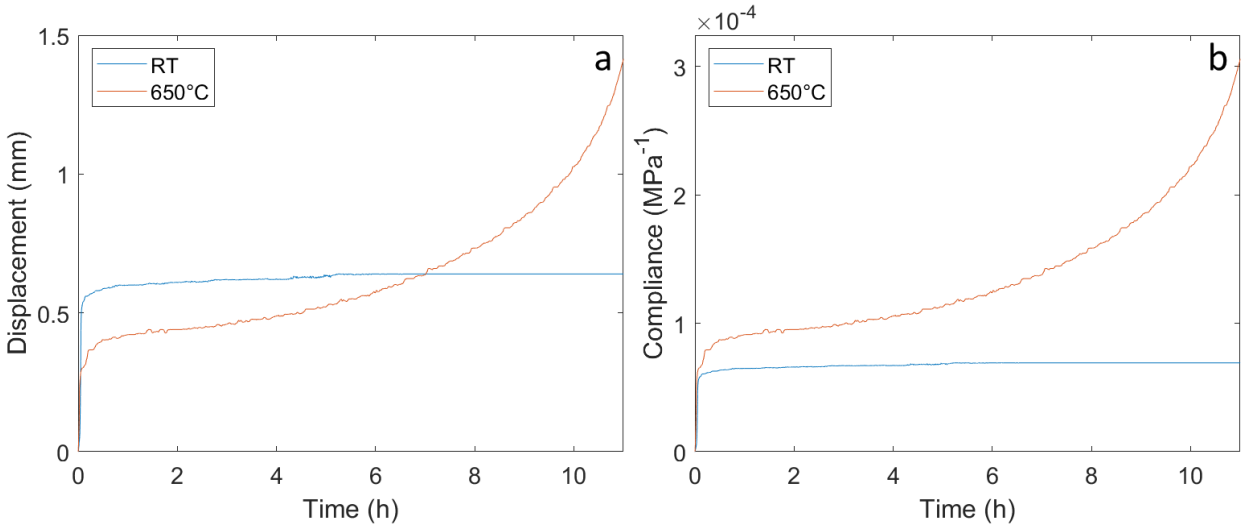

Fig. 2.7. (a) Displacement vs. time curve for two hourglass samples loaded at RT and 650°C, with maximum stresses of 500 MPa and 250 MPa, respectively; (b) Compliance vs. time curves for the same samples.

The primary creep response was studied more closely using a separate series of hourglass samples loaded with hold times ranging from 30 to 900 seconds, effectively producing a detailed view of the initial part of the curves shown in Fig. 2.7b. Fig. 2.8 shows the results obtained for the creep compliance (here strains from *in situ* DIC divided by maximum stress) during creep deformation of 10 hourglass samples, loaded at RT and 650°C with maximum stresses of 500 MPa and 250 MPa, respectively. Here, the strains prior to the start of hold (during plastic deformation) have been subtracted from the results, which is why the curves start at 0 creep compliance for 0 s hold time. Again, the results shown the expected trend that creep at 650°C produces a higher

deformation rate than at RT. The results from these experiments helped us in specifying how long the hold times should be during the creep-fatigue experiments that follow. A hold time of 60 s was determined as the best balance between being able to capture a reasonable amount of short term creep deformation and keeping creep-fatigue experiments at a feasible length (longer hold times would result in longer cycles).

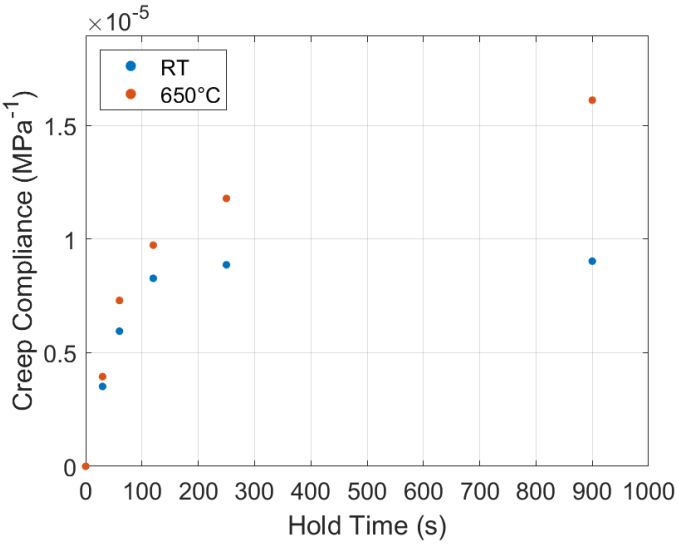

Fig. 2.8. Creep compliance vs. hold time for hourglass samples loaded at RT and 650°C with maximum stresses of 500 MPa and 250 MPa, respectively.

2.3.2 Creep-Fatigue

As with creep, the creep-fatigue response of stainless steel 709 has also been the object of previous study. Shaber et al. (2019) measured creep-fatigue crack growth rates in alloy 709 samples loaded at 550°C, 600°C and 700°C, with hold times of 0 s, 60 s and 600 s, reporting that crack growth rates exhibited very low sensitivity to different loading conditions, with the hold time of 600 s resulting in a crack growth rate only 2 times as fast as the 0 s experiments (the 60 s experiments were even closer to the results from 0 s). Lall et al. (2019) presented a comprehensive experimental evaluation of the creep-fatigue response of alloy 709 at 750°C, loading samples inside a scanning electron microscope which allowed them to study the microstructural evolution

of the material during creep-fatigue. Their results indicated that with lower hold time (60 s) cracks mainly propagated in a transgranular fashion, while at higher hold times (1 hour) intergranular cavitation dominates the crack growth. Alsmadi et al. (2020) and Alsmadi and Murty (2021) investigated the effects of hold times and strain range on the creep-fatigue life of alloy 709 samples loaded at 750°C, reporting a creep-fatigue interaction diagram (Creep damage vs. Fatigue damage), based on linear damage summation, which showed high levels of creep-fatigue interaction in alloy 709 (failure points fall below the ideal failure criterion). Appendix A presents a study on the creep-fatigue behavior of alloy 709 conducted in the context of the present work, in which the physically-motivated model developed by Neu and Sehitoglu (1989) is applied to model the material's creep-fatigue response.

The cyclic short-term creep response of alloy 709 was also explored here. Two hourglass samples were cyclically loaded at RT and 650°C, at maximum stresses of 500 MPa and 250 MPa respectively, and with 60 s hold times at maximum stress. Fig. 2.9 shows the creep compliance (again the plastic deformation has been subtracted from the result) per cycle for these two samples. The result for both samples show that there is a diminishing effect of hold time with number of cycles, with later cycles accumulating less deformation during hold, leading to an overall higher importance of the first few cycles in determining the creep-fatigue response. This is explored further in Chapter 3 with the help of microstructural strain measurements.

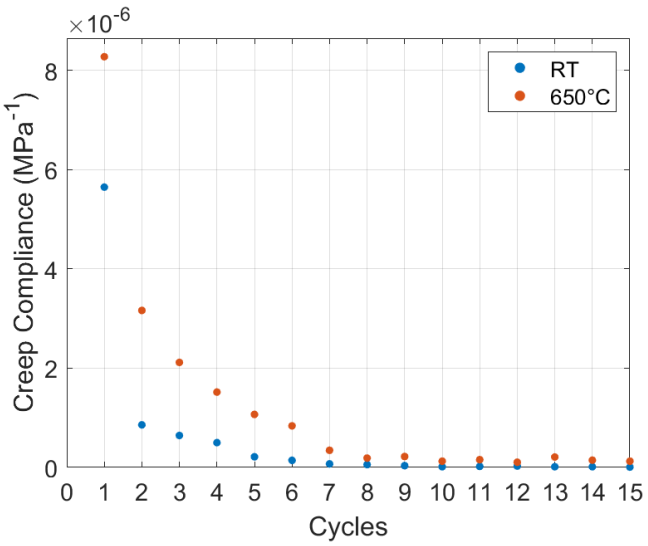

Fig. 2.9. Creep compliance vs. cycles during cyclic creep loading of alloy 709 hourglass samples at RT and 650°C with maximum stresses of 500 MPa and 250 MPa, respectively. Each cycle included a 60 s hold time at maximum stress.

Finally, 16 hourglass samples were loaded in fully reversed stress-controlled experiments, at both RT and 650°C. Fig. 2.10 shows the stress amplitude vs. life plots for all the 16 samples. The RT experiments were conducted at 500 MPa, 450 MPa, 430 MPa and 375 MPa amplitudes, while the 650°C samples were loaded with 250 MPa and 230 MPa amplitudes. For all tests the hold times were present both at maximum and minimum stress. Previous authors have reported that hold times in compression have a regenerative role in creep-fatigue of austenitic stainless steels, acting to prolong their creep-fatigue life (Rao et al., 1993). The results seen here were as expected; the samples loaded at a higher temperature had much lower lives, also, the presence of hold times acted to lower the life of samples at the same stress level. Only the points at 230 MPa show a discrepancy, in which the creep-fatigue experiment with longer hold time (120 s) failed at a higher number of cycles than the one with shorter hold times (60 s), but this can easily be explained through the typical scatter of fatigue results, since the difference is relatively low.

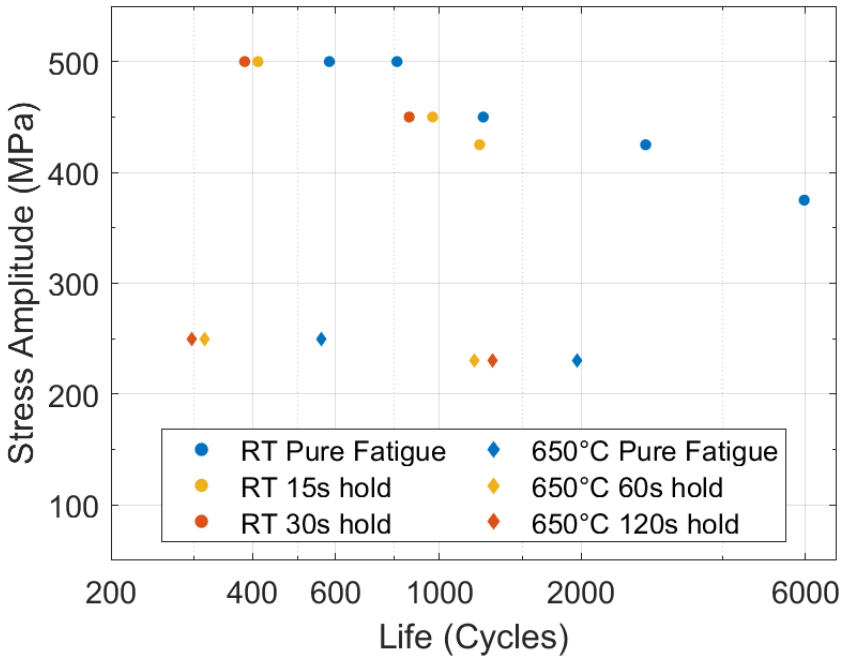

Fig. 2.10. Stress amplitude vs. life for 16 alloy 709 hourglass samples loaded in stress control at RT and 650°C.

2.4 Summary

This chapter went over a brief study of the macroscopic response of stainless steel 709 to plastic, creep, and creep-fatigue loading. The experimental setup presented in section 2.1 is the same one that was used for all experiments that follow in the next chapters. The results presented here serve as a baseline and a starting point for microstructural exploration of alloy 709 response. A few key conclusions can be drawn from the experiments shown: The introduction of higher temperatures and hold times both resulted in higher strain accumulation and lower lives, indicating that creep-fatigue interaction does play a role in the response of alloy 709. Additionally, the early cycles of creep-fatigue loading play an important role, being responsible for the majority of plastic strain accumulation. These conclusions are further explored through the microstructural studies presented in Chapters 3, 4, 5 and 6.

Chapter 3: Grain-scale Strain Accumulation

In Chapter 2, the macroscale response of the austenitic 709 stainless steel alloy under plasticity and creep-fatigue loading was explored, including its failure. As expected, samples loaded at higher temperatures or with longer hold times resulted in higher levels of global strain accumulation, accompanied by more damage, ultimately resulting in faster failure. To understand how these loading parameters affect material response, it becomes necessary to study the material's behavior at the microscale (Remy and Petit, 2002).

The microscale response of crystalline materials to varying loading conditions has been the object of study of many published works, often through the measurement of microscale strain accumulation, as was discussed in Section 1.1.1. A brief review of the most relevant publications to the work presented here follows. Padilla et al. (2012) used a DIC technique with a resolution of about 1.2 μm/pixel to study the microstructural strain accumulation during loading of highly texturized Zirconium. They explored the statistical correlation between crystal orientation (Schmid factors) and inhomogeneities in the strain fields in highly textured hcp Zr and found a moderate correlation between specific slip system activity and accumulated microscale strain. Abuzaid et al. (2012) used a very similar DIC technique to what is presented in this work, with resolution of about 0.1 μm/pixel, to study the accumulation of strains near grain boundaries, specifically the correlation between crystal orientations (e.g., grain boundary misorientation, Schmid factors, active slip systems) and strain accumulation. Carroll et al. (2013) used the same technique to study the interactions between grain boundaries and fatigue crack nucleation.

This chapter will go over the high resolution DIC (HiDIC) technique Carroll et al. (2010) used to measure strain accumulation at the grain scale and the initial application of this technique to both room-temperature and high-temperature experiments with samples subjected to plasticity and creep-fatigue loading. The findings from these initial experiments act as the main motivation for the studies that follow in Chapters 4, 5 and 6.

3.1 Grain-Scale *Ex Situ* Strain Measurements

This section will go over the entire procedure to successfully measure grain-scale *ex situ* strain accumulations using a high-resolution DIC technique and align the results with microstructural information obtained from Electron Backscatter Diffraction (EBSD) scanning. The methodology follows closely what was developed by Carroll et al. (2010), with some improvements being made to the alignment procedure, as described below.

3.1.1 Sample Preparation for EBSD Scans

After machining, the samples described in Chapter 2 were polished in a metallographic polishing machine using silicon carbide paper disks with the following grit sizes: 200, 600, 800, and 1200. Then, the samples were further polished in the same machine, using cloth disks and diamond suspensions with the following particle sizes: 9, 6, 3, 1 and 0.25 μm. At this point, fiducial marks were introduced to the surface of the sample, specifically five Vickers indentation marks were placed at the corners of the area of interest where the microscale strain measurements would be performed, that allow for alignment of microstructural and strain field datasets. Finally, the sample was placed on a vibratory polishing machine for 3-4 hours, using a 0.05 μm colloidal silica solution. This final polishing step produced a surface with lower residual stresses, allowing for better EBSD scan results.

In order to characterize the microstructure of the material, which will be subsequently overlaid onto the grain-scale strain measurements, the samples were placed inside a scanning electron microscope (SEM) and an EBSD scan taken of the surface (Randle and Engler, 2000). EBSD data presented throughout the entirety of this document were collected using a JEOL 7000F SEM, with measurement points spaced by 1 μm. Fig. 3.1a shows a typical EBSD scan result colored by the first Euler angle, with the highly distorted Vickers marks visible at the corners of the image as white diamonds, while Fig. 3.1b shows the grain boundaries obtained using the Mtex EBSD analysis Matlab Toolbox (Hielscher and Schaeben, 2008) and considering changes in crystal orientation >7° to occur across boundaries. Neighboring points with average misorientation larger than 7° result in a boundary between them, while points with smaller orientation difference are considered to be within the same grain. The 7° threshold was used in order to account for noise in the EBSD scan, resulting from residual stresses still present on the surface after vibratory polishing.

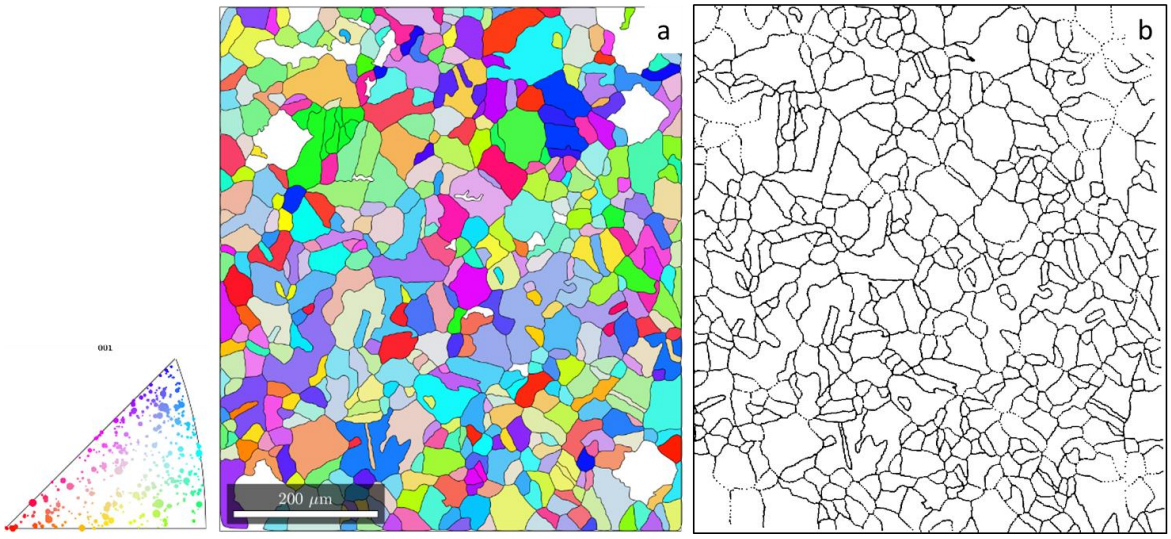

Fig. 3.1. (a) EBSD scan result, colored by the first Euler angle, with highly distorted Vickers marks visible in the corners; (b) Grain boundaries obtained by taking changes in crystal orientation >7°.

3.1.2 High-Resolution Digital Image Correlation (HiDIC)

In order to measure microscale strain accumulations using DIC, the correlated images must be acquired with sufficiently high magnification, and consequently resolution, so that the appropriate number of correlation points can fit within a typical (or smallest) grain of the tested sample to provide the desired grain-scale measurements. To reach these resolution requirements, the reference and deformed DIC images are taken under an optical microscope, before and after loading. All the grain-scale DIC results shown throughout this document were taken using an objective lens with 40x magnification, resulting in ~0.09 μm/pixel spatial resolution images. The main advantage of this approach is this increased resolution over *in situ* imaging (which typically would be above 1-2 μm/pixel), while the main disadvantage is the reduced field of view resulting from images taken at high magnification (FOV of ~190x190 μm using a 2000x2000 pixels camera). This disadvantage can be addressed by taking sets of images in a grid (with significant overlap between them, around 50%) to cover the entire region of interest. These sets of images can then be stitched to form very large reference and deformed images that are then correlated. However, since a series of images need to be taken at the reference point and at the deformed state, it becomes much harder to make *in situ* measurements using this approach. With the sample under load, even small vibrations and variations of the applied load can interfere with focus, especially with the reduced depth of field of the high magnification imaging device. Because of this difficulty, all microscale strain measurements shown in this work were taken *ex situ*, that is, the sample was removed from the loading frame and placed under the optical microscope for each set of images to be taken. Therefore, all the strains shown are plastic residual strains (resulting from plasticity and/or creep loading).

The use of ultra-high-resolution microscope images allow for DIC measurements at the grain scale, but the general limitations of local DIC (as seen in Chapter 1) still apply. The (effective) density of measurement points is determined by the subset size used during correlation. Thus, in order to measure strains with sub-grain resolution, the subset size must be considerably smaller than the average grain size, allowing for multiple subsets to fit within each grain. Besides optical magnification, the main limiting factor to shrinking the subset size comes from the random speckle pattern required for correlation, as seen in Chapter 1. The speckle pattern applied to all samples discussed in this work was obtained by depositing 1000 grit silicon carbide powder to the polished surface (after EBSD scanning) using compressed air. Fig. 3.2a shows a typical DIC reference image, resulting from the stitching of a 6 by 6 grid of images (roughly as shown by the yellow lines, the 50% overlap is not shown for clarity), with the five Vickers fiducial marks appearing in the corners. Fig. 3.2b shows a magnified view of the highlighted square, with the subset size drawn. A similar set of images of the surface is then taken after deformation, and the stitched reference and stitched deformed images are correlated using a subset size of 61 by 61 pixels (~5.5 by 5.5 μm, as shown in Fig. 3.2b) and a step size of 10 pixels (~0.9 μm), for most cases. If a finer speckle pattern was applied to the surface, a lower subset size could be used, increasing the effective density of measurement points for DIC, but very fine random speckle patterns are harder to achieve (Park et al. 2017).

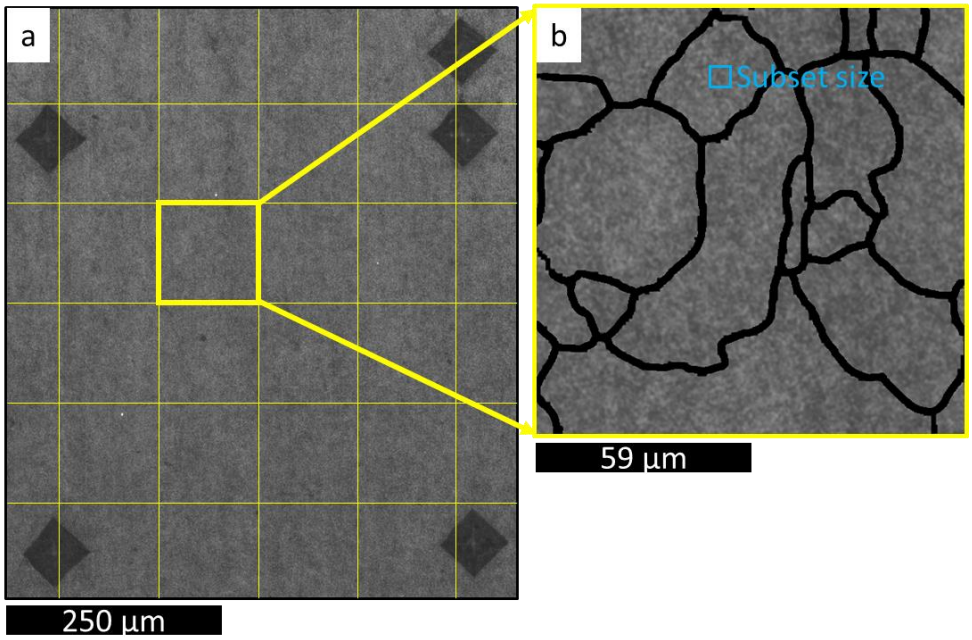

Fig. 3.2. (a) DIC reference image, resulting from the stitching of 6 by 6 images (as shown); (b) Magnified view of the highlighted square, with the subset size shown.

3.1.3 Alignment of DIC and EBSD Datasets

The final step in combining the two datasets (from HiDIC and EBSD) is to align the HiDIC measured strain fields with the underlying microstructure. Even though the five Vickers fiducial marks are visible in both datasets (Fig. 3.1a and Fig. 3.2a) and can be used for alignment as done in Carroll et al. (2010), there is distortion present in the EBSD scan results (Fig. 3.1a), which could result in a significant alignment error if alignment was done simply by using the visible fiducials as reference points between the two datasets. In order to account for this distortion, and to improve the alignment accuracy of the technique developed by Carroll et al. (2010) thus allowing for more localized observations of the strain accumulation (near grain boundaries, for example), a set of optical images, taken at the same magnification level as the HiDIC images, of the etched surface of the sample prior to applying the DIC pattern, are used as an intermediate step for alignment. Etching was done using a 36% weight of solute / weight of solution of HCl in water, for 15 minutes at 100°C, allowing for grain boundaries to be visible under the optical microscope.

Fig. 3.3, which includes the three types of images that are taken of the surface, makes it easier to understand the alignment process. First, the grain boundaries obtained from EBSD (Fig. 3.3a) are aligned to the optical grain boundaries obtained from the optical imaging of the etched surface (Fig. 3.3b). This is done by manually selecting prominent grain-boundary features visible in both images (such as, for example, points 1 and 2 marked by the blue crosses) and fitting a projective transformation to these points. For this type of transformation, all straight lines remain straight, but parallelism is not conserved. Then, the optical grain boundaries (Fig. 3.3b) are aligned to the DIC reference image (Fig. 3.3c), through the use the five Vickers fiducial marks. The corners of the fiducials are manually selected (for example, as shown by points 1 and 2 marked by the orange X's) and an affine transformation is fitted to those points. For this type of transformation, both straightness and parallelism are conserved. These two transformations can then be used consecutively to align the EBSD results to the DIC reference image, and since the DIC reference image establishes the coordinate system where the results of the correlation are computed, the DIC results can now be overlaid by the EBSD-obtained boundaries.

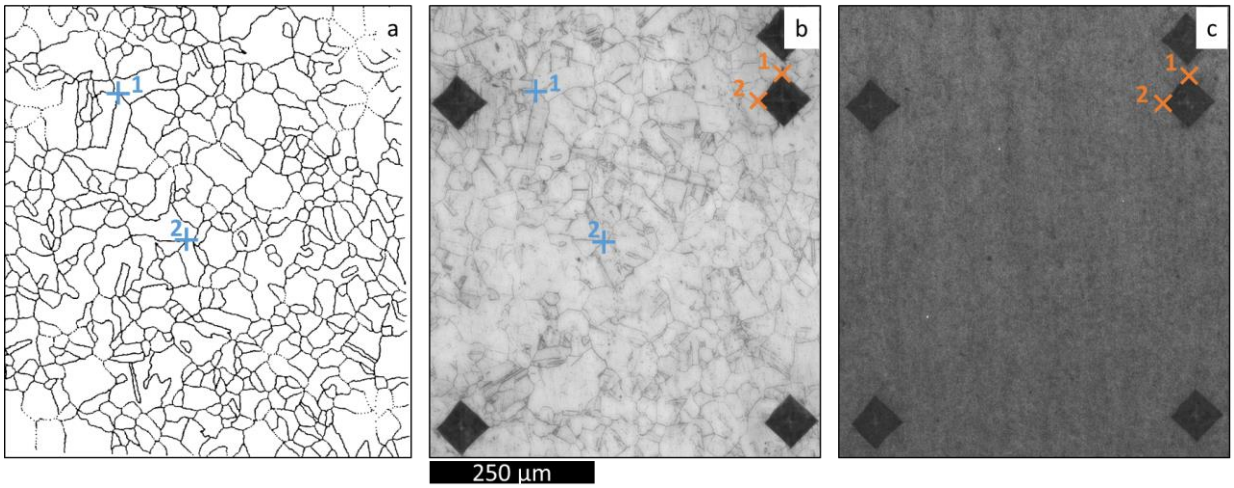

Fig. 3.3. (a) Grain boundaries obtained from EBSD scan; (b) Optical image resulting from stitching a grid of 6 by 6 images; and (c) DIC reference image resulting from stitching the same grid of images after applying the speckle pattern.

Applying optical images of the grain boundaries as an intermediate step for alignment makes use of the strengths of both EBSD and optical microscopy. On one hand, EBSD is capable of providing microstructural information not available through optical microscopy, and is also more reliable in finding all the existing boundaries in the region of interest. On the other hand, optical microscopy is more reliable in locating the grain boundaries within the DIC reference frame, since the images are taken under the same microscope with the same magnification level.

In order to estimate the average error in placement of grain boundaries within the HiDIC results, an optical image of the etched surface was overlaid onto the EBSD boundaries, as shown in Fig. 3.4a. Then, the distance between the EBSD-boundary and the same boundary as seen in the optical image (called henceforth "alignment error") was measured for all boundary segments within the region of interest of the sample. Fig. 3.4b shows a magnified view of a region of the sample, with number labels pointing to the positions at which the alignment error was measured. Finally, Fig. 3.4c shows a histogram of the measured alignment errors over the entire region of interest (404 total points). The mean error was found to be 0.52 μm, with a maximum error of 2.86 μm. Errors above 1 μm happened in about 10% of the points (43 out of the 404 points), and the most common error value was between 0.15 and 0.3 μm. The significance of this error depends on the size of the grains (average grain sizes of 25-32 μm) and the correlation point density of the HiDIC measurements (subset sizes around 5.5 μm), both considerably larger than 0.52 μm for all the cases studied in this work. Carroll et al. (2010) reported their alignment procedure to produce alignment errors "better than 5 μm", which is of the order of the size of the smallest grains found in alloy 709 and therefore not satisfactory for the present application. Thus, the improvement achieved here by using optical images as intermediate step is significant for our experiments. Finally, the fact that the resulting average misalignment (0.52 μm) is very close to half the EBSD

spacing (1 μm) indicates that the described alignment procedure is capable of reaching the limit of how well the two datasets could be aligned, with the main source of "error" being the inherent uncertainty from EBSD (a smaller EBSD spacing could result in a smaller average misalignment).

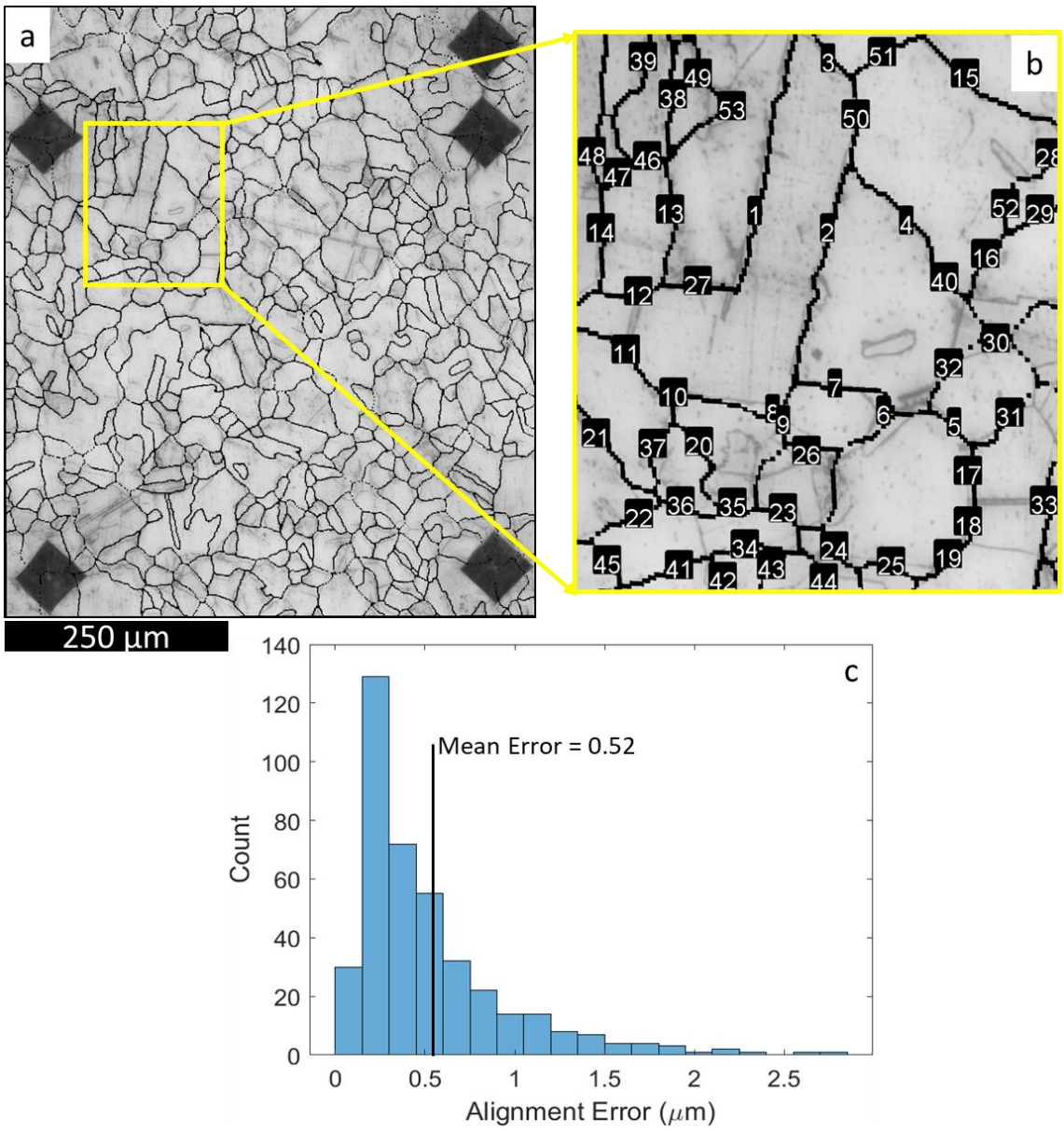

Fig. 3.4. (a) Optical image of etched surface overlaid by EBSD boundaries; (b) magnified view of highlighted squared, showing the points where the distance between optical and EBSD boundaries were measured; and (c) histogram of the alignment error measured from the entire region of interest (total of 404 points).

3.2 Grain-Scale Residual Strain Field Results

This section presents a first set of grain-scale residual strain measurements, taken from a dog-bone sample (as shown in section 2.1) loaded at room temperature. Fig. 3.5a, b and c show the contour plots of the residual strain components (ε_{yy}, ε_{xx}, and ε_{xy} respectively) from a sample loaded to 400 MPa at room temperature with no hold time. The strain field is highly inhomogeneous, with areas of strain concentration mostly near grain boundaries. Fig. 3.5b shows a magnified view of the highlighted rectangle (in Fig. 3.5a), with white arrows indicating 5 different boundaries with misorientation angles between 59.3° and 60.5° (Σ3 or twin boundaries). Boundary 1 has similar strain levels on each side, close to the overall average strain, while boundary 2 presents strain on both sides that is much higher than the global average (average = 0.031). Both boundaries 1 and 2 can be characterized as (strain) transmitting boundaries, with slip being transmitted across them thus causing comparable plastic strain on both adjacent grains. In contrast, boundaries 3 and 4 separate grains with one of the adjacent grains having higher strain than the other, indicating that these boundaries can be classified as blocking boundaries (Eshelby et al., 1951; Hall, 1951; Petch, 1953). Across blocking boundaries slip is not as readily transmitted, causing a strain concentration on one side of the boundary with the other side remaining relatively strain free (often at strain levels well below the global average). Finally, boundary 5 has both adjacent grains relatively strain free. These results are qualitatively similar to those obtained by Abuzaid et al. (2012) for Hastelloy X, indicating that misorientation alone (recall boundaries 1 through 5 all possess the same misorientation angle) cannot fully predict strain localizations (this is further explored in Chapters 5 and 6).

The general shape of these microscale strain fields, and their dependence on loading parameters is the subject of the next sections, as well as Chapter 5. Chapter 4 introduces the

concept of the Representative Volume Element (RVE), which can be used to connect the micro and macroscale responses, while Chapter 6 proposes a neural-network approach to predict microstructural strain accumulation near grain boundaries.

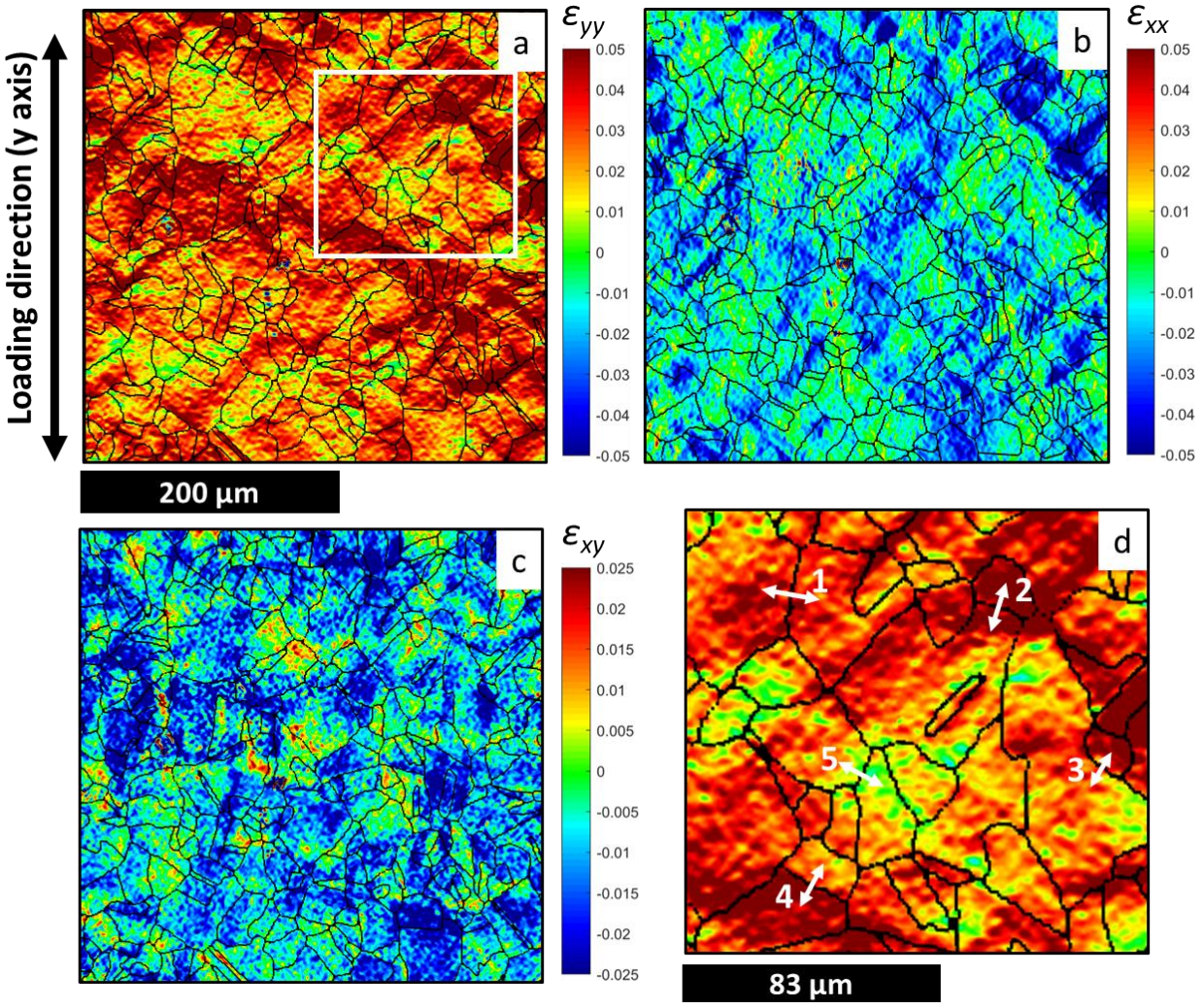

Fig. 3.5. (a) ε_{yy} residual strain field obtained for a sample loaded to 400 MPa at room temperature; (b) and (c) ε_{xx} and ε_{xy} for the same sample; (d) Magnified view of highlighted rectangle (in (a)), showing twin boundaries with different strain levels (indicated by white arrows).

3.3 Cyclic Creep-Fatigue Residual Strain Accumulation

3.3.1 Room Temperature Experiments

A possible difference between the microstructural strain accumulation resulting from plasticity and creep (at room temperature) was investigated using HiDIC. Fig. 3.6 shows the resulting strain fields for an hourglass sample (as shown in section 2.1) loaded in two steps at room temperature. These strain fields are shown overlaid on the optical-microscopy-obtained etched boundaries, since EBSD scans were not performed on these samples. First the sample was loaded to 500 MPa (~60% above yield), and was unloaded as soon as it reached the maximum stress (purely plastic cycle). Fig. 3.6a shows the residual plastic axial strain field obtained after this first loading step (correlation of point **a** with the reference, in the schematic stress vs. time curve). Then, the sample was loaded again to 500 MPa and held at this maximum stress level for 1800 seconds (creep cycle). Fig. 3.6b shows the residual axial strain field obtained after this second loading step (correlation of point **b** with the reference, in the schematic stress vs. time curve). Fig. 3.6c shows the incremental residual axial strain field between the two loading steps, with different contour limits for visibility (correlation of point **b** with point **a**, in the schematic stress vs. time curve). These contours show that strain accumulates at specific locations whether through plastic or creep deformation. Since the shape of the strain contours is very similar, it implies that creep straining occurs at the same locations where plastic strains had initially developed.

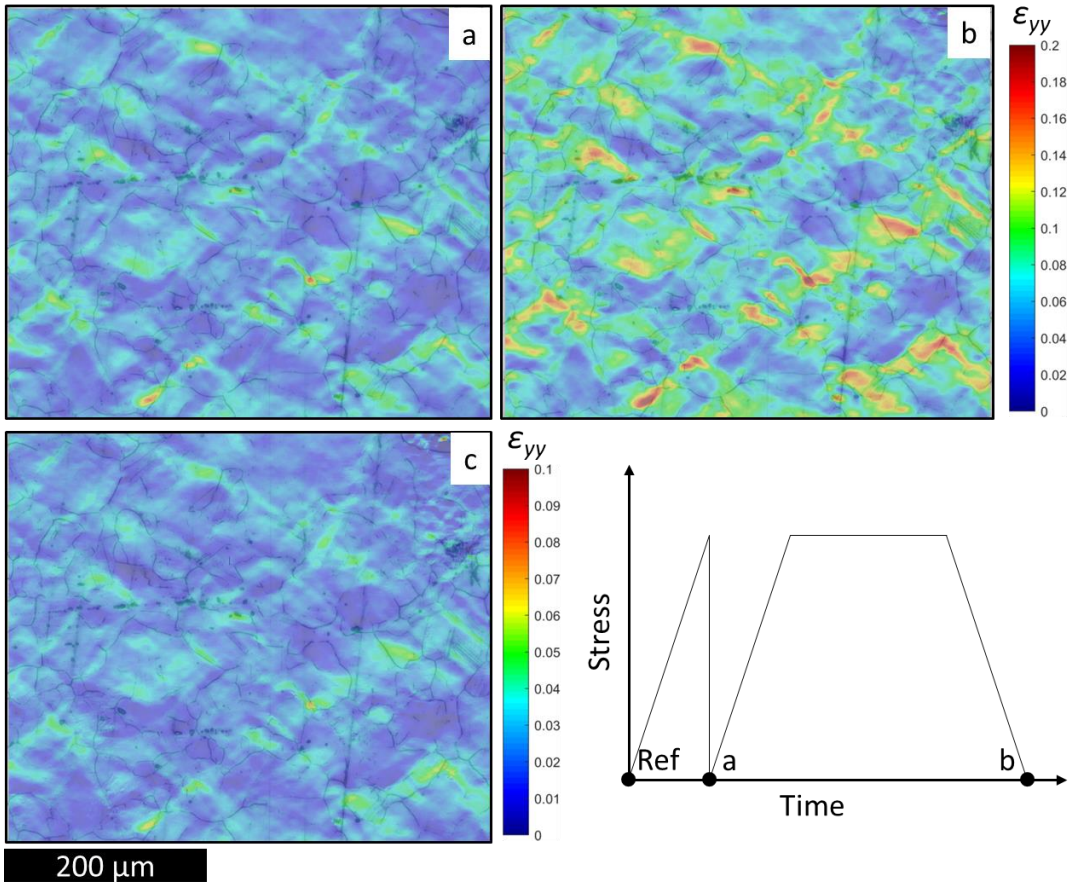

Fig. 3.6. (a) Residual axial strain field after a tensile cycle (500 MPa) without any hold time (correlated with reference); (b) Residual axial strain field in the same sample after a subsequent hold time of 1800 s at 500 MPa (correlated with reference); and (c) Incremental residual axial strain field with different contour limits (b correlated with a).

The previous experiment made a comparison between the strains accumulated in a single plasticity loading with a relatively long hold period creep loading. Such a long hold time was used in this first experiment before we had established the influence of hold time on creep. A second case was then also considered, termed “creep-fatigue” loading, which involved several loading cycles and with load reversal. The results obtained for such a fully-reversed creep-fatigue test at room temperature are discussed here. An hourglass sample was loaded to 500 MPa and held there for 30 s, being subsequently loaded to -500 MPa and again held there for 30 s. For each half-cycle of loading, the sample was removed from the load frame and a set of images was taken. This

process was performed for 8 full (tensile and compressive) loading cycles. Fig. 3.7a shows contour plots of the residual axial strains after the tensile and compressive half-cycles of the 1st and 8th cycles (all correlated to the undeformed state), while Fig. 3.7b shows a plot of the average axial strain for each measured half-cycle. Again, the results of Fig. 3.7a indicate that strains accumulate at the same locations, with the first cycle being responsible for defining the "hot-spots" for strain accumulation. The contours also indicate some degree of irreversibility for these residual strains, since even after being held at -500 MPa for 30 s, no negative axial strains are found anywhere in the region of interest. However, the reversal of load does have a noticeable effect, especially evident by the average strains plotted in Fig. 3.7b, which shows a plastic recovery at the very early cycles with a subsequent increase leading to eventual failure.

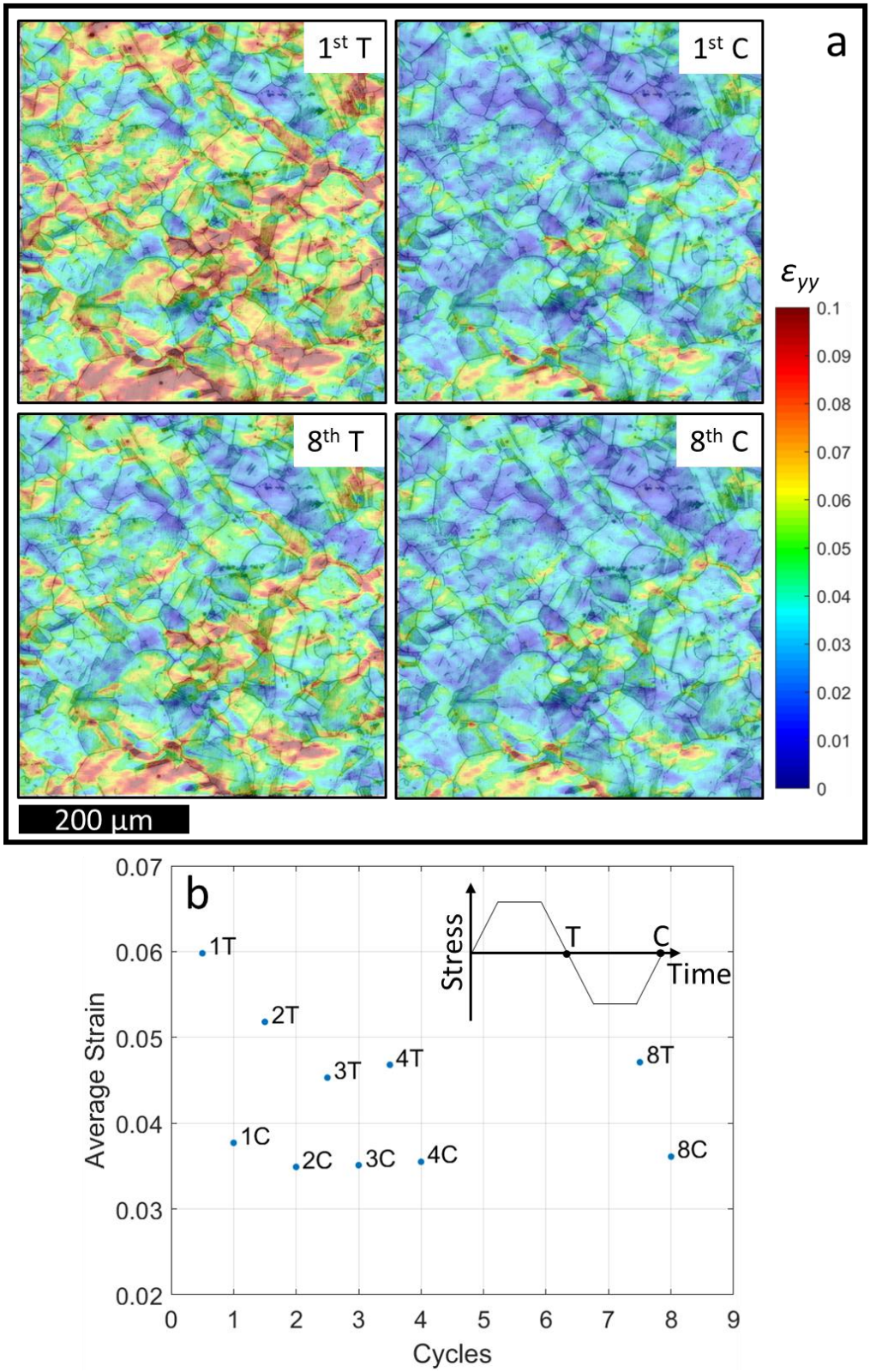

Fig. 3.7. (a) Contour plots taken after the tensile and compressive half-cycles of the 1st and 8th cycles; and (b) Scatter of average axial strain after each measured half-cycle.

3.3.2 High Temperature Experiments

Corresponding experiments were also conducted at a temperature of 650°C. An hourglass sample at 650°C was loaded in two loading steps: first to 250 MPa (~60% above yield at 650°C) and then unloaded (plastic cycle), followed by loading again to 250 MPa now being held at maximum stress for 120 seconds (creep cycle). In analogy to Fig. 3.6, Fig. 3.8a shows the residual axial strain field obtained after the first loading step (correlation of point **a** with the reference, in the schematic stress vs. time curve), while Fig. 3.8b shows the residual strain field obtained after the second loading step (correlation of point **b** with the reference, in the schematic stress vs. time curve). Fig. 3.8c shows the incremental residual axial strain field between the two loading steps, with different contour limits for visibility (correlation of point **b** with point **a**, in the schematic stress vs. time curve). The same observation from the room temperature experiments (from Fig. 3.6,) is valid here. The distribution of strains within the region of interest is very similar, again indicating that the strains from creep accumulate at the same locations where plastic strains had accumulated. It is important to note that this result does not mean that temperature has no influence on the location of strain accumulation, but only that it seems to not have an effect on the nature of the interaction between damage locations from creep and plasticity.

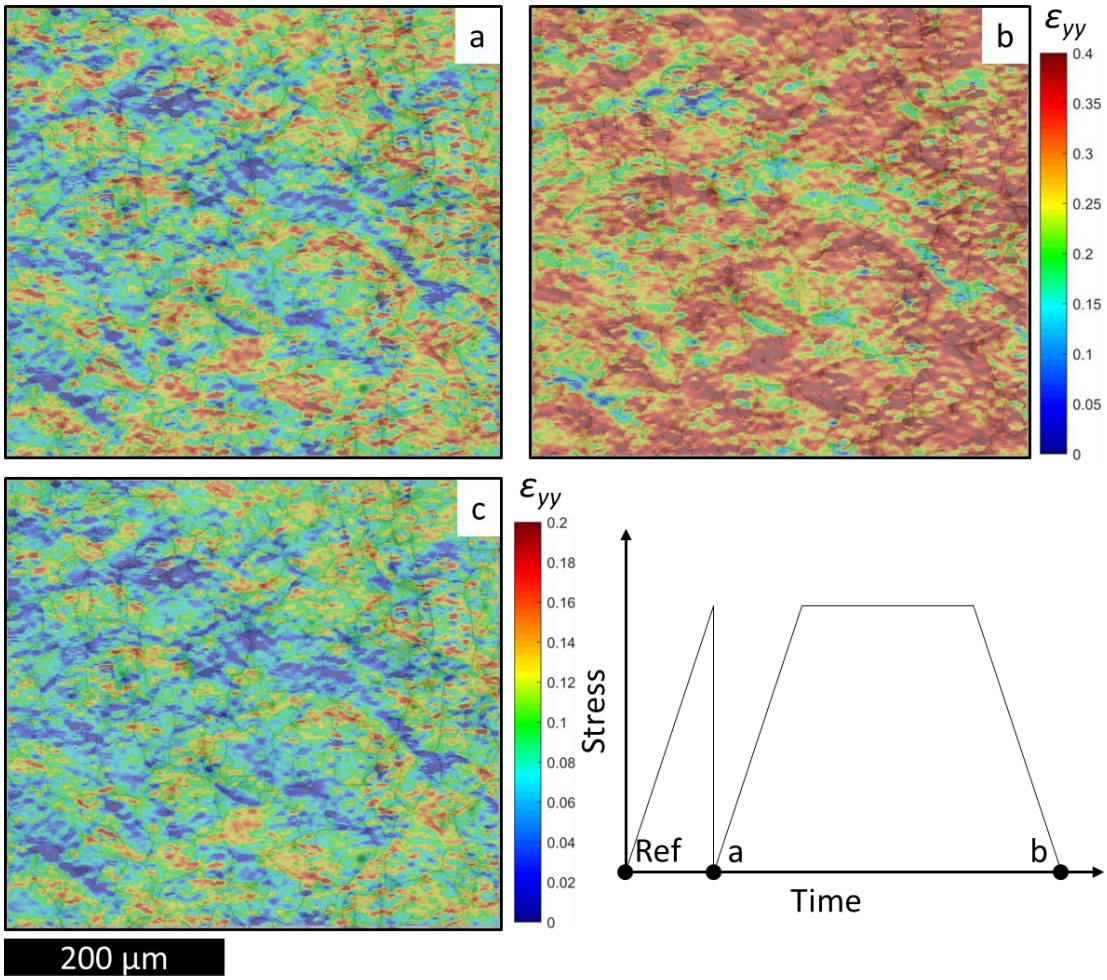

Fig. 3.8. (a) Residual axial strain field after a tensile cycle (250 MPa at 650°C) without any hold time (correlated with reference); (b) Residual axial strain field in the same sample after a subsequent hold time of 120 s at 250 MPa and 650°C (correlated with reference); and (c) Incremental residual axial strain field with different contour limits (b correlated with a).

In the next experiment, as before for room temperature, a sample was loaded in fully reversed creep-fatigue at 650°C. An hourglass sample was loaded to 250 MPa and held at maximum stress for 120 s and then loaded down to -250 MPa and held at minimum stress for 120 s, for a total of 3 full cycles. As before, after each half-cycle the sample was removed from the load frame and a set of images was taken. In analogy to Fig. 3.7, Fig. 3.9a shows contour plots for the residual axial strain after the tensile and compressive half-cycles of the 1st and 3rd cycles (all correlated to the undeformed state), while Fig. 3.9b shows a plot of the average axial strain for

each measured half-cycle. These results are very similar to the ones shown in Fig. 3.7 (for room temperature), and the same observations can be made. The recovery of strains after initial cycles seems less pronounced, as can be seen in Fig. 3.9b, with the average strain from cycle 1 much closer to the average strain of subsequent cycles (when compared to the room temperature results of Fig. 3.7). The same irreversibility of the strains is observed, with strains never reaching negative values anywhere in the region of interest, even after the compressive half-cycle, indicating that temperature doesn't affect the nature of creep directionality, even if the exact mechanism behind deformation is not clear.

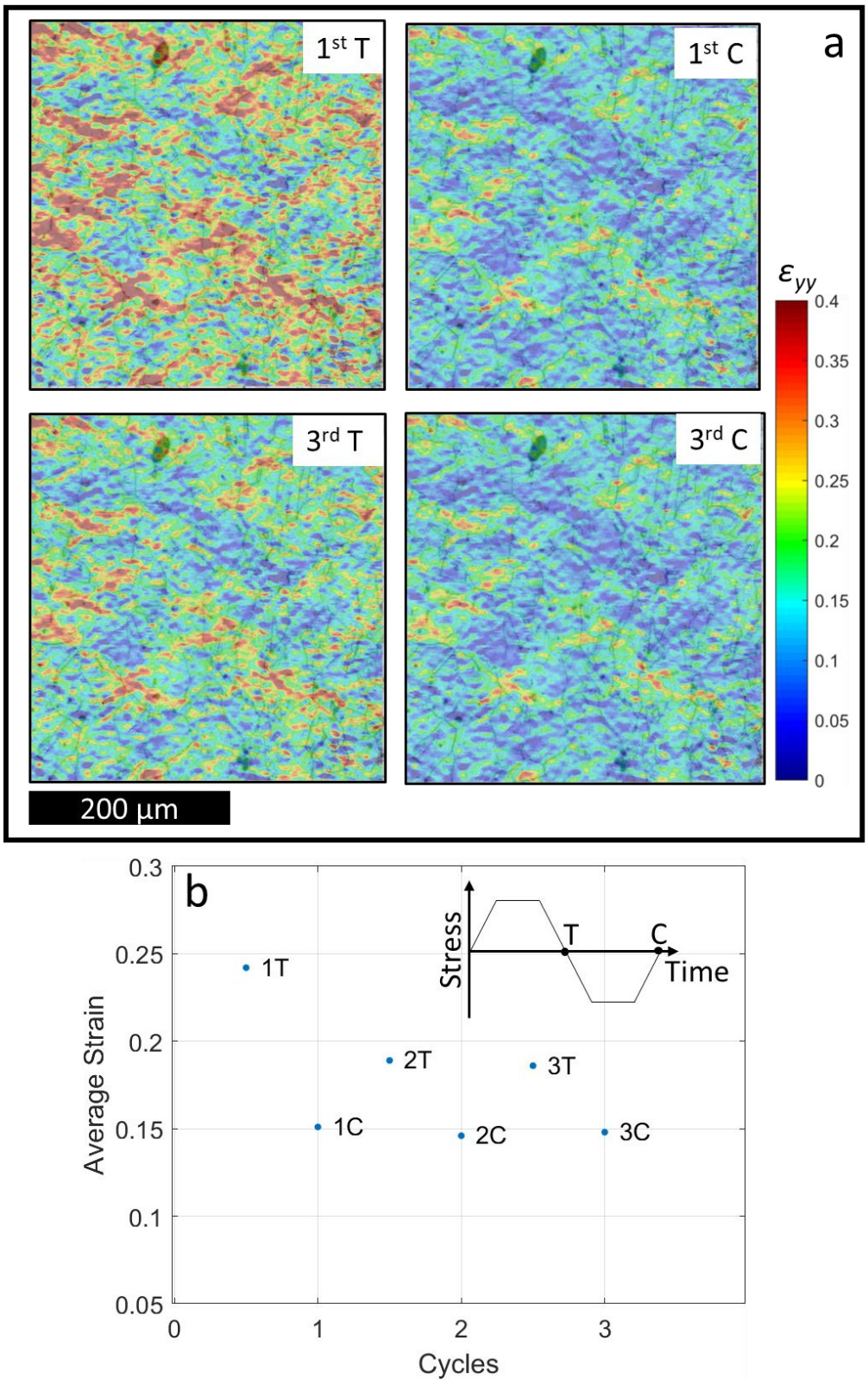

Fig. 3.9. (a) Contour plots taken after the tensile and compressive half-cycles of the 1st and 3rd cycles; and (b) Average axial strain after each measured half-cycle.

3.4 Onset of Failure – Fatigue Crack Nucleation

Following the same sequence presented in Chapter 2 at the macroscale, after room temperature and high temperature experiments, the next step was to investigate creep-fatigue failure. Here, the idea was to explore the connection between microstructural strain accumulation and eventual nucleation of creep-fatigue microcracks. To this end, the same hourglass sample shown in the results of Fig. 3.6 was subsequently loaded at room temperature with a stress amplitude of 500 MPa, with hold times of 30 s both at maximum and minimum stress. Fig. 3.10a shows the stitched DIC image obtained after the 400^{th} tensile cycle, with the white arrows indicating the locations where microcracks were found after the 400^{th} tensile cycle, through visual inspection under the optical microscope. Fig. 3.10b and c show the strain field obtained after the 100^{th} tensile half-cycle (overlaid on the optical image of the grains obtained prior to loading), with the black arrows pointing to the same locations where cracks were found after the 400^{th} tensile half-cycle. Fig. 3.10c shows a magnified version of the strain field shown in Fig. 3.10b, with the inset showing a location in the vicinity of a grain boundary, with high strain accumulation, where a crack eventually nucleated. All the observed cracks appeared in locations with high strain accumulation, indicating that these hot-spots accumulate damage more quickly, leading to microcrack nucleation. The correlation between the strain accumulation hot-spots, shown to develop from the very first cycle, and the location of eventual creep-fatigue crack nucleation observed in these results has also been reported for pure fatigue of Hastelloy X (Abuzaid et al., 2013). It is also interesting to note that most of the detected strain accumulation locations fall across or near grain boundaries, as seen in the inset of Fig. 3.10c. Therefore, a closer look at these specific locations of strain accumulation in the vicinity of grain boundaries is presented in Chapters 5 and 6.

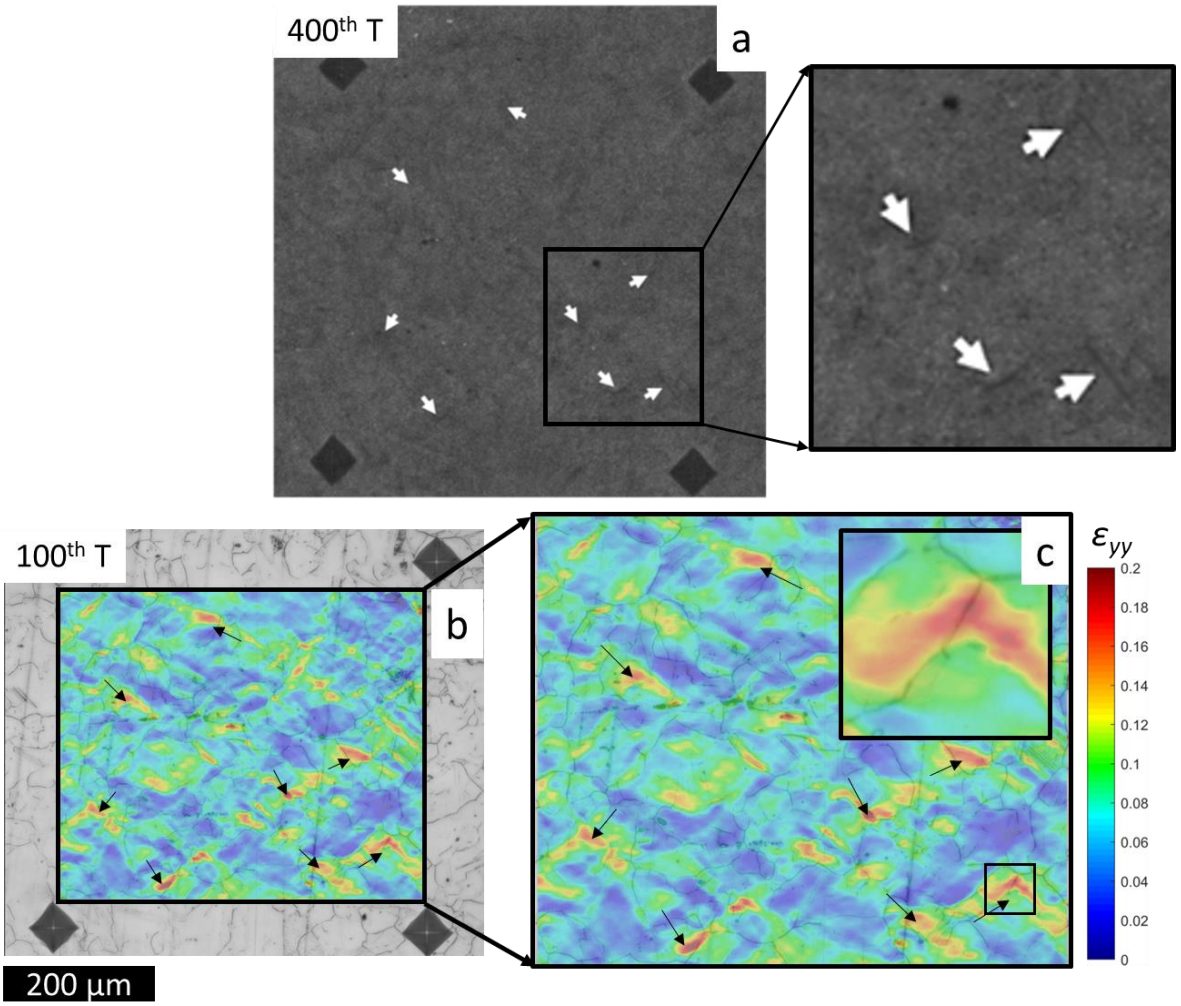

Fig. 3.10. (a) DIC stitched image obtained after the 400th tensile half-cycle; (b) Residual axial strain field obtained after the 100th tensile half-cycle (overlaid on the optical grain boundaries); and (c) Magnified view of the strain field with inset showing strain accumulation at grain boundary (arrows indicate locations where cracks were found after 400 cycles).

3.5 Summary

This chapter described the HiDIC technique used throughout this work to measure grain-scale residual strains. Following the method developed by Carroll et al. (2010), and with an improved alignment methodology, HiDIC can be used to measure strain at the microstructural length scale and align the results with microstructural information obtained from EBSD scans. The improvement in alignment accuracy came with the introduction of an optical image of the etched surface, where the grain boundaries were visible, as an intermediate step in aligning the EBSD

results to the DIC reference frame. The average misalignment of the new alignment procedure was estimated to be 0.52 μm. Initial HiDIC results obtained from cyclic experiments at both room temperature and high temperature (650°C) were also presented. The main conclusions from these results are:

1) At the microstructural level the residual strain fields are highly inhomogeneous;
2) Hot-spots for strain accumulation tend to occur in the vicinity of grain boundaries;
3) The distribution of strains within the region of interest resultant from solely plastic loading and from subsequent creep loading appear to be very similar, with strains accumulating at the same spots;
4) With further cyclic loading, the distribution of strains does not change, the hot-spots for strain accumulation are defined by the first loading cycle;
5) The average strain level during fully-reversed creep-fatigue tests decays during the initial cycles, reaching a steady state which will eventually lead to failure;
6) There is a correlation between the hot-spots for strain accumulation and eventual microcrack nucleation, which indicates that damage accumulates more quickly at these spots with high strain levels.

These findings motivated the studies presented in Chapters 4 and 5, where the differences between strain fields resulting from different loading conditions are explored, through the use of the Representative Volume Element (RVE), which can be used to relate the microscale measurements to the macroscale response. The work presented in Chapter 6 builds upon the findings of Chapter 5 about local grain-boundary strains to propose a neural-network approach to predict residual strains in the regions near to grain boundaries.

Chapter 4: Measuring Representative Volume Elements from High-Resolution Grain-Scale Strain Fields[1]

Chapters 2 and 3 described an experimental investigation on the macro and microscale response of a polycrystalline austenitic stainless steel subjected to plasticity, creep and fatigue loading conditions. Linking different length scales is an important component of many multiscale modeling frameworks, and is often done through homogenization techniques (e.g., Bargmann et al., 2018). Such homogenization techniques are largely based on the concept of the Representative Volume Element (RVE). This chapter presents the development of a new and robust methodology of experimentally measuring strain-based RVEs, which takes into account the statistical nature of the RVE. Subsequently, Chapter 5 applies the proposed method to study the influence of loading parameters on the size of the RVE, with the goal of analyzing the differences on strain accumulation at the microstructural level.

4.1 Background

It is well established that strain heterogeneities at the microscale are related to material response at the macroscale in crystalline metals (e.g., Delaire et al., 2000; Raabe et al., 2001), with many studies exploring their formation and development in polycrystals subjected to various loading conditions. For example, in plastic deformation Sachtleber et al. (2002) used a photogrammetry-based digital image correlation (DIC) method to measure surface strains in aluminum polycrystal samples with columnar coarse grains and identified triple-points as preferential spots for strain localization. In fatigue, Abuzaid et al. (2013) used a high-resolution

[1] This Chapter is an expanded version of Vieira and Lambros (2021a)

DIC technique to measure strain inhomogeneities at the grain scale of a nickel superalloy, and their correlations to micro-crack nucleation. For creep, Chen et al. (2015) used an *in situ* neutron diffraction technique to measure strains between grains of pre-strained austenitic stainless steel samples loaded at varying temperatures, reporting no change in the distribution of strains during creep.

The link between such microstructural observations and macroscale response is often achieved through the use of homogenization techniques. Homogenization itself must be performed within a volume of material that has been described by Hill (1963) as being able to reproduce the average value of some property of the bulk material, forming the basis of the concept of a Representative Volume Element (RVE). Many authors have recognized the existence of multiple RVEs, coining the terms "microstructural volume element" and "property volume element", to describe an RVE capable of reproducing macroscale average microstructural properties (e.g., grain size, twin density, misorientation distribution) or mechanical properties (e.g., moduli, yield strength, strain distribution), respectively (Echlin et al., 2014). Bagri et al. (2018) not only recognized the existence of different types of RVE, but also highlighted the inherently statistical nature of the RVE, using the term "statistically equivalent RVE" first coined by Swaminathan et al. (2006) and Swaminathan and Ghosh (2006), where they describe the RVE as the smallest microstructural domain for which statistical distributions of morphological parameters, or material properties, converge to those for the entire microstructure. With this understanding, the RVE is not only required to deterministically and uniquely reflect only the average macroscale property, but also its statistical distribution. Experimentally, these statistical distributions can be understood as the variations on the response that would result from, say, a series of samples cut from the same bulk material. Such variations are always present in polycrystals because of the random nature of

the process of crystal formation. Note that this variability from one sample to another is inherent to the polycrystal, and is differentiated from apparatus-related experimental error which would present even in measurements from one specific sample.

With the RVE playing such a central role in homogenization methods required to connect microstructural results, both experimental and numerical, to the macroscale response, it follows that there has been much study concerning the estimation of the RVE size for different materials and properties. Bargmann et al. (2018) presented an extensive review on numerical methods for RVE estimation, which also includes many statistical approaches for a range of different materials (Githens et al., 2020; Motaman et al., 2020). Of special relevance to the present effort is the stereological approach of Critchfield and Johnson (2020) where they select multiple random samples from within a numerically simulated domain in order to statistically estimate the microstructure-based RVE size. On the experimental side, several studies have developed methods of measuring the size of an RVE, with one of the earlier studies by Liu (2005) introducing the idea of using full-field strain measurements to determine the size of a strain-based RVE. Efstathiou et al. (2010) presented another method of experimentally determining the size of a strain-based RVE, using the standard deviation of the average strains in different regions of the strain field as a measure of the homogenization of strains. More recently, Ravindran et al. (2017) proposed a method of experimentally measuring a strain-based RVE based on the average strain of an increasing square portion of the microstructure. A few other studies have made attempts at measuring RVE sizes experimentally, e.g., Koohbor et al. (2016) where a preliminary version of the method from Ravindran et al. (2017) was used, and Stinville et al. (2017) where they used the density of candidate grain-boundaries for crack nucleation (obtained from a model proposed in a previous work) to estimate the fatigue-failure-based RVE size of a nickel superalloy.

The following sections in this chapter describe the development of a robust methodology of measuring the size of an RVE based on experimental grain-level strain fields. As described above, several techniques have already been proposed for this, and each of these have advantages and disadvantages–one disadvantage being that these existing techniques do not explicitly account for the statistical nature of the RVE. Here we will draw from the advantages of these existing techniques and, by combining them with stereological approaches for the numerical estimation of RVEs, we will develop a new method of experimentally measuring strain-based RVEs that accounts for its statistical nature.

4.2 Current Experimentally-Based RVE Measurement Methods

This section will describe in detail the advantages and disadvantages of two existing methods, namely those of Efstathiou et al. (2010) and Ravindran et al. (2017), on which the proposed new method (outlined in Section 0) is based. As a case study, we will apply the existing methods to experimental results obtained using the HiDIC technique, described in Chapter 3, on two dog-bone samples loaded with different loading parameters. Sample 1 was loaded to 80 MPa for 1 hour at 800°C, while sample 2 was loaded to 215 MPa for 1 hour at 300°C. The influence of loading conditions on the size of the RVE is the subject of Chapter 6, and for now it is enough to know that different strain-based RVE sizes can be expected for samples that undergo different deformation (Yang et al., 2019). Fig. 4.1 shows the residual axial strain field obtained for sample 1 (Fig. 4.1a) and sample 2 (Fig. 4.1b), overlaid with microstructures obtained from EBSD. The reason why these two cases were chosen to exercise the RVE-measurement approaches of Efstathiou et al. (2010) and Ravindran et al. (2017) is that, as can be seen in Fig. 4.1, the strain fields generated in these two cases are quite different.

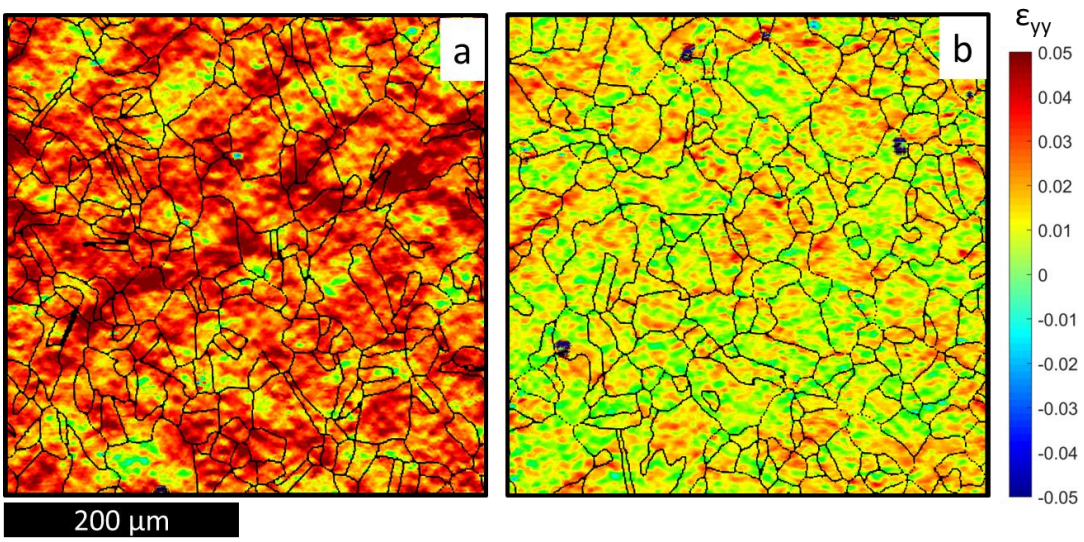

Fig. 4.1. Residual axial strains obtained for two stainless steel 709 samples loaded to (a) 80 MPa for 1 hour at 800°C (sample 1) and (b) 215 MPa for 1 hour at 300°C (sample 2), overlaid with microstructures obtained from EBSD.

4.2.1 Standard Deviation Method

The first method used to obtain the strain-based RVE size follows closely what was developed by Efstathiou et al. (2010): dividing the strain field into a grid of boxes of the same size and plotting the variation of the standard deviation of the box averages vs. the size of the boxes. Then, the RVE size is determined by fitting a line to the trailing points and assuming a deviation from linearity to be due to a box size considerably smaller than the RVE. Fig. 4.2 shows how this method, which we will refer to as the "standard deviation method", can be applied to sample 1. First, the field is divided into a grid of boxes of a given size, as shown in Fig. 4.2a for a box size of 100 x 100 µm, then the average strain of each box is calculated, and finally the standard deviation of these averages is calculated. This is repeated for each box size, varying from the size of the entire field of view to a single pixel. Fig. 4.2b shows the plot for the standard deviation of box average strains vs. the box size and a fitted straight line to the tail end of the useful data points

that can be used to measure the RVE. In this case, deviation from linearity was observed for boxes at around 100 μm, and this value can be taken as the RVE size for this field[2].

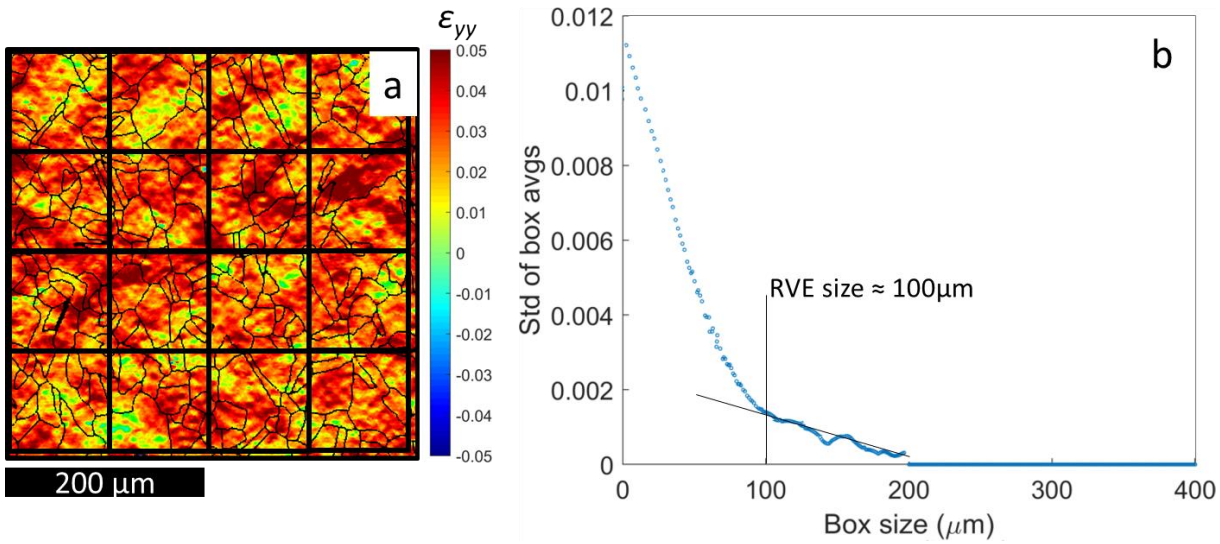

Fig. 4.2. (a) Strain field obtained for sample 1, superimposed by a grid of boxes of size 115 μm; (b) The plot of standard deviation of box average strains vs. box size and the fitted line used to measure the RVE size.

One weakness of this method is apparent by looking at the box sizes from 200 to 400 μm in the plot of Fig. 4.2b. Since these boxes are larger than half the size of the entire field, only a single box can uniquely fit inside of the image, making the standard deviation of the averages for all box sizes from 200 to 400 μm zero. Ultimately this means that the standard deviation method is only well suited to measure an RVE that is considerably smaller than the field of view (at most half the size of the field of view). Fig. 4.3, which corresponds to the same process but now applied to sample 2, illustrates a case where this limitation makes the standard deviation method unsuitable for obtaining a measurement of the strain-based RVE size. Fig. 4.3a shows the residual plastic strain field from sample 2 after unloading, while the plot in Fig. 4.3b was obtained following the same procedure of dividing the strain field into a grid of boxes of varying sizes. It is clear from

[2] From this point forward, RVE sizes are always reported as a single value, which should be understood as the side of a 2D squared box.

Fig. 4.3b that the standard deviation method is not well suited to measure the RVE size of sample 2, since it is difficult to fit a line to the trailing end of the plot. This happens because the RVE size of sample 2 is close to half the field of view, as will be seen from the other methods below. In fact, even in Fig. 4.2b the line does not reach a plateau even though in both cases, Fig. 4.2 and 4.3, at 400 μm box size we do recover the average stain, indicating the actual RVE size is less than at least 400 μm.

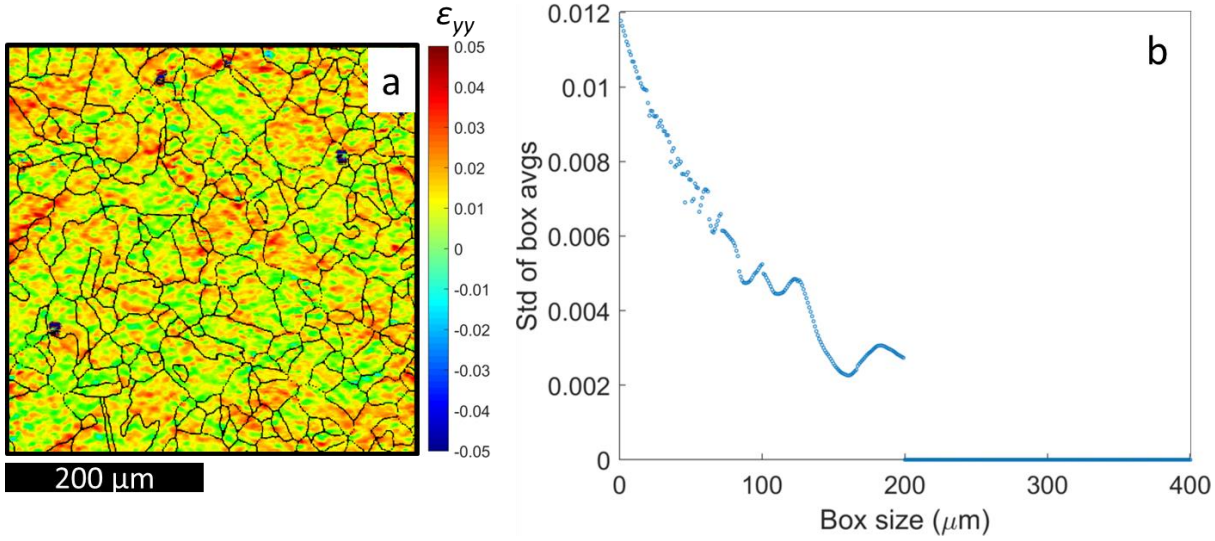

Fig. 4.3. (a) Strain field obtained for sample 2; (b) The plot of standard deviation of box average strains vs. box size (The standard deviation method is not well suited to measure the RVE size of this sample).

4.2.2 Centered Box Growth Method

The second method explored here follows what was proposed by Ravindran et al. (2017), and will be referred to as the "centered box growth method". As the chosen name suggests, the method uses a single square box grown from the center point of the strain field and investigates the evolution of the average strain inside the box as a function of the growing box size. The RVE size is then determined by evaluating convergence of the average strain within some margin of

error. Fig. 4.4 shows how this method can be applied to sample 2. A box starts from the center pixel of the strain field and has its size increased from a single pixel to a box that spans the entire field of view. Fig. 4.4a shows the centered box of size 140 μm overlaid on the strain field, and Fig. 4.4b shows the average strain inside the box plotted vs. the box size. A ±5% margin is used to check for convergence of the average strain to the global average of the strain field (the average macroscale strain accumulated in the sample, measured by *in situ* DIC). The point beyond which the average strains converge to within 5% the global average (around 140 μm for the sample 2) is taken as the RVE size.

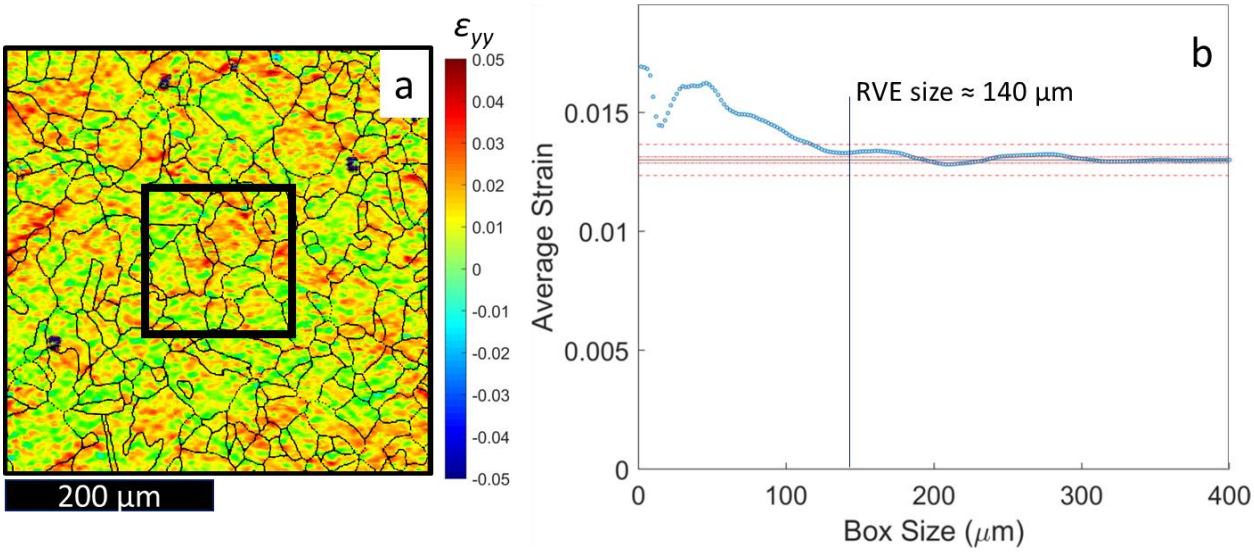

Fig. 4.4. (a) Strain field obtained for sample 2, superimposed by a centered box of size 140 μm; (b) Plot of average strain vs. box size, used to measure the RVE size from convergence to the global average.

The main advantage of this method is that it will produce an estimate of the RVE size as long as the field of view is itself at least about 1.2 times the size of an RVE. This means that the centered box growth method can be applied with a field of view almost half the size of that required by the standard deviation method. However, the main weakness of this method is also a byproduct of its main advantage: using a single box grown from the center of the field of view makes the

method highly dependent on the location and distribution of strains within the field of view. Fig. 4.5 shows the application of the centered box growth method to sample 1, for which it fails to produce a realistic RVE measurement. Fig. 4.5a shows the strain field for sample 1 superimposed by a 10 μm centered box (the box is very small and hard to see, which reinforces how this is an unrealistic RVE size), while Fig. 4.5b shows the plot of average box strain vs. box size. The main weakness of the method is evident in Fig. 4.5b, where the average strain inside the centered box coincidentally converges to the global average at a very small box size. The distribution of the strains within the field of view, as well as the fact that the center pixels of the strain field for sample 1 are close to the average, cause this clearly erroneous measurement of a 10 μm RVE. Statistically speaking, finding an RVE size of 10 μm for this sample is an anomaly that happens because of the random nature of microstructural distributions.

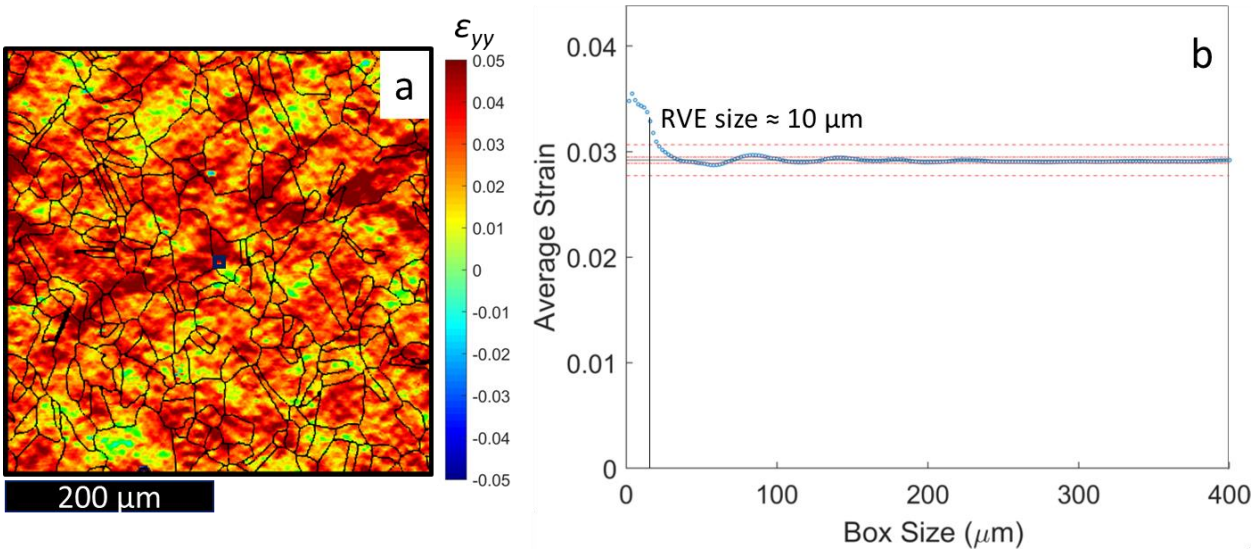

Fig. 4.5. (a) Strain field obtained for sample 1, superimposed by a centered box of size 10 μm; (b) Plot of average strain vs. box size, used to measure the RVE size from convergence to the global average (The centered box growth method is not well suited to measure the RVE size of this sample).

Appendix B presents a more in-depth study about the advantages and disadvantages of both the standard deviation and the centered box growth methods, along with some attempts to

circumvent those disadvantages by modifying each method individually. The decision to develop a separate and new experimental method to measure the strain-based RVE was made after the conclusion from that study that the RVE should be treated as a statistical entity. This conclusion is illustrated by Fig. 4.6 (reproduced from Appendix B), where the centered box growth method was applied to 1,000 different synthetic strain fields (generated as discussed in the next section 4.3.1), with the resulting average strain vs. box size plot showing the high variability of strain-based RVE size results. The next section will go over the details of the new method developed in the present work that considers variability, by approaching the RVE size as an inherently statistical entity.

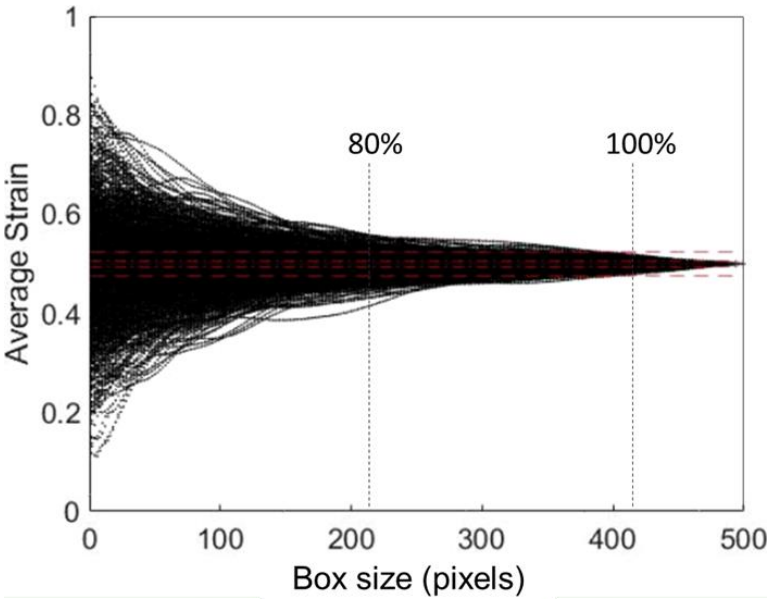

Fig. 4.6 Average strain vs. box size plots for 1,000 different synthetic strain fields, with vertical dashed lines showing the box sizes where 80% and 100% of the strain fields converge to within a ±5% margin from the global average.

4.3 Proposed Experimental Stereological RVE Measurement Method

The method proposed here, which exploits the advantages of considering the box average approach while circumventing the weaknesses of both previous methods, is able to measure the strain-based RVE size from strain fields of the order of the RVE size and accounts for the

dependence on the location of the measured strains within the sample. The main idea behind this method comes from the observation of the high variability of results from the centered box growth method (Appendix B), suggesting that there exists a distribution of RVE sizes for a given nominal material at given nominal loading conditions. As discussed above (Section 4.1), previous authors have recognized this statistical characteristic of the RVE (Swaminathan and Ghosh, 2006), but not much effort has yet been made to take it into account in the *experimental* determination of RVE sizes, which most experimental studies have considered as a deterministic quantity. In order to develop a new method that takes this statistical aspect of the RVE into account, a large quantity of strain data for which the RVE size is controllable is necessary. Such a large number of separate datasets is extremely difficult, if not impossible, to obtain experimentally. Therefore, here we will artificially generate highly controllable "strain fields" that are qualitatively and quantitatively similar to those obtained by HiDIC, but for which we can control geometric features so as to control the resulting RVE size. The method will be developed and verified based on these synthetic strain fields, and will then be exercised on experimentally measured data.

4.3.1 Synthetic Strain Fields

The procedure used here to generate controllable synthetic strain fields consists of a simplified version of the fractional Gaussian noise introduced by Mandelbrot and van Ness (1968). Different frequencies of Gaussian noise are generated by taking n by n matrices of random values from the standard normal distribution and smoothing them through spline interpolation to span the size of the final image. Fig. 4.7 shows how single-frequency Gaussian noise can be obtained by a spline interpolation of a 31 by 31 matrix of random values, from the standard normal distribution, to a 500 by 500 pixel image. Then, a synthetic strain fields is obtained by adding different frequency Gaussian noises together, multiplied by a weight factor inversely proportional to the

frequency (i.e., higher frequencies have lower weights). Fig. 4.8 shows how Gaussian noise obtained from matrixes of sizes 500, 250, 125, 62 and 31 can be added together to obtain a synthetic strain field.

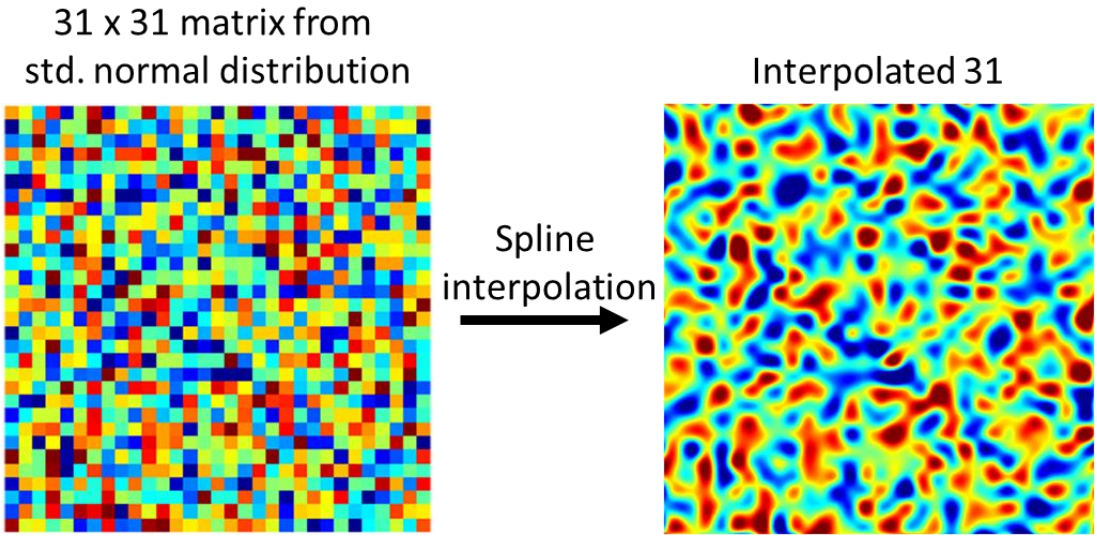

Fig. 4.7. Obtaining one frequency Gaussian noise by spline-interpolating a 31 by 31 matrix of random values, from the standard normal distribution, to a 500 by 500 pixel image.

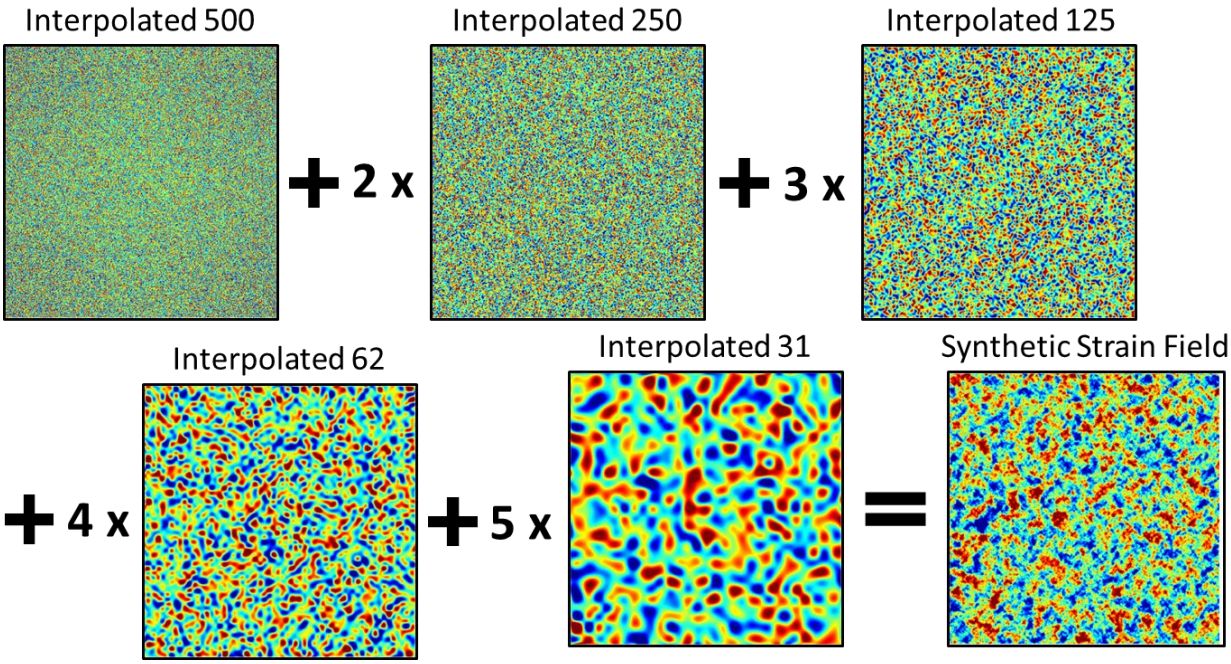

Fig. 4.8. Different Gaussian noise frequencies are added together, multiplied by inversely proportional weights, to obtain a synthetic strain field.

The geometrical scale (which is closely related to the RVE size) of the final synthetic strain field can be controlled by choosing what frequencies of Gaussian noise are added together. Instead of requiring a list of what frequencies were used for each synthetic strain field, a scale factor was introduced as a single parameter that controls the geometrical scale of the synthetic strain fields. Table 4.1 can be used to determine which frequencies are added together for each scale factor. As an example, if a scale factor of 15 was used, the synthetic strain field generated would use only the 500 by 500 random matrix, while for a scale factor of 8, random matrixes of sizes 500, 250, 125, 62, 31, 15 and 10 would be interpolated and added together.

Table 4.1. n values used to generate different frequency Gaussian noise for each scale factor of the synthetic strain fields.

Scale Factor	Frequencies used (matrix sizes)
0	[500,250,125,62,31,15,10,9,8,7,6,5,4,3,2]
1	[500,250,125,62,31,15,10,9,8,7,6,5,4,3]
2	[500,250,125,62,31,15,10,9,8,7,6,5,4]
⋮	⋮
7	[500,250,125,62,31,15,10,9]
8	[500,250,125,62,31,15,10]
⋮	⋮
14	[500,250]
15	[500]

The final step in obtaining synthetic strain fields comparable to the strain fields shown in Fig. 4.1 is to normalize (so that average strain values coincide) and re-plot the synthetic strain fields with the same contour limits. Representative synthetic strain fields for scale factors 6, 8, and 10 are show in Fig. 4.9, illustrating how the scale factor can be used to control the geometric scale

of these fields, which is directly related to the size of the RVE. These fields can be generated at very large quantities, and will be used to develop and verify the proposed new method.

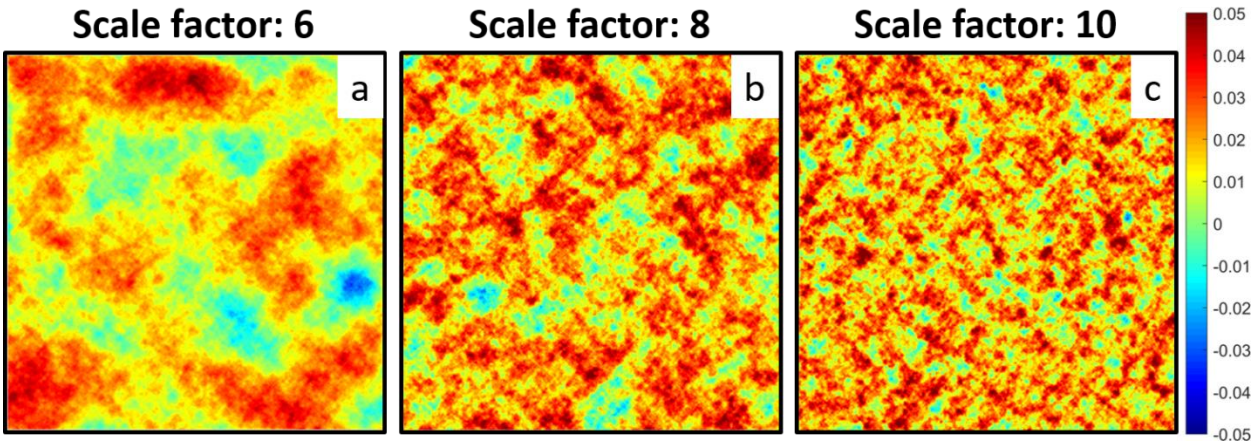

Fig. 4.9. Representative synthetic strain fields for scale factors (a) 6; (b) 8; (c) 10.

4.3.2 Stereological RVE Determination Method

The proposed stereological method consists of taking a very large number (10,000 boxes in the examples shown below) of randomly distributed boxes from within the field of view and plotting a histogram of the average box strains for each box size. Then, the RVE size can be determined through the use of a margin around the global average strain, also allowing for a choice on how strict the measurement should be, by choosing what percentage of the boxes should fall within the margin. Fig. 4.10a shows a synthetic strain field with a scale factor of 8, superimposed by a few randomly distributed boxes of size 191 pixels. Fig. 4.10b shows the histograms obtained by taking 10,000 randomly distributed boxes of sizes 10, 191 and 350 pixels. From Fig. 4.10b it is possible to see that for a box size of 10 pixels, very few (less than 10%) of the boxes fall within the ±5% margin from the global average strain (the average macroscale strain experienced by the sample as measured from *in situ* DIC). With a box size of 191 pixels, 80% of the boxes fall within the ±5% margin, while for a box of 350 pixels 80% of the boxes fall within a ±1% margin of the

global average strain. These can be understood as a confidence level and a margin of error: 80% of the time a box of size 191 pixels will be a strain-based RVE (i.e., will reflect the global average strain), considering a margin of error of ±5% on the strains, or 80% of the time a box of size 350 pixels will be a strain-based RVE, considering a margin of error of ±1% on the strains. Using this inherently statistical approach, we can see how the statistical anomaly results obtained from the centered box growth method could be possible (they could be one of the few boxes that fall within the margin for a small box size).

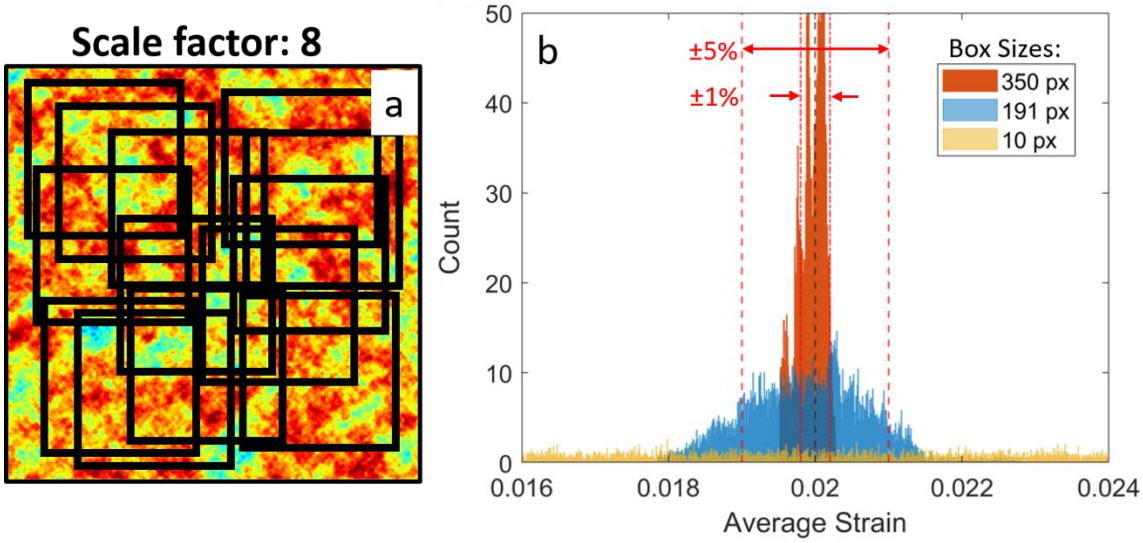

Fig. 4.10. (a) Synthetic strain field with scale factor 8 superimposed by randomly distributed boxes of size 191 pixels; (b) Histograms of average strains for box sizes of 10 pixels, 191 pixels, when 80% of the boxes fall within a ±5% margin from the global average strain, and 350 pixels, where 80% of the boxes fall within a ±1% margin of the global average.

4.3.3 Statistical Equivalence between Stereological and Centered Box Growth Methods

In order to validate the stereological method, it must be shown that it can predict similar RVE sizes as the existing methods, as well as their statistical variation. To this end, the centered box growth method (Ravindran et al., 2017) was applied to 10,000 *different* synthetic strain fields with scale factors from 0 to 10 (using a ±5% margin from global average strains, measured from *in situ* DIC, to judge convergence), with the results obtained for fields of scale factor 8 being

plotted in the histogram shown in Fig. 4.11a. Vertical lines indicate the values for median, average, and the 80% threshold, where for 8,000 of the 10,000 synthetic strain fields the centered box growth method predicts an RVE size of at most 232 pixels (i.e., for 80% of cases 232 pixels is an RVE). With this result (obtained through the use of 10,000 different strain fields) in hand, it is possible to compare the statistical predictions from the centered box growth method to the proposed stereological method. Fig. 4.11b shows a plot comparing the results obtained from the 80% threshold of both the centered box growth (with 10,000 different synthetic strain fields being analyzed for each point) and the stereological method (with 10,000 boxes taken from a single synthetic strain field for each point) for scale factors from 0 to 10.

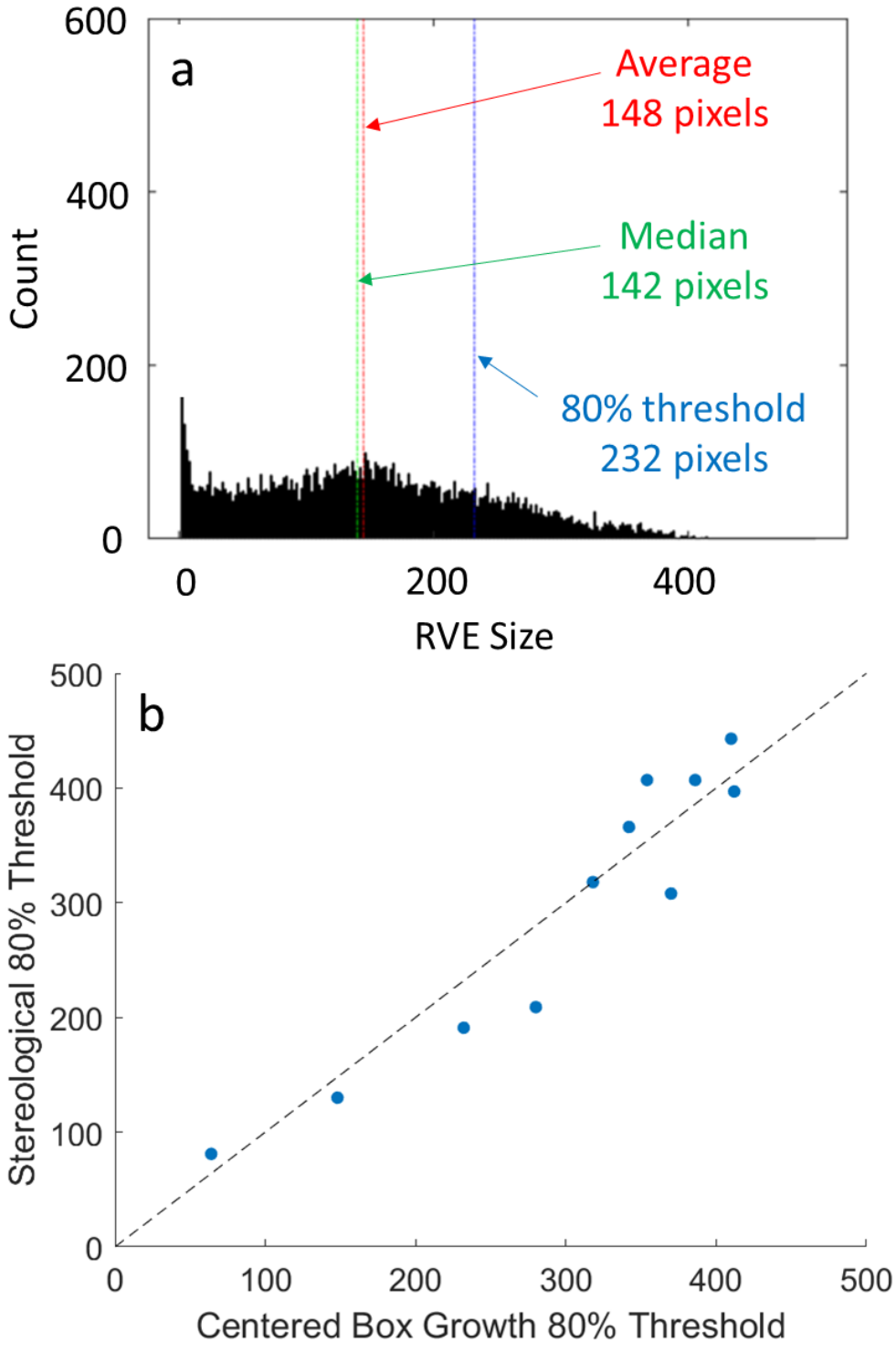

Fig. 4.11. (a) Histogram of the results obtained from the centered box growth method (±5% margin on strains) for 10,000 different synthetic strain fields of scale factor 8; b) Plot of the RVE sizes measured by the stereological method vs. the centered box growth method, both using the 80% threshold and a ±5% margin on strains.

The data points of Fig. 4.11b show that the stereological method produces statistically equivalent results to the centered box growth method, while requiring far fewer data to do so (a single image vs. 10,000 different images). Thus, the main advantage of the stereological method is that by taking into account the statistical variance of the RVE size, the method is able to consistently predict a wide range of strain-based RVE sizes from a single strain field. By producing statistically equivalent results to the centered box growth method and circumventing its main disadvantage, the stereological method becomes the best suited for application to a wide range of strain and spatial resolutions.

4.4 Stereological Method Applied to Experimental Results

The final step in assessing the stereological method is to apply the proposed method to the same experimental data, namely those of Fig. 4.1a where the standard deviation method produced reasonable results but the centered box growth method did not, and those of Fig. 4.1b where the opposite occurred. Fig. 4.12 shows the histograms obtained for sample 1 (Fig. 4.12a) and sample 2 (Fig. 4.12b), using the 80% threshold and a ±5% margin on strains (80% of the 10,000 randomly taken boxes fall within the ±5% margin from global average strains). The insets show the respective strain fields overlaid by a box of size equal to the measured RVE.

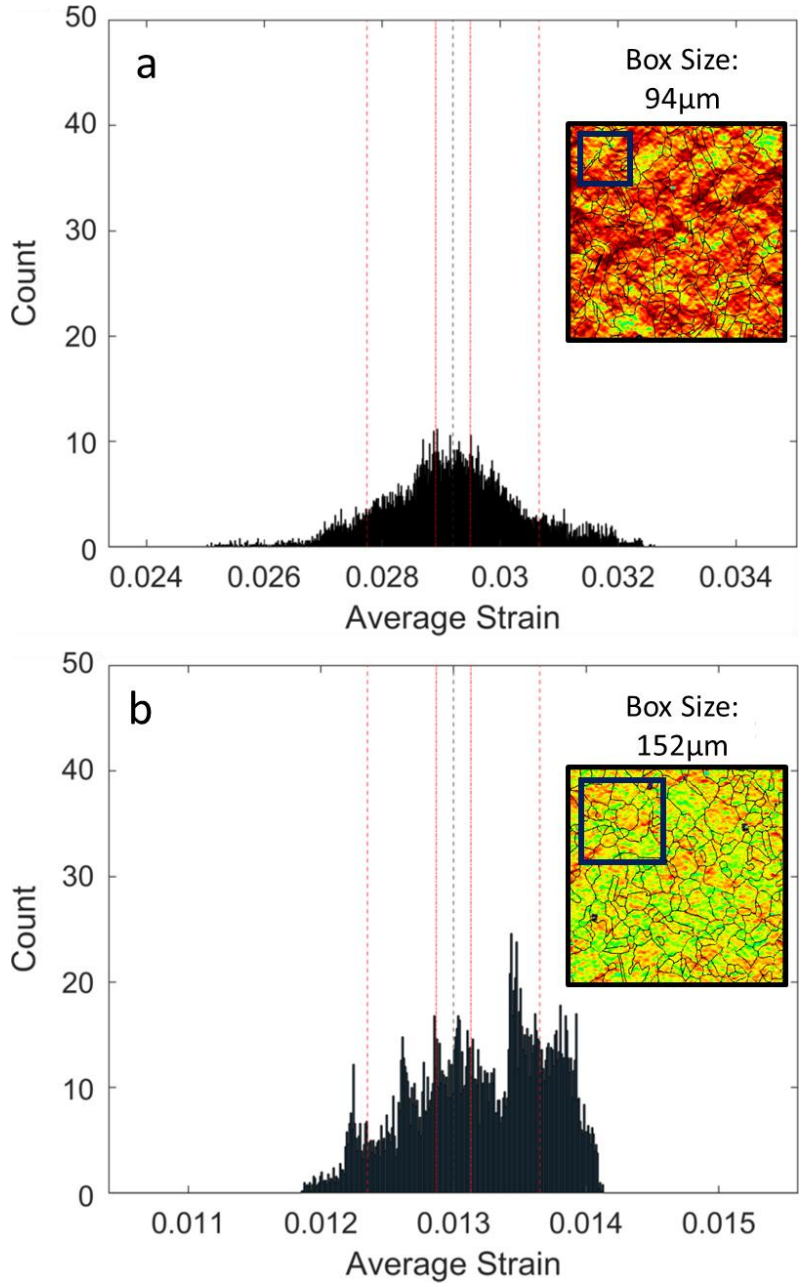

Fig. 4.12. Stereological method plots for (a) sample 1 and (b) sample 2; insets show the respective strain fields with the obtained RVE sizes drawn (the RVE size was taken at the 80% threshold considering a ±5% margin on strains).

Table 4.2 shows the resulting strain-based RVE sizes obtained for each sample from each of the three discussed experimental methods. The stereological method was successful in measuring the RVE size for both samples, while the standard deviation method failed to produce an estimate for sample 1 and the centered box growth method resulted in a unrealistic prediction

for the result of sample 2. These results show that not only is the stereological method a more robust way of experimentally measuring the size of the strain-based RVE, but also that it is a more flexible method, capable of being adjusted to match the desired strictness level of the measurement, by choosing a different threshold value or a tighter margin for the strains.

Table 4.2. Strain-based RVE sizes measured for two samples using each of the three discussed methods.

Measured RVE Sizes

	Standard Deviation method	Centered box growth method (±5% margin from global avg. strain)	Stereological method (80% threshold, ±5% margin from global avg. strain)
Sample 1	100 μm	10 μm	94 μm
Sample 2	-	140 μm	152 μm

For the purposes of comparing the stereological method with the two prior methods which offer deterministic RVE results, all the strain-based RVE sizes quoted above in Table 4.2 and all those subsequently reported in this work were taken using the 80% threshold and a ±5% margin from the global average strain. However, the stereological method is much more powerful and can in fact be used to generate a probability distribution for the size of the strain-based RVE. If instead of choosing a priori a threshold and interrogating the strain field to determine what box size converges to the global average (within a chosen margin which for example can be based on experimental noise levels), we do the opposite and calculate what percentage of the 10,000 randomly selected boxes fall within the chosen margin, a probability distribution can be plotted. Fig. 4.13 shows the plot for the probability that the box average strain falls within ±5% and ±1% margins from the global average strain for each box size in sample 2 (Fig. 4.1b). The 80% threshold line is shown, for reference, but this plot makes it clear how the stereological method could be

used with different combinations of threshold and margin to produce more (or less) strict strain-based RVE size measurements.

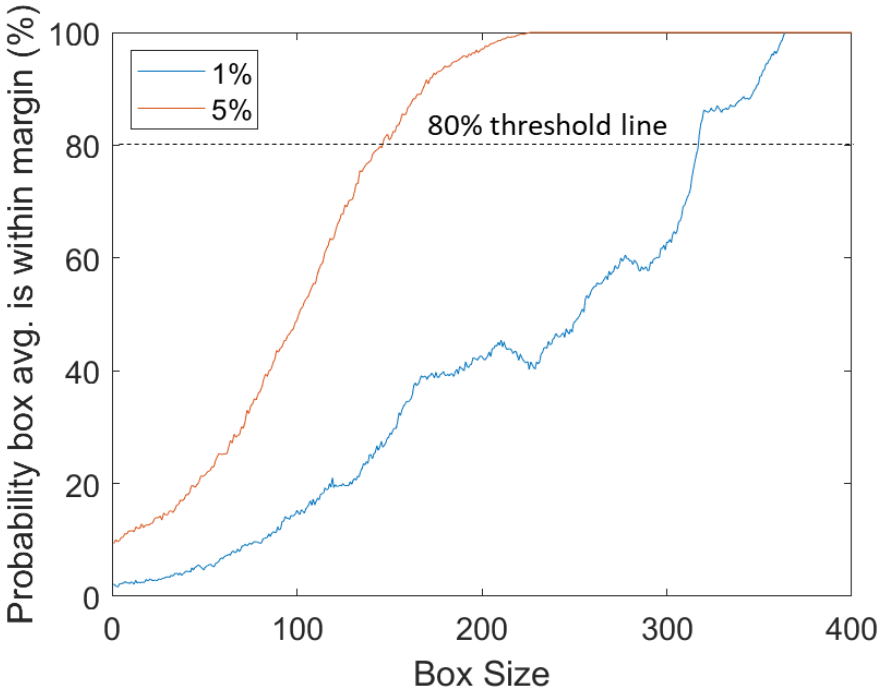

Fig. 4.13. Probability that the average strain from a random box falls within the global average strain vs. box size, for ±5% and ±1% margins.

4.5 Summary

This chapter proposed a new, robust method of experimentally measuring strain-based RVEs from high-resolution strain fields obtained from applying the HiDIC technique described in Chapter 3. A review of two previously proposed methods was presented, namely the standard deviation (Efstathiou et al., 2010) and the centered box growth (Ravindran et al., 2017) methods. The main disadvantages of each of these two methods were revealed from their application to experimental data, namely: the need for a relatively large field of view for the standard deviation method; and the susceptibility of the centered box growth method to produce unrealistic RVE measurements depending on the precise details of the starting location. The proposed stereological method uses the statistical nature of the RVE coupled with a large number of randomly collected

boxes, to produce more reliable measurements along with quantitative control over (statistical) tolerances on the RVE. In the development and validation of the stereological method, controllable synthetic strain fields obtained from Gaussian noise allowed the generation of large quantities of data, similar to experimental strain fields, but easily controllable by an adjustable scale factor that directly correlates with the resulting RVE size. These synthetic strain fields were used to demonstrate the statistical equivalence between strain-based RVE measurements obtained from the stereological method and the centered box growth method, thus validating the results produced by the stereological method. All three methods were applied to real experimental results, with the stereological method being capable of producing reliable measurements in all cases, while both the standard deviation method and the centered box growth method failed to generate reliable measurements in some of the cases. The next chapter will go over the application of the stereological method to investigate the influence of loading parameters (e.g., temperature, maximum stress and hold times) on the size of the strain-based RVE.

Chapter 5: Representative Volume Elements for Plasticity and Creep Measured from High-Resolution Microscale Strain Fields [3]

As seen in Chapter 3 and 4, during loading of polycrystalline metals strain accumulates at specific locations at the microscale, producing highly inhomogeneous strain fields. Such heterogeneities can ultimately be attributed to the underlying mechanisms of deformation that govern the interactions between the anisotropic grains. Therefore, the degree of inhomogeneity, in addition to microstructure, may also be a function of the loading parameters (e.g., maximum stress, temperature, hold times, etc.) to which the material is subjected. This chapter presents an experimental study on the influence of these loading parameters on the size of the Representative Volume Element (RVE), using the method proposed in Chapter 4 to measure strain-based RVEs from the microscale strain field obtained using HiDIC. The local accumulation of strains near grain boundaries is also analyzed through a pertinent coordinate frame transformation, with the influence of temperature on the underlying creep mechanisms being identified as one of the main driving forces behind changes in the RVE sizes.

5.1 Background

A number of experimental studies regarding micro and mesoscale strain inhomogeneities in titanium e.g., (Efstathiou et al., 2010), copper e.g., (Delaire et al., 2000) and aluminum e.g., (Raabe et al., 2001) have shown the development of plastic heterogeneity at the grain level. Many such experimental studies have been used to validate corresponding numerical models, such as

[3] This Chapter is an expanded version of Vieira et al. (2021)

crystal plasticity simulations, through homogenization techniques capable of extrapolating the macroscopic response of the material from the predicted microscopic response (Roters et al., 2010). As discussed in Chapter 4, the central concept of many such techniques is the Representative Volume Element (RVE), which can be understood as the smallest volume of material that reproduces a characteristic of the bulk. This characteristic can be microstructure-based or property-based, and the size of the RVE can change greatly depending on which characteristic needs to be homogenized.

An extensive series of studies regarding the determination of RVE length scales have been published in the literature, with a wide range of results. A majority of these studies were conducted through numerical approaches that usually determine the RVE size through homogenization techniques, where the result obtained from a simulation has to converge to the macroscopic result for a large enough simulation box (Salahouelhadj and Haddadi, 2010; Bouchedjra et al., 2018; Nakamachi et al., 2007; Ranganathan and Ostoja-Starzewski, 2008). Experimental studies, such as the one conducted by Efstathiou et al. (2010), are far fewer. Efstathiou et al. (2010) experimentally determined (using the "standard deviation method" discussed in Chapter 4) the RVE size of a plastically loaded titanium alloy to be ~30 times the average grain size. Ravindran et al. (2017) presented an overview of RVE sizes obtained for different polycrystalline materials. They also proposed their own method of experimentally measuring RVE sizes (the "centered box growth method" discussed in Chapter 4), finding that, for a plastically loaded carbon steel, the RVE size was 8.85 times the average grain size. More recently, Stinville et al. (2016, 2017) experimentally measured RVE sizes of a nickel superalloy for plastic strain localization (~9 times the average grain size) and fatigue crack initiation (~34 times the average grain size), pointing to the possibility that the size of the RVE depends on the investigated property, as well as on the

loading parameters. Yang et al. (2019) predicted RVE sizes for viscoplastic properties of FCC Cu to be consistently larger than those for elastic properties, thus concluding that loading parameters such as stress play a role in the RVE size. Therefore, RVE sizes can be property-dependent as well as load-dependent, and ultimately mechanism-dependent.

The following sections describe the experimental determination of strain-based RVE sizes under different plasticity and creep loading conditions, with the objective of correlating the strain inhomogeneities found at the microscale with the macroscopic behavior of the material. The influence of temperature, maximum stress, and hold times on the size of the RVE is determined to be due to changes on the underlying deformation mechanisms.

5.2 RVE Measurements for Different Load-Temperature Conditions

In order to explore the effect of different loading conditions on the inhomogeneous microscale strain field and the changes in RVE size resulting from them, dog-bone samples were tested under different loading histories that can be divided into three types: ***plasticity*** when the sample was subjected to a stress above macroscopic yield at the test temperature, without being subjected to any amount of hold time before unloading; ***elastic creep*** for a loading step in which the sample was loaded *below yield* at the test temperature, being subjected to some extent of hold time at maximum stress; and the combination of plasticity and creep, where a sample was loaded *above yield* at the test temperature and subsequently subjected to some hold time at maximum stress in what we will refer to henceforth as ***plastic creep***. (Although all strains measurements presented here are residual plastic strains, the nomenclature “elastic creep” vs. “plastic creep” is adopted to distinguish the stress level at which creep takes place.) Fig. 5.1 shows schematic stress vs. strain curves displaying the characteristics of the three different types of loading investigated.

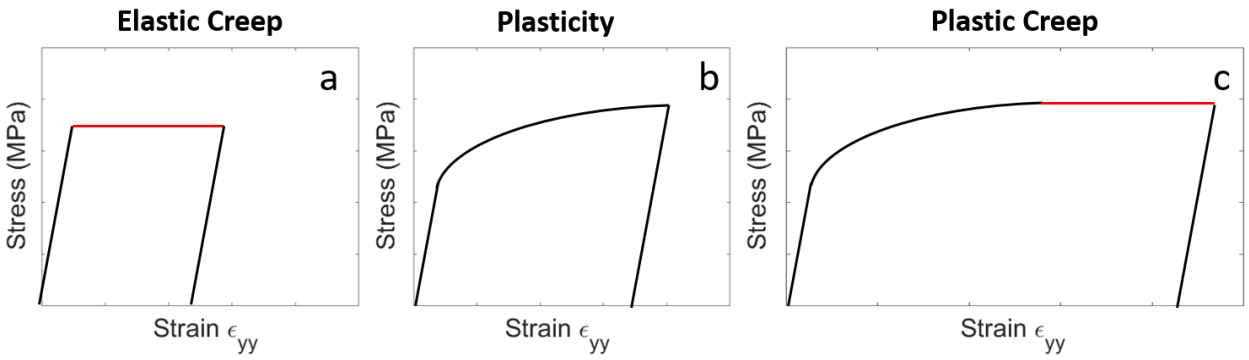

Fig. 5.1. Schematic stress-strain curves of the three types of deformation investigated; (a) Elastic creep; (b) Plasticity and (c) Plastic creep. Red denotes hold a time at the maximum stress level.

The particular loading parameters involving these three types of loading for a number of specific cases investigated here are listed in Table 5.1. By varying the maximum stress and the temperature during loading, each sample was subjected to a different deformation type, as listed in the table. The maximum stresses were taken at 25% above or below the macroscopic yield stress for a given temperature depending on whether initial bulk plastic deformation was desired or not. The yield stress at room temperature (RT) was measured to be 315 MPa, while at 300°C it was 285 MPa, 200 MPa at 500°C and 110 MPa at 800°C.

Table 5.1. Loading parameters used for each sample.

Sample	Temperature (°C)	Max Stress (MPa)	Hold Time (min)	Deformation type
1	RT	400 (~25% above yield)	0	Plasticity
2	RT	400 (~25% above yield)	60	Plastic Creep
3	300	215 (~25% below yield)	60	Elastic Creep
4	300	350 (~25% above yield)	0	Plasticity
5	300	350 (~25% above yield)	60	Plastic Creep
6	500	150 (~25% below yield)	60	Elastic Creep
7	500	250 (~25% above yield)	0	Plasticity
8	500	250 (~25% above yield)	60	Plastic Creep
9	800	80 (~25% below yield)	60	Elastic Creep

5.2.1 Residual Strain Fields for Different Load-Temperature Conditions

After loading, each sample enumerated in Table 5.1 was removed from the load frame and placed under an optical microscope to have a set of deformed images taken. The result from the subsequent HiDIC correlation of the stitched images is a set of residual surface strain fields, as for example shown in Fig. 5.2 for sample 1. Fig. 5.2a shows a smoothed stress-strain curve of the axial loading to which sample 1 was subjected, at room temperature (RT), with a maximum stress ~25% above yield (400 MPa) and with no hold time leading to plastic deformation. Fig. 5.2b shows the residual axial strain (ε_{yy}) field after loading.

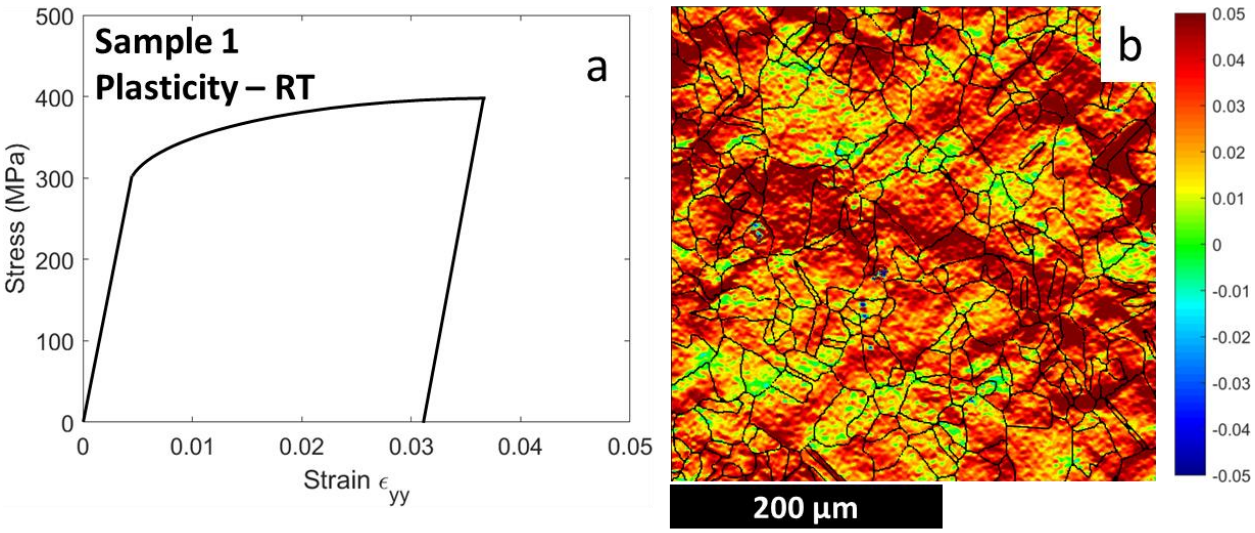

Fig. 5.2. (a) Stress-strain curve for sample 1 at room temperature; (b) Residual axial strain field (ε_{yy}) obtained after loading.

From Fig. 5.2b we, again, see that strains accumulate at preferential locations, resulting in a highly inhomogeneous residual strain field. Furthermore, the residual strain levels at specific points reach values much higher than the macroscopic strain, with the maximum local strain measured being at around 8% (0.08), while the macroscopic strain is just above 3% (0.0309). Finally, as has been discussed in Chapter 3, grain boundaries appear to present "hot-spots" for strain accumulation. Fig. 5.3 shows the equivalent plots for sample 2, which was subjected to loading at room temperature, with maximum stress of 400 MPa (~25% above yield) and held for 60 minutes, i.e., it underwent plastic creep at room temperature. By comparing Fig. 5.3 to Fig. 5.2, a few observations can be made. Strains still appear to be primarily concentrated near grain boundaries, with higher strains being measured overall. The higher macroscopic strain, result of the hold time to which the sample was subjected, caused the average measured strain to rise to about 4% (0.0412), but the maximum value of strain obtained didn't rise as much, staying close to 8% (0.0823).

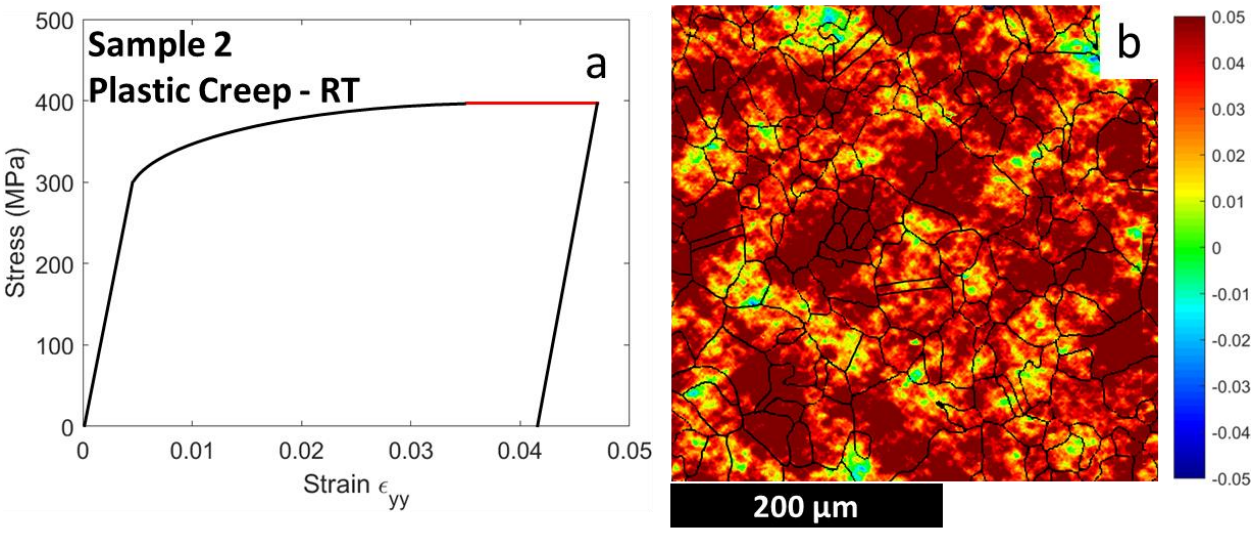

Fig. 5.3. (a) Stress-strain curve for sample 2 at room temperature; (b) Residual axial strain field (ε_{yy}) obtained after loading.

For the samples tested at 300°C, the equivalent plots are shown in Fig. 5.4. The stress-strain curves for sample 3, 4 and 5 are shown in Fig. 5.4a, c and e, respectively, while the residual strain fields are shown in Fig. 5.4b, d and f. The result for sample 3, loaded at 215 MPa (~25% below yield at 300°C) with one hour hold time, shows lower average strain levels (than the RT experiments), with strain accumulation happening largely at the vicinity of grain boundaries. The strain field (Fig. 5.4b) has average strain at about 1.3% (0.0134) and maximum strain values at around 3% (0.0311). The result for sample 4, loaded at 350 MPa (~25% above yield at 300°C) with no hold time, shows average strain levels below those obtained for sample 1, indicating that even though both samples were loaded at about 25% above yield (at their respective temperatures), the 400 MPa loading at room temperature resulted in higher strains. The strain field obtained for sample 4 (Fig. 5.4d) again presents high strain concentrations near grain boundaries, with an average strain level around 2% (0.0212) and a maximum measured strain of around 5.5% (0.0562). Sample 5 was also loaded at 350 MPa (~25% above yield at 300°C), but with an hour hold time, leading to average strains lower than those obtained for sample 2, which indicates again that the

400 MPa loading at room temperature resulted in more straining than the 350 MPa loading at 300°C. The strain field (Fig. 5.4f) has an average strain level around 3% (0.0298) with a maximum strain close to 7.5% (0.0744).

Similarly, Fig. 5.5 shows the stress-strain curves and residual strain fields for samples 6 (Fig. 5.5a and b), 7 (Fig. 5.5c and d) and 8 (Fig. 5.5 e and f). The results for sample 6 show higher macroscopic strain than that of sample 3, indicating that the loading of 150 MPa for 1 hour at 500°C was more critical than 215 MPa for 1 hour at 300°C, even though both samples were loaded at around 25% below yield (at their respective temperatures). The strain field for sample 6 (Fig. 5.5a) was similar to that of sample 3 (Fig. 5.5a), presenting strain concentrations largely near grain boundaries, with an average strain around 2% (0.0196) and maximum strain around 4% (0.0389). Sample 7, loaded at 250 MPa at 500°C, had higher strain than those from sample 4, pointing again to the fact that loading at 500°C was more critical than at 300°C for loads 25% above yield. The residual strain field for sample 7 (Fig. 5.5d) had an average strain around 2.5% (0.0258), with a maximum strain of around 6.5% (0.0662). Lastly, sample 8 was loaded at 250 MPa for 1 hour at 500°C, resulting in higher strains than those of samples 5 and 7. Again the loading at 500°C is seen as more critical than that at 300°C, and again the introduction of a hold time increased the strain levels. The strain field for sample 8 (Fig. 5.5f) presented an average strain around 3.5% (0.0366) with maximum strains around 7.5% (0.0772).

Finally, the plots obtained for sample 9 are shown in Fig. 5.6. The loading of 80 MPa (~25% below yield) for 1 hour at 800°C, resulted in the highest strain for elastic creep (higher than samples 3 and 6), following the trend that an increase in temperature resulted in more critical loading conditions. The average strain in Fig. 5.6b was close to 3% (0.0291), with maximum strain around 6.5% (0.0639).

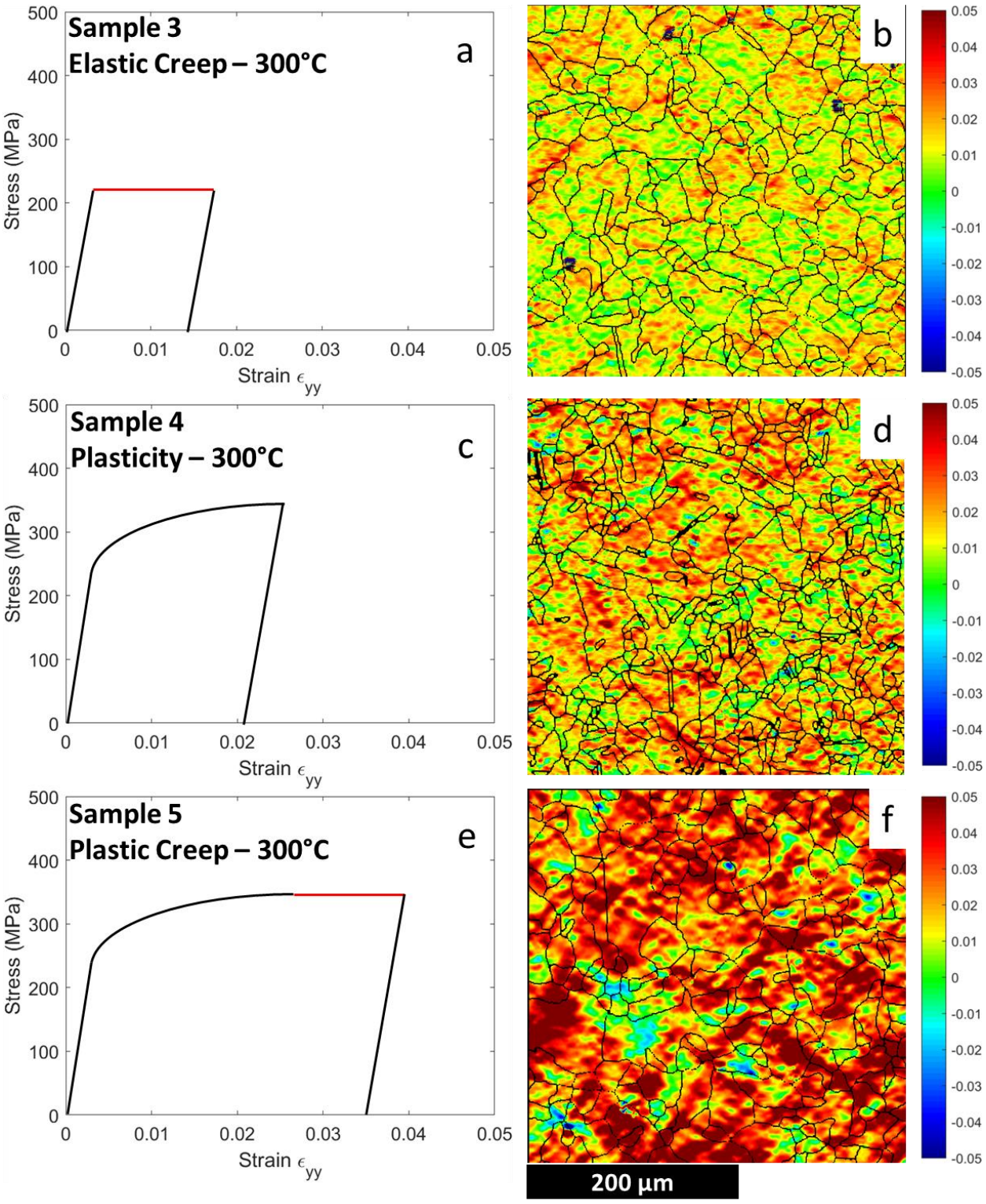

Fig. 5.4. Stress-strain curve for samples (a) 3, (c) 4 and (e) 5 at 300°C; Residual axial strain field (ε_{yy}) obtained after loading for samples (b) 3, (d) 4 and (f) 5.

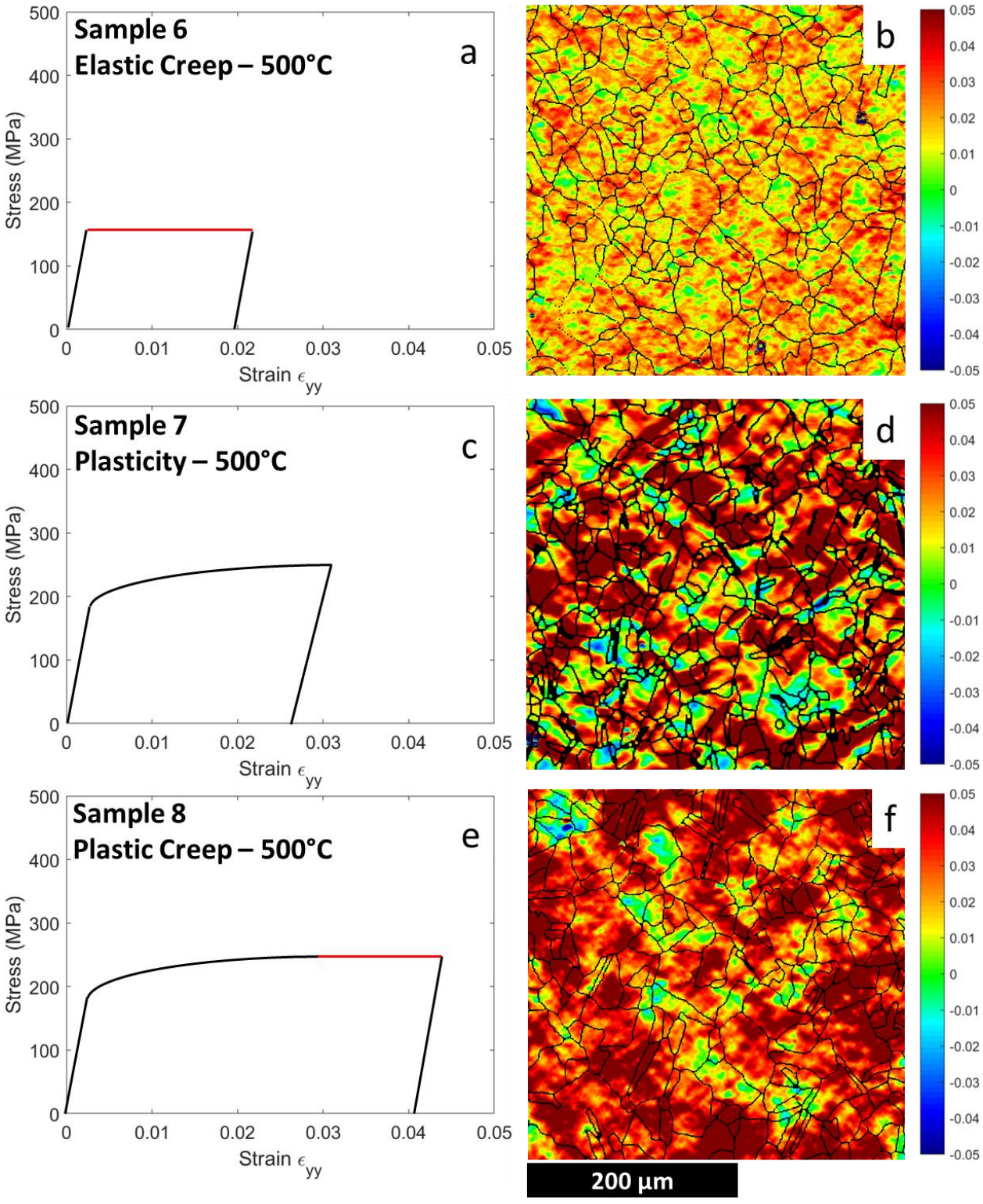

Fig. 5.5. Stress-strain curve for samples (a) 6, (c) 7 and (e) 8 at 500°C; Residual axial strain field (ε_{yy}) obtained after loading for samples (b) 6, (d) 7 and (f) 8.

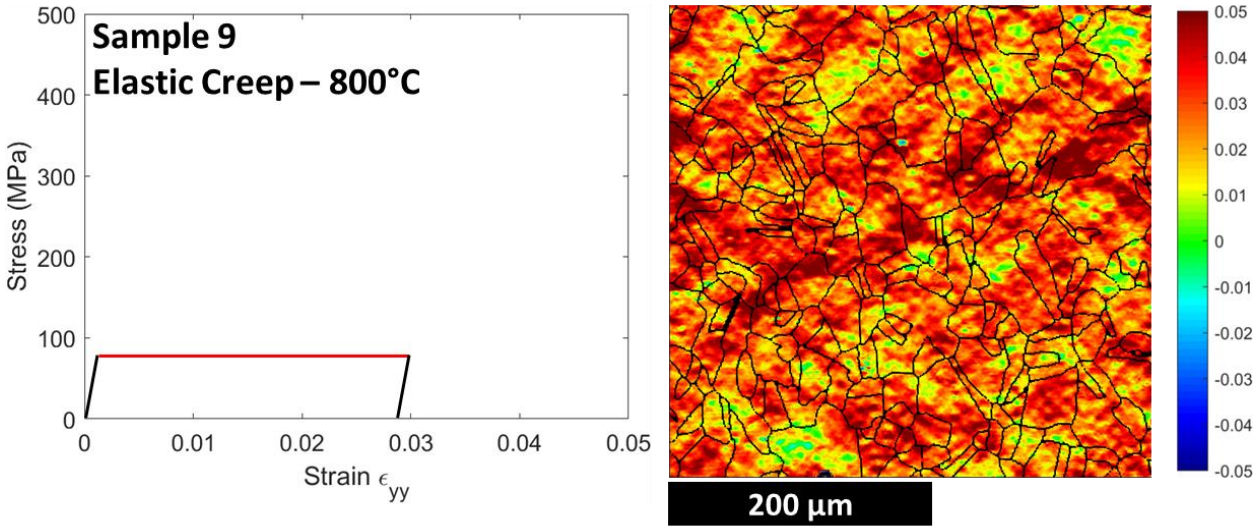

Fig. 5.6. (a) Stress-strain curve for sample 9 at 800°C; (b) Residual axial strain field (ε_{yy}) obtained after loading.

Even though these contours show different resulting residual strain fields for different loading conditions, a more quantitative measure of how different these contours and their inhomogeneities are can be achieved by extracting their respective RVE sizes. The dependence of RVE size on deformation type, as well as temperature and stress can be determined by measuring the RVEs of all contours shown in Fig. 5.2 - Fig. 5.6.

5.2.2 RVE Sizes

The stereological method proposed in Chapter 4 was used to measure the strain-based RVE of each of the 9 samples presented here. The 80% threshold was chosen for all samples, considering a ±5% margin from the global average strain, which is the same as saying that 80% of the time that box size will satisfy the condition of converging to the global average strain. These margins could be more (or less) restrictive, and the resulting RVE size would be larger (or smaller), thus maintaining the statistical character of the RVE (Swaminathan et al., 2006). Since the margins used for all samples are the same, a relative comparison between the (statistically computed) RVE in each case is valid. Fig. 5.7 shows a bar plot of the resulting RVE sizes for all of the cases tested,

colored by the deformation type. For simplicity, again, the RVE sizes are reported as a single number, which should be understood as the length of side of the box that satisfies the convergence criterion. The left vertical axis shows the RVE sizes in μm, while the right vertical axis shows the RVE sizes as a multiple of the average grain size (~27 μm).

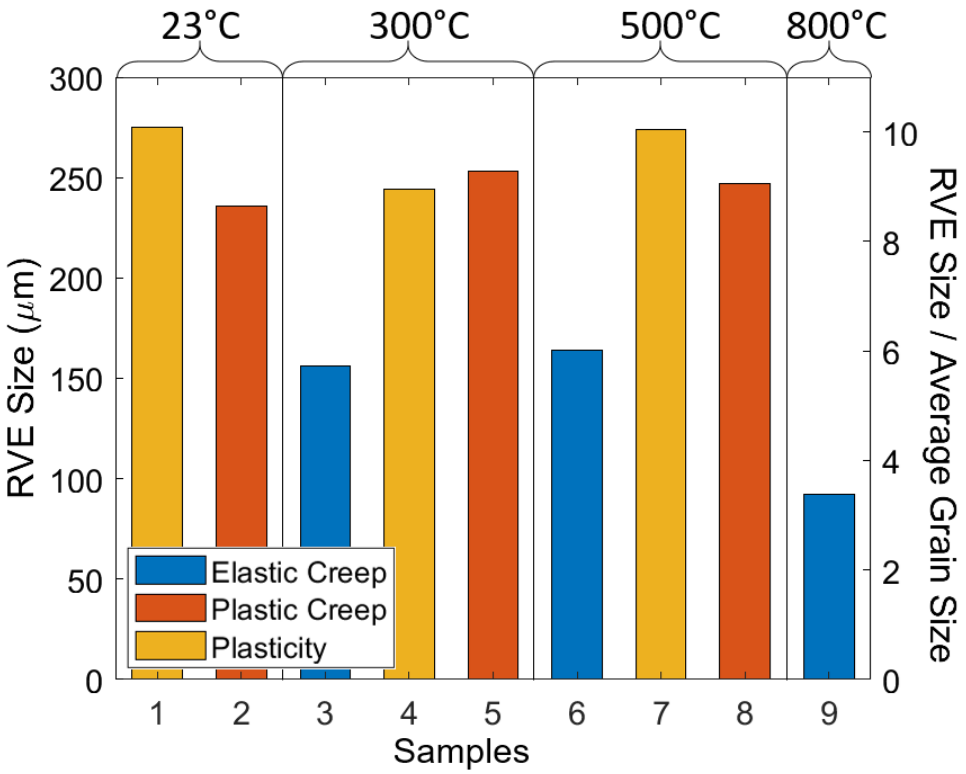

Fig. 5.7. Bar plot of the resulting RVE sizes for each sample, colored by deformation type.

All the measured RVE sizes fall within a range from ~4 to ~10 times the average grain diameter along its side. It is clear that the obtained RVE size for *elastic creep* is considerably smaller than that of *plasticity* and *plastic creep*, which are similar to each other. With the exception of the result obtained for 800°C, the results generally agree with the literature with regards to the size of measured RVEs (6 to 15 times the average grain size) (Liu, 2005) and (Stinville et al., 2016), though the aforementioned studies were at room temperature. Past studies have reported differences between elastic and plastic RVE sizes (Yang et al., 2019), which can be related to the

differences between plasticity (and plastic creep) and elastic creep RVE sizes found here. It is likely that the smaller RVE size obtained for elastic creep can be attributed to the underlying mechanisms of strain accumulation. Finally, the fact that RVE sizes for *plasticity* and *plastic creep* are very similar leads to the conclusion that plasticity dominates the material behavior (at least under these loading conditions) introducing a higher level of inhomogeneities that overshadows the creep response.

In order to investigate how the loading conditions affect the size of the strain-based RVE (potentially due to changes in the underlying deformation mechanisms), the next section recognizes grain boundaries as the primary locations of higher strain concentration (leading to inhomogeneity) and concentrates at the local strains at regions near grain boundaries, specifically aiming to investigate the relative amounts of normal to shear strains near the boundary regions.

5.3 Localized Strain Accumulation at Grain Boundaries

When studying strain accumulation at the microscale, the concept of dividing a grain into two regions, mantle (the part of the grain near the boundaries) and core (the grain interior) is useful. The separation of grains into these two sections is motivated by the assumption that the mechanical response of points far enough from grain boundaries wouldn't be influenced by local effects at the boundaries, while points closer to a boundary would have a response governed mainly by their interaction with the boundary (Meyersm and Ashworth, 1982; Abuzaid et al., 2012). Following this reasoning, to better identify strain accumulation in the mantle regions, strain components in a local coordinate system of the neighboring grain boundaries may be more useful than the axial strains (ε_{yy}) in the global coordinates. Consequently a coordinate transformation from global (sample) coordinates (x, y) to local (grain-boundary) coordinates (normal, n, and tangential, t) is performed based on the EBSD-obtained boundary positions. With this frame rotation it is possible

to visualize more directly what happens at a boundary during loading, specifically since the local normal and shear strains can be understood as neighboring grains being pushed together or attempting to slide against each other. The mantle size (region within which the coordinates are transformed) was estimated at 6-7 μm, or around 20% of the average grain size. This estimate was done by using the same percentage of the average grain size as the one found by Abuzaid et al. (2012), where they used a change in the slope in the plot of strains vs. distance from grain boundary to estimate the mantle size for a nickel superalloy.

The strain coordinate transformation methodology is illustrated in Fig. 5.8. From the EBSD data set of grain boundaries shown in Fig. 5.8a, we selected the closest boundary point (Closest pt. in Fig. 5.8b) to the mantle point of interest (Interrogated pt. in Fig. 5.8b). Subsequently, a set of up to 50 boundary points before and after the Closest pt., shown in red in Fig. 5.8b, are used to fit a line approximating and smoothing the grain boundary section corresponding to the Interrogated pt., which will be taken as the local boundary slope in the vicinity of the point of interest. The reason that we fit a line to a small subset of the boundary near each point, effectively locally smoothing the boundary, is that the noisy local variation of the EBSD-obtained boundaries would produce abrupt changes in local boundary normal that would lead to an extremely unrealistic noise being introduced in the rotated local strain fields. Finally, the angle α (grain-boundary inclination angle) between the fitted line and the horizontal (x axis) is taken as the rotation angle and used in the coordinate transformation. Using this local angle α, which will change as we move along each boundary, we can rotate the DIC-measured strain field from the global (x, y) coordinate system to a local (n, t) coordinates. As illustrated schematically in Fig. 5.8c, the local ε_{nn} normal strain will now represent an extension (or compression) across each boundary and the ε_{tn} shear strain will

represent two grains attempting to slide against each other. This procedure is repeated for every mantle point present in the DIC data, i.e., all the areas denoted by black in Fig. 5.8d.

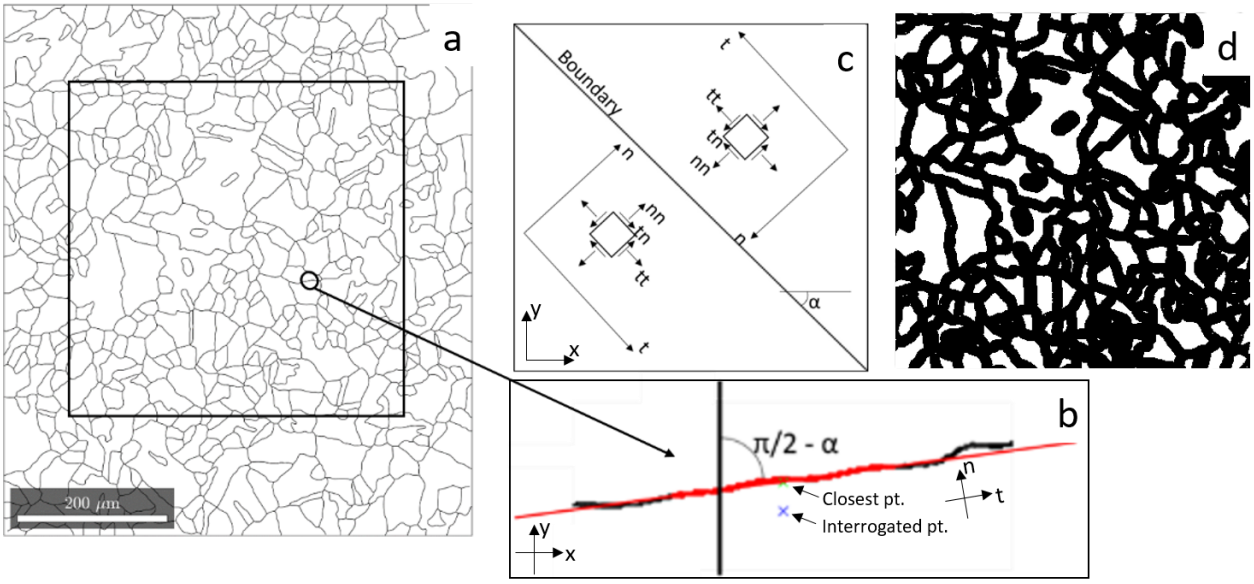

Fig. 5.8. (a) Grain boundaries obtained from EBSD; (b) How the angle *α* is obtained for a specific region of a specific GB; (c) Schematic of the coordinate systems (*x*,*y*) and (*n*,*t*); (d) The separation of mantle (in black) and core (in white).

Fig. 5.9 shows the strain fields before and after the coordinate transformation. Fig. 5.9a and b show the ε_{yy} and ε_{xy} components of residual strains for the entire region of interest; Fig. 5.9c shows contours only within the mantle regions of the same sample of the ε_{nn} (normal to the boundary) component of residual strain (the core is whited out); Fig. 5.9d shows the mantle-only contours of ε_{tn} (shearing the boundary) component of residual strain (again the core is whited out). In order to showcase the advantage of using this coordinate system, Fig. 5.10 shows the magnified view of the boundary marked by the square in Fig. 5.9a. From the local coordinate strains, shown in Fig. 5.10c and d, it is clear that this specific boundary has relatively high residual shear strains and relatively low residual normal strains. This indicates that the two adjacent grains are being sheared against each other, instead of being pushed together or pulled apart. This observation is not as clear when observing the global coordinate strains shown in Fig. 5.9a and b.

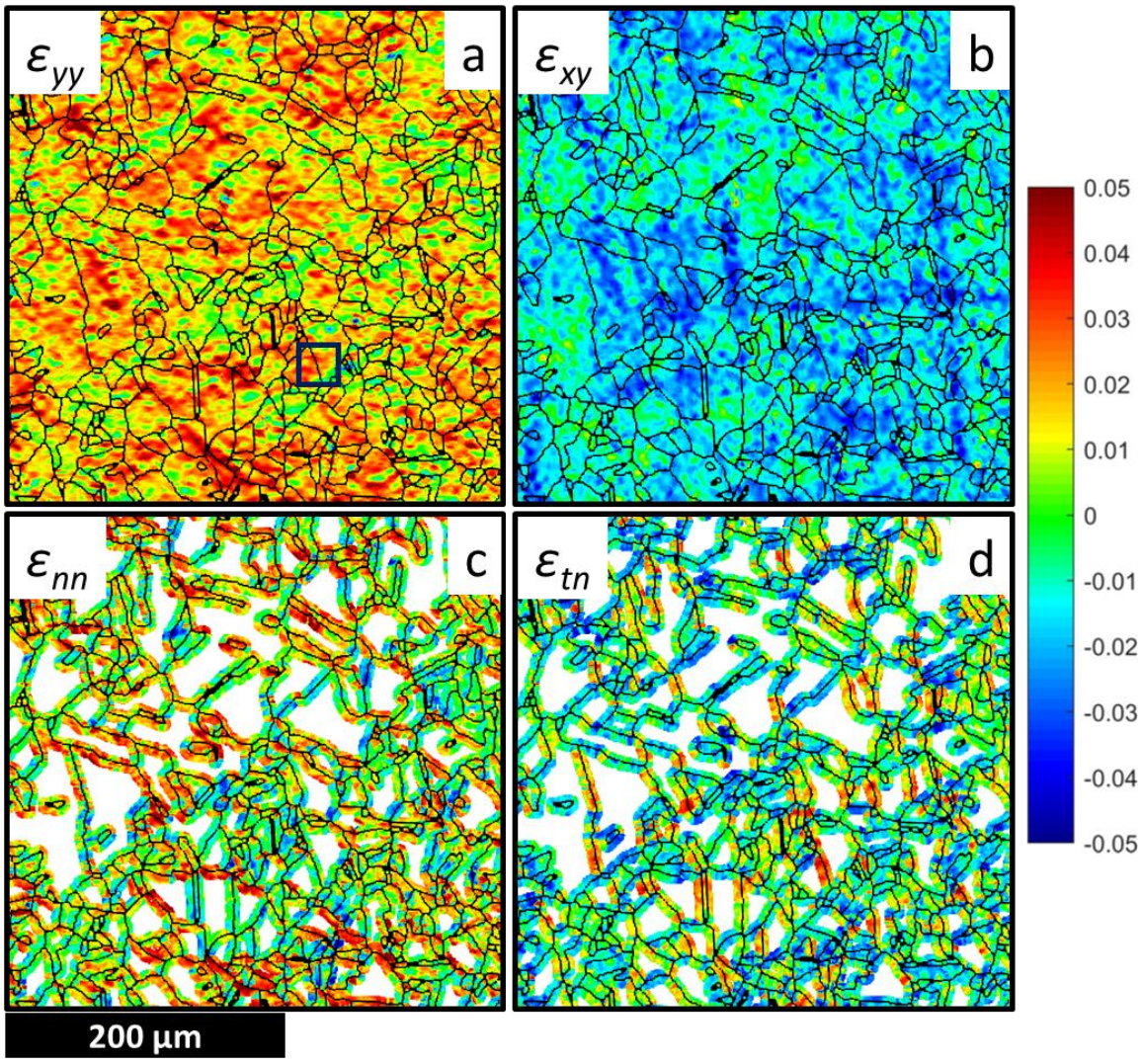

Fig. 5.9. (a) ε_{yy} component of residual strains; (b) ε_{xy} component of residual strains; (c) mantle-only ε_{nn} component of residual strains; (d) mantle-only ε_{tn} component of residual strains.

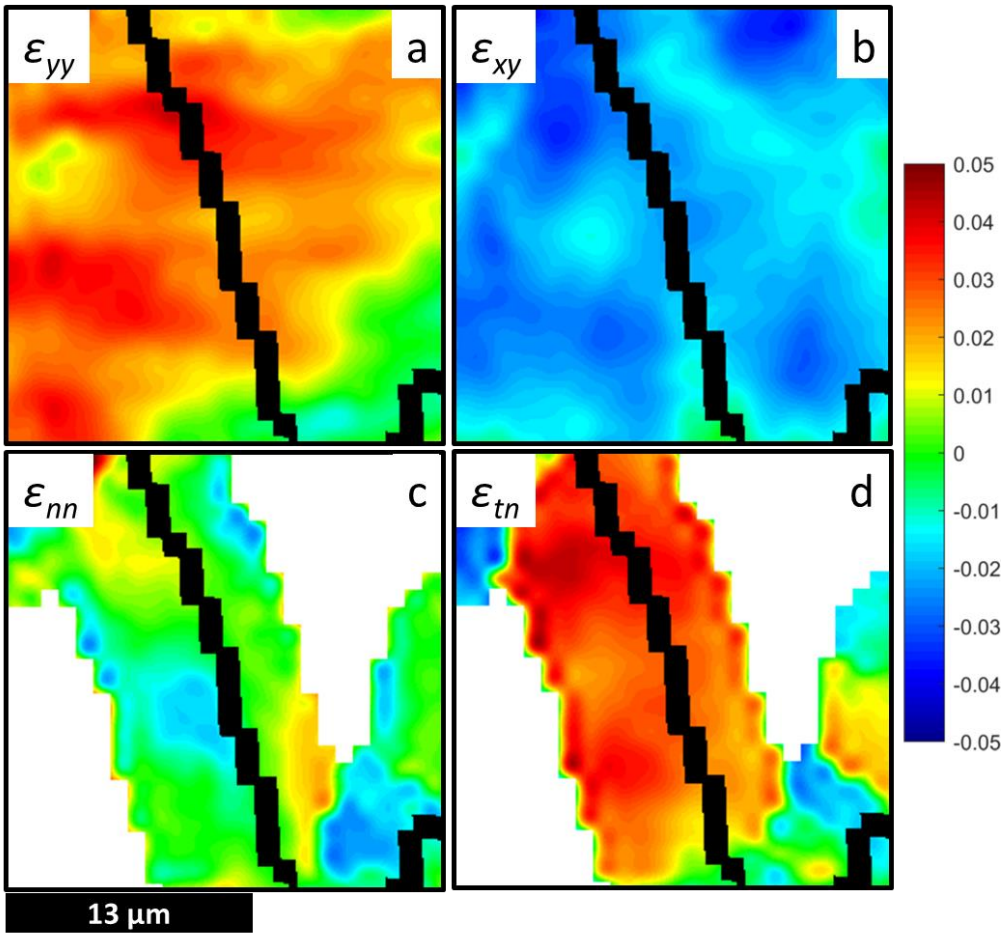

Fig. 5.10. Magnified view of the boundary marked with a square in Fig. 5.9a.

A similar observation can be made about the local behavior at the mantle of each grain boundary. Collectively, and since we have a very large volume of local data form the high-resolution *ex situ* DIC measurements, by looking at all mantles of all grain boundaries contained within the region of interest, a conclusion can be drawn about the dominant deformation around grain boundaries under the different conditions. Fig. 5.11 shows normalized plots of the absolute value of the ratios between normal and shear residual strains ($|\varepsilon_{nn} : \varepsilon_{tn}| \,/\, max(|\varepsilon_{nn} : \varepsilon_{tn}|)$) at every investigated mantle point vs. the corresponding grain-boundary inclination (α), for 3 different *elastic creep* loaded samples at three different temperatures (300°C, 500°C and 800°C). The roughly 50,000 plotted strain ratio points in each case are colored by the misorientation angle

(defined as the difference between the crystallographic orientations of the two adjacent grains) of the corresponding boundary which can be obtained from the EBSD measurements. These results show that there is a relationship between the grain-boundary inclination and the normal to shear strain ratio. Horizontal and vertical boundaries ($\alpha = 0, \pi/2, \pi\ldots$) possess higher ratios (i.e., relatively high local normal strains) while slanted boundaries present lower ratios (relatively high local shear strains). This localization effect at horizontal and vertical boundary inclination becomes more pronounced as temperature increases, as seen by the sharper and narrower peaks in Fig. 5.11c (recall each plot contains about the same number of data points). Unlike what has been reported in some cases previously e.g., (Cheong and Busso, 2006), there is no clear observed correlation between misorientation angle and the local ratio of normal to shear strain: this material contains predominantly twin boundaries which have a misorientation angle of 60° and appear as dark red in Fig. 5.11. As seen from Fig. 5.11, these boundaries corresponding to red points show all levels of strain ratio. Finally, and perhaps most relevant to relating measured local mantle strains to underlying deformation mechanisms, as temperature increases there is a trend indicating that the strains at the mantles become more dominated by shear (i.e., lower overall ratios).

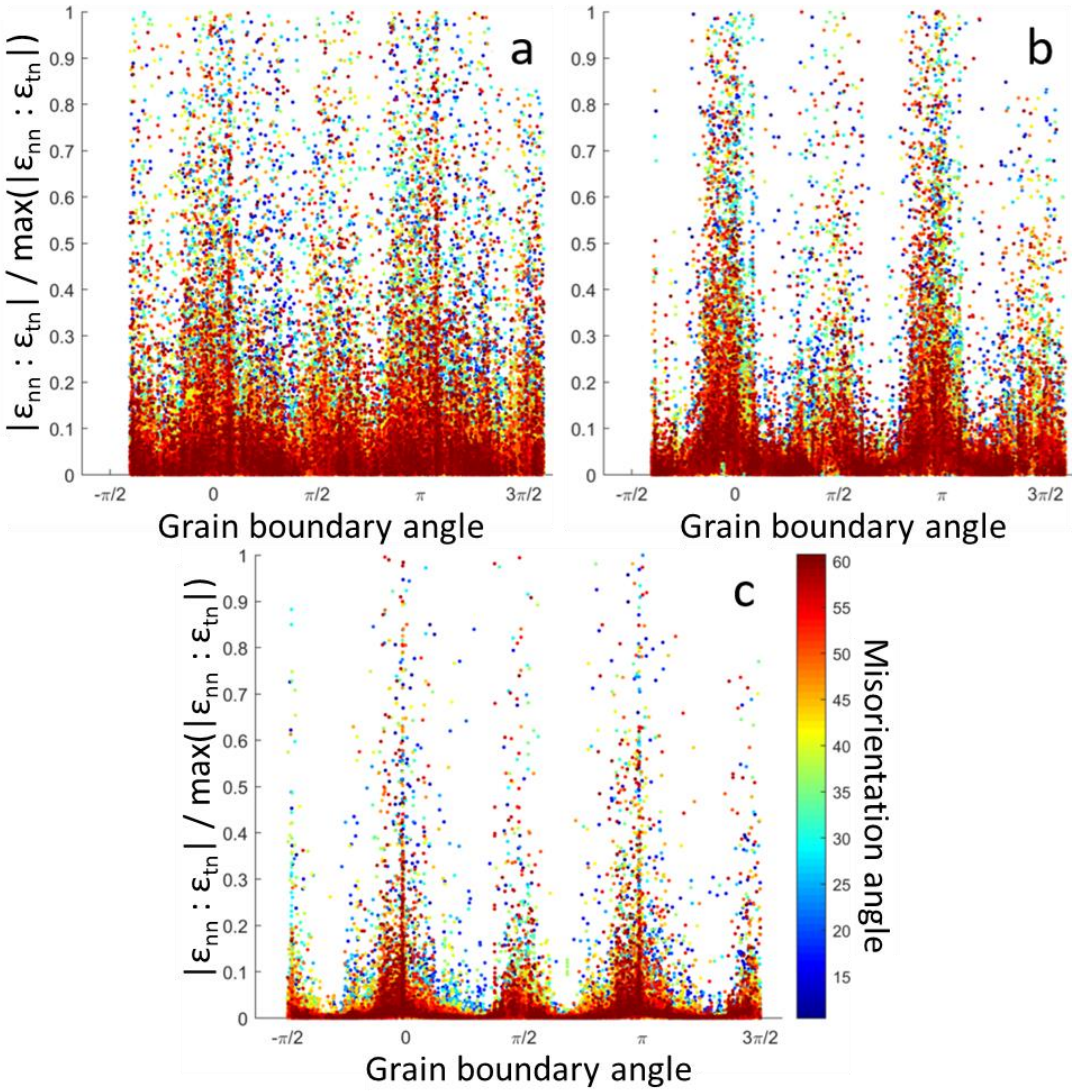

Fig. 5.11. (a) The ratio of normal to shear strains at mantle points vs. the GB inclination (α), colored by the misorientation angle on the closest boundary and normalized by the maximum ratio, for sample 3 (*elastic creep* at 300 °C); (b) sample 6 (*elastic creep* at 500 °C); (c) sample 9 (*elastic creep* at 800 °C).

To obtain a quantitative assessment, the average strain ratio at mantle regions for each case was calculated. Fig. 5.12 shows a bar plot of the average normal to shear strain ratios at the mantle regions for all samples. Here, we see that elastic creep loading presents a much lower average strain ratio than the plastic creep and plasticity cases, regardless of temperature levels. The results for plasticity and plastic creep were very similar, again indicating that plasticity dominates over

creep at the load and temperature levels studied here (~25% above yield strengths for 23°C, 300°C and 500°C). Both these observations are consistent with the discussion from the RVE sizes accompanying Fig. 5.7. In fact, the two bar plots, Fig. 5.7 illustrating RVE sizes and Fig. 5.12 illustrating local strain ratio, are very similar in terms of the interrelations of the three different deformation types. In all cases, samples that had larger RVE sizes also presented higher ratios of normal to shear strains at the mantles. This observation also leads to the hypothesis that the size of the RVE (a measure of residual axial strain inhomogeneity) could be used as a proxy for detecting local mechanism transitions. Strong evidence that also points in this direction comes from the result for sample 9, which presents the lowest RVE size (lower degree of inhomogeneity) as well as the lowest average strain ratios (mantles dominated by shear). This result is corroborated by observations from Alomari et al. (2017) who observed a change in creep mechanism for alloy 709 at around 650-700 °C (from dislocation climb dominated to grain boundary sliding dominated), by fitting power-law creep curves to experimental data at varying temperatures, and following Ashby (1972) to predict the change of creep mechanism from a change in the stress exponent.

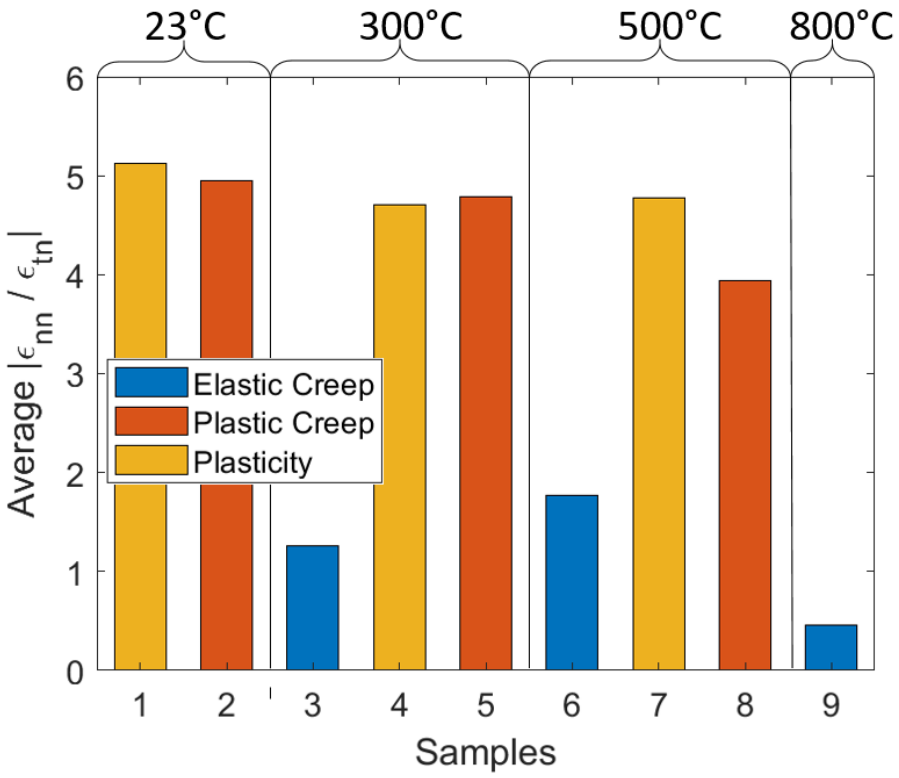

Fig. 5.12. Average strain ratios obtained for all samples, colored by deformation type.

In order to explore further the observation that plasticity seemed to dominate over creep, with plastic creep (essentially an elastic creep deformation on a sample that had been subjected to plastic deformation) RVEs and strain ratios being very similar to those of pure plasticity, the next section will briefly go over another series of samples that were loaded in multiple steps in different orders of deformation/loading types.

5.4 Effects of Cyclic Creep-Plasticity Loading

This section presents a series of experiments conducted to explore the effect of cyclic creep and plasticity loading on the size of the strain-based RVE. The end goal was to eventually correlate RVE sizes with creep-fatigue failure, and because of that, hourglass samples were used in the cyclic experiments. Changing the temperature and keeping the maximum stress at 250 MPa allowed for 5 hourglass samples to be loaded in two steps each, where the elastic creep, plasticity

and plastic creep deformation types were applied in different orders. Table 5.2 shows the loading parameters used for samples 10-14, indicating the temperature, the hold time at 250 MPa and the associated deformation type of each loading step.

Table 5.2. Temperature and hold times for each loading step of samples 10-14.

Sample	1st Loading step (Temp. – Hold time)	2nd Loading step (Temp. – Hold time)
10	300°C – 60 min *elastic creep*	500°C – 5 min *plastic creep*
11	500°C – 5 min *plastic creep*	300°C – 60 min *elastic creep*
12	300°C – 120 min *elastic creep*	500°C – 10 min *plastic creep*
13	500°C – 0 min *plasticity*	500°C – 5 min *plastic creep*
14	500°C – 0 min *plasticity*	500°C – 10 min *plastic creep*

The stress-strain curve and residual axial (ε_{yy}) strain fields for both loading steps of sample 14, as well as the incremental strain field obtained between the 1st and 2nd loading steps are shown in Fig. 5.13. The sample was loaded plastically to 250 MPa at 500°C (*plasticity*), after unloading it was placed under the microscope and a set of images was taken (marked by the letter b in Fig. 5.13). Then, the sample was loaded again to 250 MPa for 10 minutes at 500°C (*plastic creep*), and a second set of deformed images was taken (marked by the letter c). The strain fields shown in Fig. 5.13b and c are the results of correlating these two set of images with the reference image. The strain field shown in Fig. 5.13d is the result of correlating these two sets with each other, which gives us the incremental strain accumulated during the 2nd loading step (elastic creep).

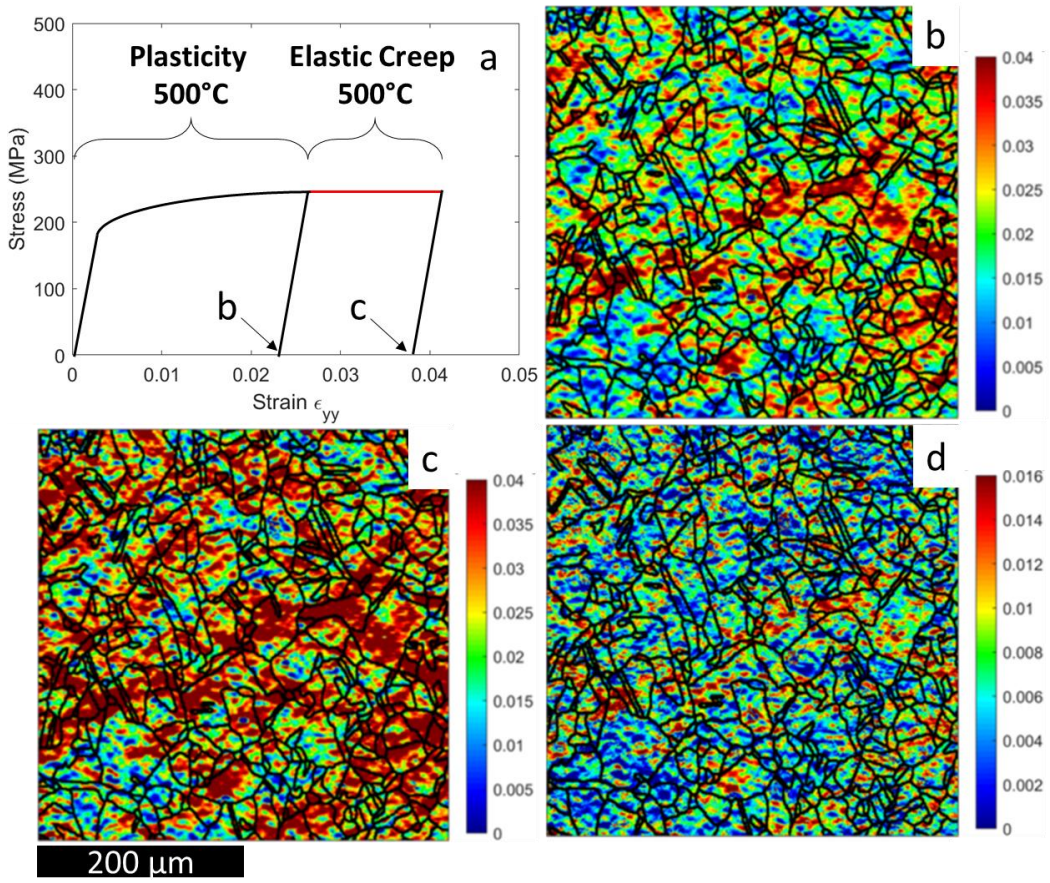

Fig. 5.13. (a) Schematic stress-strain curve for sample 14 at 500°C; (b) Residual axial strain field (ε_{yy}) obtained after 1st loading step; (c) 2nd loading step and (d) The incremental strain field between the 1st and 2nd loading step.

The bar plots for the RVE sizes and average strain ratios of all loading steps of samples 10-14 are shows in Fig. 5.14 and Fig. 5.15, respectively. For reference, the loading parameters of each loading step are found in a table below the *x* axis. For example, the bar labelled 11_2 shows the result obtained for the second loading step of sample 11, which was performed at 300°C with a hold time of 60 minutes, while the bar labelled 13_i shows the result for the increment between the first and second loading steps of sample 13, performed at 500°C for 5 minutes. Overall, the results shown in Fig. 5.14Fig. 5.15 corroborate what was found for samples 1-9, indicating that the geometry of the sample did not influence the RVE size or the normal to shear strain ratio (results for hourglass samples were the same as for dog-bone samples). The RVE sizes and strain

ratios for elastic creep were always considerably lower than those of plasticity or plastic creep. Even when the sample had been subjected to plastic deformation, the incremental strain accumulation from elastic creep resulted in lower RVE sizes and strain ratios, reinforcing even further the observation that plasticity seems to dominate over creep. For every strain field where the two deformation types (plasticity and elastic creep) were present simultaneously (plastic creep), the RVE size and strain ratio mimicked that of pure plasticity.

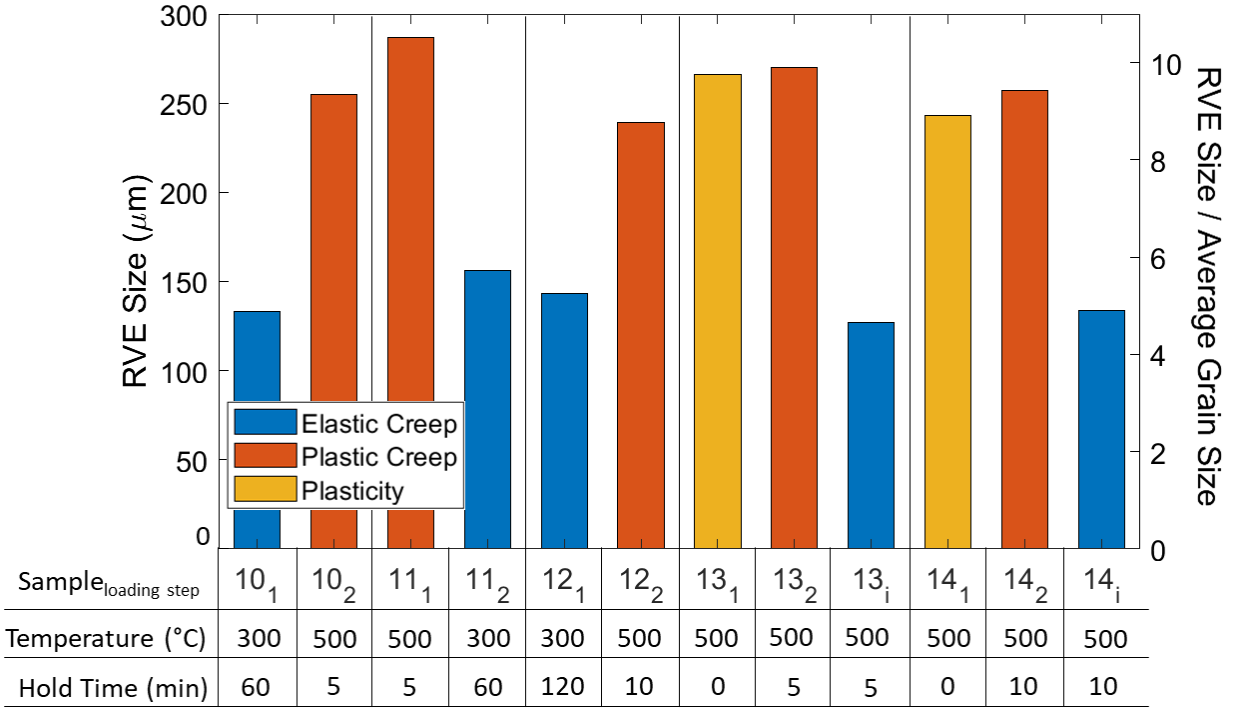

Sample$_{\text{loading step}}$	10_1	10_2	11_1	11_2	12_1	12_2	13_1	13_2	13_i	14_1	14_2	14_i
Temperature (°C)	300	500	500	300	300	500	500	500	500	500	500	500
Hold Time (min)	60	5	5	60	120	10	0	5	5	0	10	10

Fig. 5.14. RVE sizes obtained for all loading steps of samples 10 to 14, colored by deformation type.

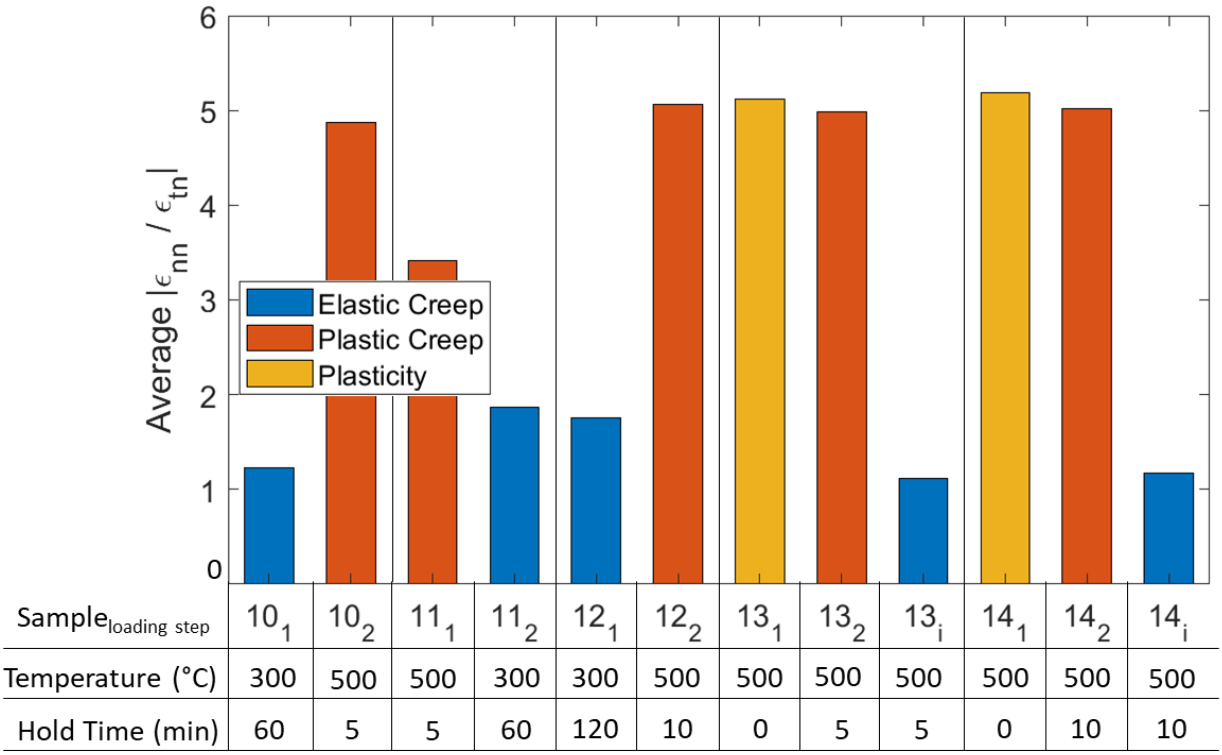

Sample$_{\text{loading step}}$	10_1	10_2	11_1	11_2	12_1	12_2	13_1	13_2	13_i	14_1	14_2	14_i
Temperature (°C)	300	500	500	300	300	500	500	500	500	500	500	500
Hold Time (min)	60	5	5	60	120	10	0	5	5	0	10	10

Fig. 5.15. Average strain ratios obtained for all loading steps of samples 10 to 14, colored by deformation type.

5.5 Summary

This chapter described an experimental study concerning the influence of loading parameters, namely maximum stress, temperature and hold time, on the strain-based RVE sizes obtained from microscale strain measurements. High-resolution DIC residual strain results and EBSD-obtained grain structure data were employed to measure the RVE sizes, using the stereological method proposed in Chapter 4, of a total of fourteen samples tested under a range of different loading parameters. These RVE measurements were made for three different deformation regimes namely *elastic creep*, *plastic creep*, and *plasticity*. Further analysis of the strains at regions near grain boundaries (mantle regions), using a relevant transformation of coordinates, allowed for the comparison between the measured RVE sizes and the nature of strain accumulation. The local

normal to shear strain ratio, which can be related to underlying deformation mechanisms, was shown to have good correlation with the strain-based RVE size for all tested cases.

The RVE sizes (reported as a linear dimension along the side of a 2D box) obtained for samples subjected to elastic creep deformation were considerably lower than those obtained for plasticity and plastic creep (4-6 times the average grain size, compared to 8-10 times for plasticity and plastic creep). Normal to shear strain ratios near grain boundaries were calculated and were shown to have a dependence on temperature, which was expected because creep deformation mechanisms are known to be a function of temperature. The average strain ratio for *elastic creep* was found to be much lower than that of *plasticity* and *plastic creep*, indicating that *elastic creep* presents more predominant grain boundary sliding, while *plasticity* dominates the response whenever it is present. The comparison between the RVE size and strain ratio results leads to the conclusion that the strain-based RVE size may be used as a proxy for determining deformation mechanism transitions. This is corroborated by the specific results for *elastic creep* at higher temperature (800 °C), in agreement with literature findings on the creep mechanisms of the studied alloy.

Overall the findings of the study indicate that a change in loading parameters results in a change in the underlying deformation mechanisms, which in turn have an effect on the inhomogeneity of the microscale strain field. Following this reasoning, if we were able to accurately predict in detail the microscale strain field, we should be able to use the strain-based loading-parameter-dependent RVE size to upscale that prediction, through homogenization, to estimate the macroscale response of the material. The next chapter will go over the use of neural networks to predict the microscale strain field.

Chapter 6: Predicting Microscale Strain Fields through Machine Learning[4]

In the previous chapter it was shown that the size of a representative volume element (RVE) can be dependent on the loading type to which the material is subjected. Such dependence is a very important aspect to consider when using the RVE for its intended goal of homogenizing microscale results to predict macroscale response. However, beyond homogenization to the macroscale, prediction of the detailed microscale response is also desirable for certain aspects of the material's behavior, such as fracture and fatigue failure, which are generally processes driven by local inhomogeneities and thus less amenable to homogenization. In fact, microscale simulation approaches such as crystal plasticity, were initially developed to predict such local effects. Many of these microscale techniques are limited in terms of predicting the response particularly in the vicinity of grain boundaries (in our case we are interested in plastic strain fields developed at the microstructural level). Most commonly in crystal plasticity simulations the grain boundaries are assumed to have perfect continuity (e.g., Özdemir and Yalçinkaya, 2014) or at most simplified responses such as the thermodynamics model of van Beers et al. (2013). In reality however, grain-boundary response can in itself be very complicated making it difficult to accurately include in micro/mesoscale simulations. This chapter, therefore, presents a first step towards the goal of predicting microscale response near grain boundaries starting directly from experimental results, which by their nature will include information of the grain boundary behavior and characteristics. In order to do so, a machine learning algorithm known as a neural network is applied to predict local residual strains near grain boundaries (GBs) of heat-treated stainless steel 709 samples. The

[4] This Chapter is an expanded version of Vieira and Lambros (2021b)

neural-network predictions are compared to experimental results with a high level of overall correlation being achieved. By following this approach, we circumvent the use of highly complex and computation-heavy crystal plasticity simulations. In fact, this approach may be combined with prior approaches, which are better at predicting response in the interior of crystal.

6.1 Background

The term machine learning is widely used as an umbrella label to describe many different algorithms capable of identifying patterns in data. From the very simple linear regression, passing through clustering techniques and going all the way into the more complex neural-network regression, these techniques have in common the relatively large amount of data required to produce reliable predictions (Mitchell, 1997). The following sections describe the use of a fitting neural network algorithm to recognize patterns in the large amount of residual strain data points obtained from *ex situ* DIC results. Gurney defines a neural network as an interconnected assembly of simple processing units (nodes) capable of storing values for internodal connection strengths (weights and biases) that are obtained from a process of adaption (learning) to a set of training data (Gurney, 1997). Even though the use of computers to simulate learning networks is not a new idea – it was proposed as early as 1943 (McCulloch and Pitts, 1943) – recent years have seen a more widespread application of these techniques.

In the field of solid mechanics, neural networks have seen increased adoption over the past two decades. Sourmail et al. (2002) used neural networks to predict the creep strength of austenitic stainless steels using their compositions and loading parameters as inputs. Lee et al. (2005) applied neural networks to predict crack growth rate and residual fatigue life of Al 2024-T3 samples, using the stress range as the only input. Kang et al. (2006) used a neural network combined with finite elements simulations to predict critical locations for fatigue damage in automotive frames. Li et

al. (2012) compared macroscale flow stress predictions from a neural-network model (with strain, strain rate and temperature as inputs) to a modified Zerilli-Armstrong and Arrhenius-type model, emphasizing the need of extensive data in machine learning applications. Pujol and Pinto (2011) and more recently Martinez and Ponce (2019) used neural networks to predict loading sequence effects on fatigue, studying the effects of overloads and underloads on fatigue life. Mozaffar et al. (2019) successfully modeled path-dependent plasticity using neural networks trained using simulation results, predicting the stress-strain behavior during complex phenomena (distortional hardening) within 0.5% error. Lin et al. (2008) trained a neural network to model the flow stress of a low alloy steel based on experimentally observable quantities. Jones et al. (2018) applied neural networks to infer plastic flow rules using data from representative simulations. They also present a very good review on the use of neural networks in the broader field of solid mechanics. Even more recently, Abueidda et al. (2021) showed that a temporal convolutional network (a specific type of neural network) could produce accurate and fast predictions for materials' response to history-dependent phenomena such as plasticity and thermo-viscoplasticity.

As seen from the brief literature review above, most applications of neural networks to the field of solid mechanics to date have had as their objective either the modelling of macroscopic behavior (i.e., mechanical properties or constitutive response of the material) or failure predictions under a variety of loading conditions. Although these are certainly of interest, the study presented in this chapter concerns the use of neural networks to predict the microscale response of the material (distribution of strain accumulations at the microscale). The objective here is to produce accurate predictions for the accumulation of plastic residual strains near grain boundaries at the microstructural level during plastic (room temperature creep) deformation.

6.2 Large-Grain Samples through Thermal Grain Growth

The as-received stainless steel 709 alloy used for the experiments shown in the previous chapters had an average grain size of 25-30 μm. As was shown earlier, this grain size resulted in *ex situ* residual strain measurements with about 5 to 6 subsets along the average grain size (linear dimension). At that magnification a large number of grains (around 500) could fit within the region of interest, enough to guarantee that the observed portion of the material would reflect its macroscopic behavior. This was necessary when studying RVE sizes for different loading parameters, because it means that the region of interest was always larger than the size of the RVE.

However, in this chapter, the study of the residual strains accumulated near grain boundaries requires a higher grain to subset size ratio, since the length scales of the subset size and the region around the GB where the material response is primarily governed by the interaction with the boundary (introduced in Chapter 5 as the "mantle" of each grain) must be comparable. One approach would be to use an even higher magnification level than before (Chapters 3, 4 and 5) when taking the DIC images. However, this would introduce a series of complications to the experimental methodology, including the difficulty of producing adequate DIC speckle patterns at these smaller length scales and concerns about the depth of field and surface roughness effects of the plastically deforming sample at higher magnifications, which would make focusing harder or even impossible in some cases (higher plastic strain levels). Therefore, an alternative approach was adopted here in which we grow the grains of 709 (via a heat treatment) so as to increase the grain to subset size ratio when applying HiDIC. To this end, a grain-growth study was conducted to decide which temperatures and treatment time should be applied to the material in order to achieve the desirable grain to subset size ratio (Appendix C describes in detail the study of grain growth for alloy 709.) Fig. 6.1 shows the resulting grain size evolution with time from the selected

heat treatment at 1200°C. The average grain size of the heat-treated samples was within the range 160-190 μm, which meant an increase of the grain to subset size ratio to about 32 (number of subsets that can fit along the linear-dimension average grain size).

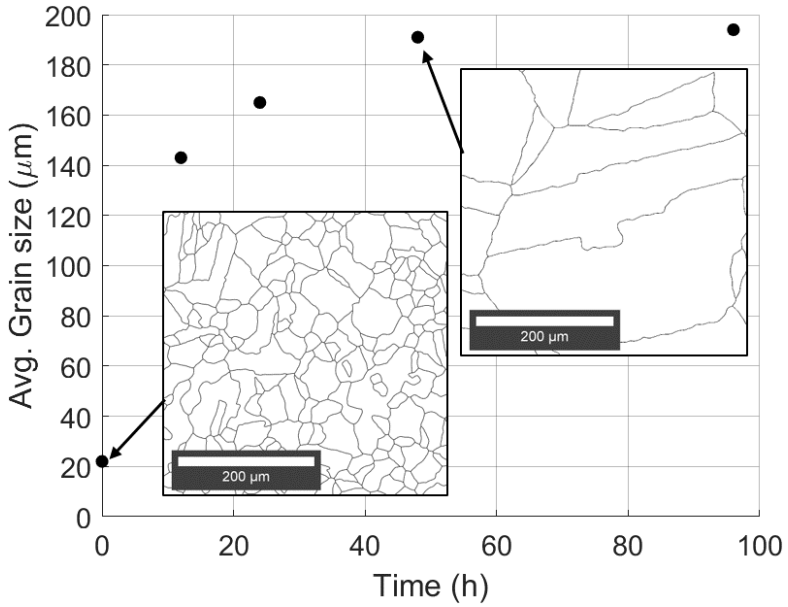

Fig. 6.1. Average grain size vs. heat treatment time plot for alloy 709 at 1200 °C.

6.3 HiDIC Results for Heat-Treated Samples

Heat-treated hourglass samples were polished, EBSD-scanned, etched and had DIC patterns applied to them, as described in Chapter 3. Then each one was loaded to 250 MPa and held at maximum load for 1 hour. Since alloy 709 presents creep straining even at room temperature, the use of such hold times was deemed necessary in order to compare the levels of accumulated plastic strains between samples. Fig. 6.2 shows a contour plot for the residual axial (ε_{yy}) strains for one of the samples, after the tensile/hold loading, overlaid on the grain boundaries obtained from EBSD.

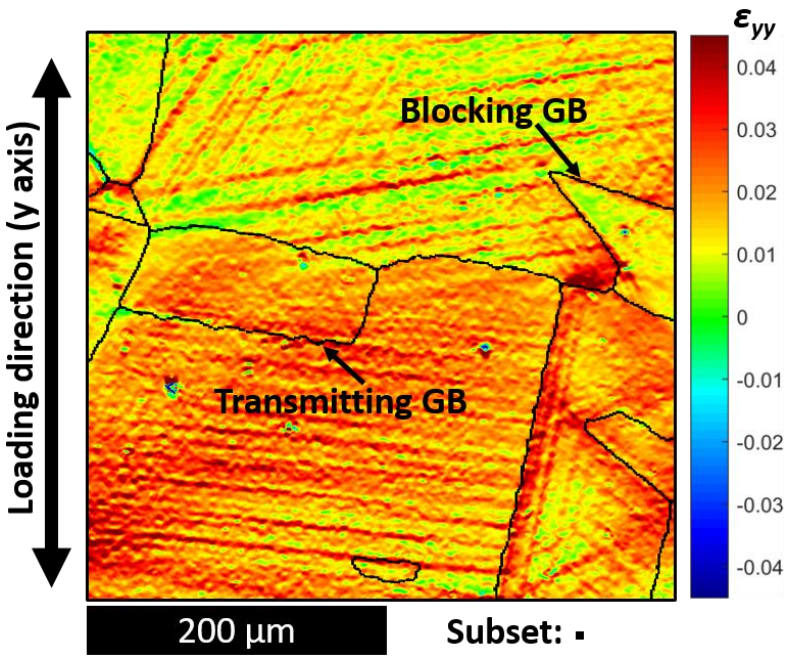

Fig. 6.2. Residual axial (ε_{yy}) strains obtained after plastic deformation at 250MPa and 1 hour hold time.

With the increased grain to subset size ratio, it is much easier to observe how the strains interact with the microstructure. The parallel lines of higher residual strain levels show the active slip systems in each of the grains, and the way they interact with the grain boundaries can be used to classify those boundaries as blocking or transmitting boundaries, as shown. (A blocking boundary doesn't allow slip across the two adjacent grains presenting very different stain fields on each side, while a transmitting boundary presents similar strain fields on each side). Fig. 6.2 also presents evidence for the existence of preferential locations for strain accumulation, which have been shown to serve as precursors for micro-crack nucleation under cyclic loading conditions (Abuzaid et al., 2012). Finally, in agreement with previous observations from Abuzaid et al. (2013), these strain "hot-spots" appear largely at the vicinity of grain boundaries. Thus, the next sections will go over the analysis, and eventual prediction, of the strains accumulated during a single tensile half-cycle (uniaxial tensile test with 1 hour hold time at maximum stress) at the mantle region surrounding grain boundaries.

6.4 Local Coordinate GB Mantle Strains

In order to better understand the effects of loading and strain accumulation near grain boundaries, the DIC-measured residual strains within the mantle regions of each of the three samples were rotated to local GB-coordinates (normal, tangential), following the same procedure discussed in Section 5.3. Fig. 6.3, Fig. 6.4 and Fig. 6.5 show the mantle residual strains measured for each of three samples, both in the global (x,y) and local (n,t) coordinates. As pointed out earlier, this coordinate transformation allows us to better visualize the behavior of the material near a boundary, i.e., whether the adjacent grains are being sheared, pulled apart or compressed together.

As before (Section 5.3), the mantle sizes used in this chapter were estimated following a percentage of the average grain size similar to what was observed by Abuzaid et al. (2012) for a nickel superalloy. With the large-grain samples, a very small number of grains can fit inside the field of view, which resulted in different estimates for mantle size, with values of ~15 μm, ~10 μm and ~12 μm from samples 1, 2 and 3 respectively. The most conservative estimate of 10 μm was chosen for uniformity, and was used in all the following results. This meant that for all boundaries of all 3 samples, about 2 subsets could fit within the mantle, ensuring that real strain data (not interpolated data) are being measured inside the mantles. Fig. 6.6 shows a magnified view of the dashed squares shown in Fig. 6.4 with a subset drawn next to the mantle. Nonetheless, the low number of subsets that can fit across the mantle width does not really allow for measurements of variations across the mantle, meaning that the contour details shown across mantles in Fig. 6.6 are likely form the plotting interpolations. However, data along (parallel) to the grain boundary are considered more reliable and for this reason the following analysis considers the mantle as a unidimensional entity, with strains being measured and predicted along its length, but not across its thickness.

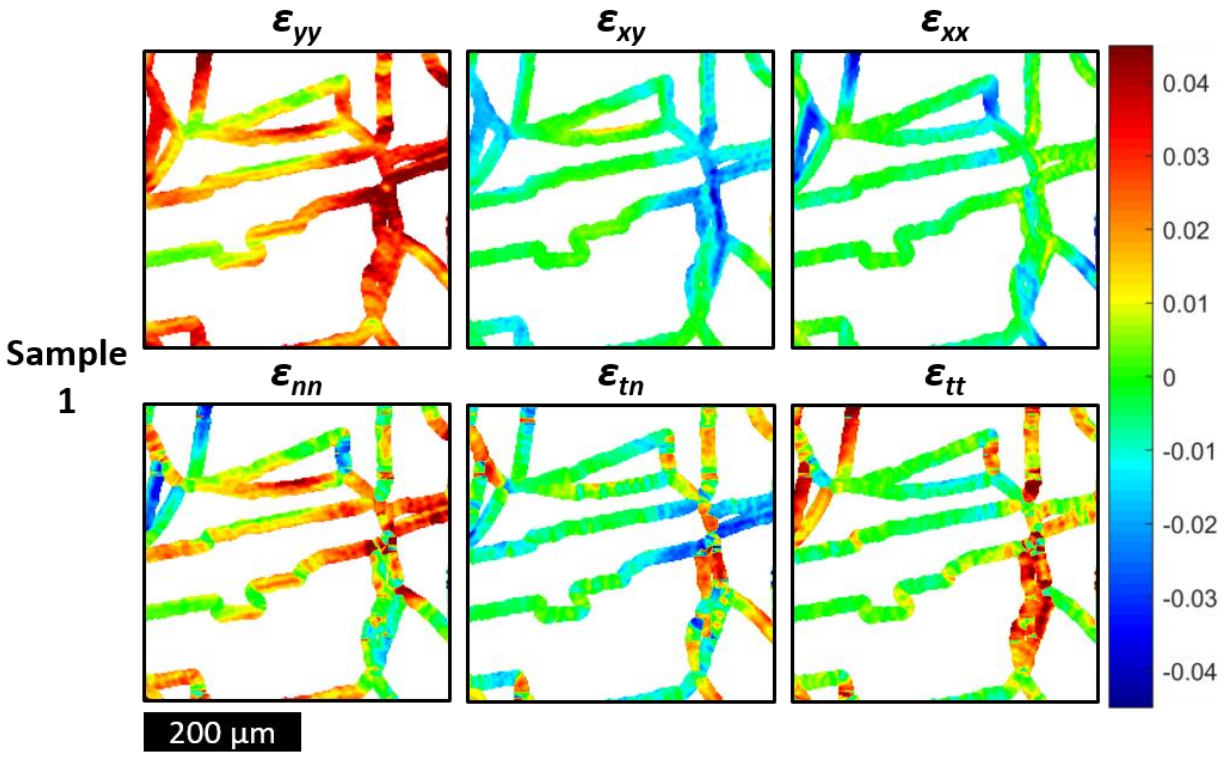

Fig. 6.3. Mantle residual strains in the global (*x*,*y*) and local (*n*,*t*) coordinates for sample 1.

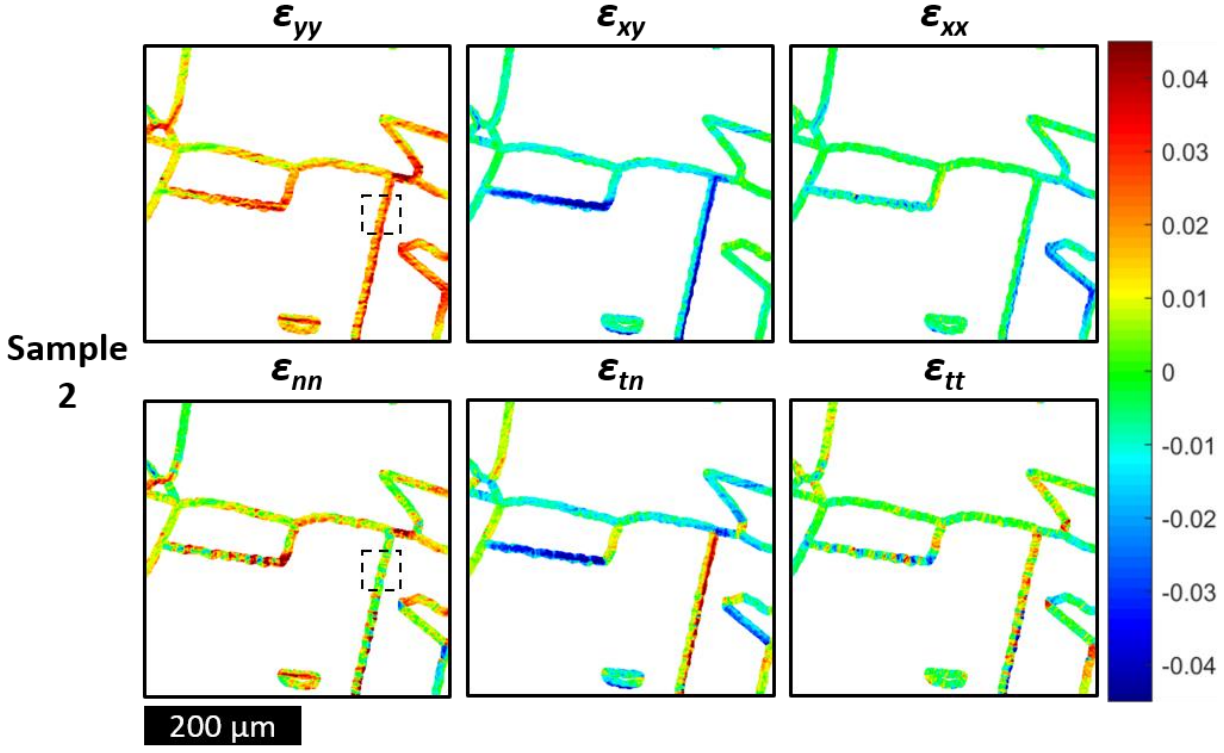

Fig. 6.4. Mantle residual strains in the global (*x*,*y*) and local (*n*,*t*) coordinates for sample 2.

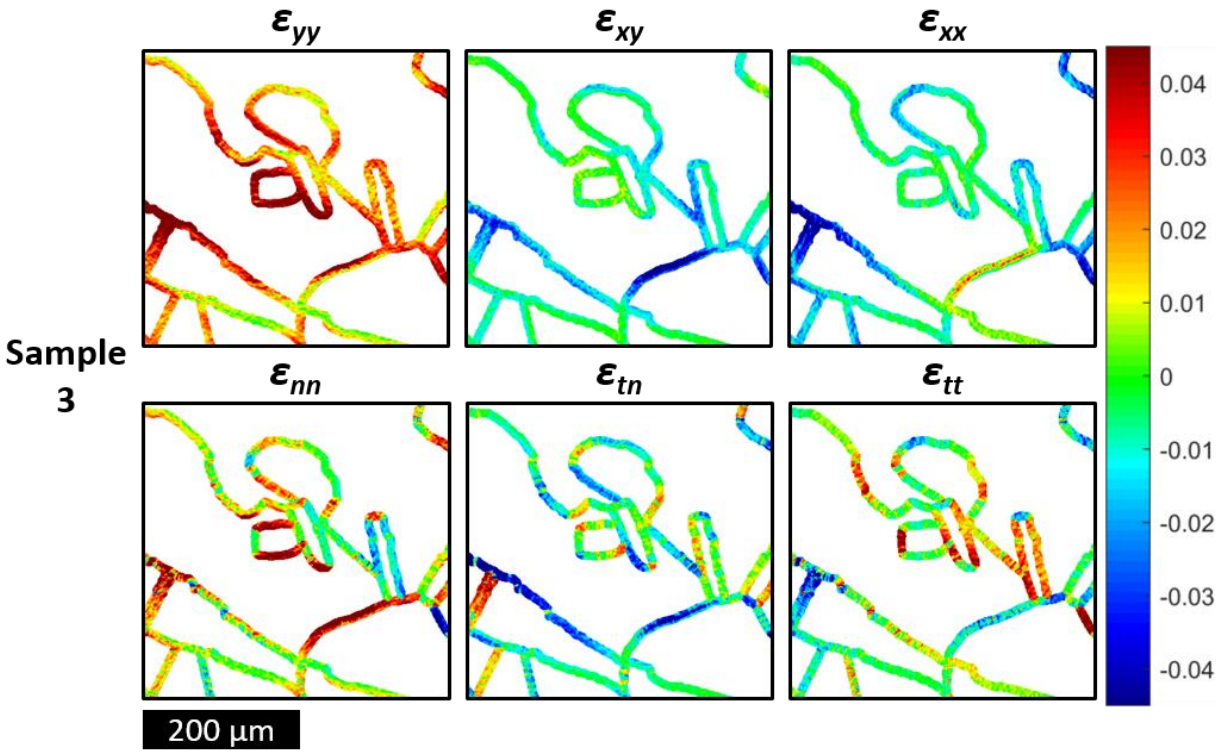

Fig. 6.5. Mantle residual strains in the global (*x*,*y*) and local (*n*,*t*) coordinates for sample 3.

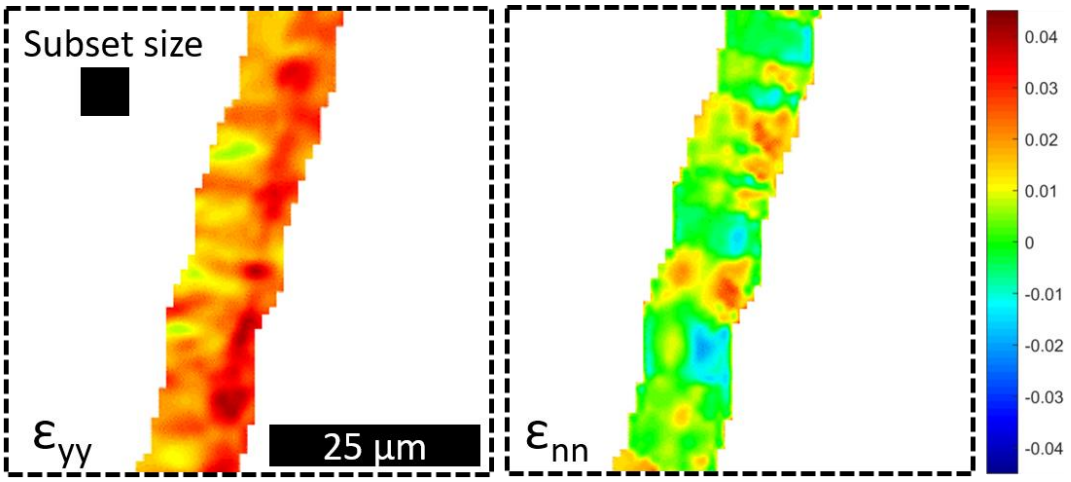

Fig. 6.6. Magnified view of the dashed squares shown in Fig. 6.4.

6.5 Clustering of Local Normal and Shear Strains

The first step in proposing a neural network approach for predicting the microscale strain accumulation inside the mantle regions is to determine what variables could be used as input for the prediction. In essence, we need to identify which parameters control the accumulation of strain

inside the mantle, and the degree to which they control the strain (since the strain dependence may be stronger on some parameters more than others). Candidate input variables are the loading conditions (it is evident that parameters such as maximum stress, temperature, and hold time have an effect on the accumulation of residual strains), but for simplicity all samples considered in this study were loaded under nominally identical conditions, essentially isolating the loading parameters. (A future study could be done that extends the current approach to variable loading parameters as well.) Other parameters that might have an effect on strain accumulation are related to the microstructure of the material. Both Abuzaid et al. (2016) and Rotella and Sangid (2020) have reported that the formation of grain clusters (neighboring grains with high strain levels) influences the accumulation of strains in grains adjacent to the cluster. Carter et al. (2012) measured the influence of triple points in the accumulation of strains near grain boundaries, reporting a statistical correlation between triple points and higher strain levels. Cheong and Busso (2006) found through crystal plasticity simulations that both high and low misorientation boundaries play a role in the heterogeneity of strain distributions at the grain scale. Later, Sangid et al. (2011) conducted molecular dynamics simulations indicating that boundaries with higher misorientation angles (twin boundaries) in general act as barriers to slip transmission, creating hot-spots for strain accumulation. A differing result was reported by Carter (2012) where they experimentally measured *in situ* strains during deformation of a nickel superalloy and found that misorientation angle had a low correlation with the localization of strains, pointing that misorientation alone would not be enough to predict strain hot-spots. Carter (2012) also reported significant statistical correlation between grain boundary inclination angle and the level of strain accumulation near grain boundaries.

Here, two of these variables (GB misorientation angle and GB inclination angle) were considered, and a clustering study was conducted through scatter plots to determine their correlation with the measured local residual mantle strains. Fig. 6.7 shows a scatter plot of ε_{tn} vs. ε_{nn} colored by the misorientation angle of each mantle point HiDIC measurement of sample 1. There is no clear pattern emerging from this plot, indicating that the correlation between misorientation angle and the residual strain levels measured in this sample is weak. Samples 2 and 3 showed similar results, in agreement with what had been reported by Carter (2012).

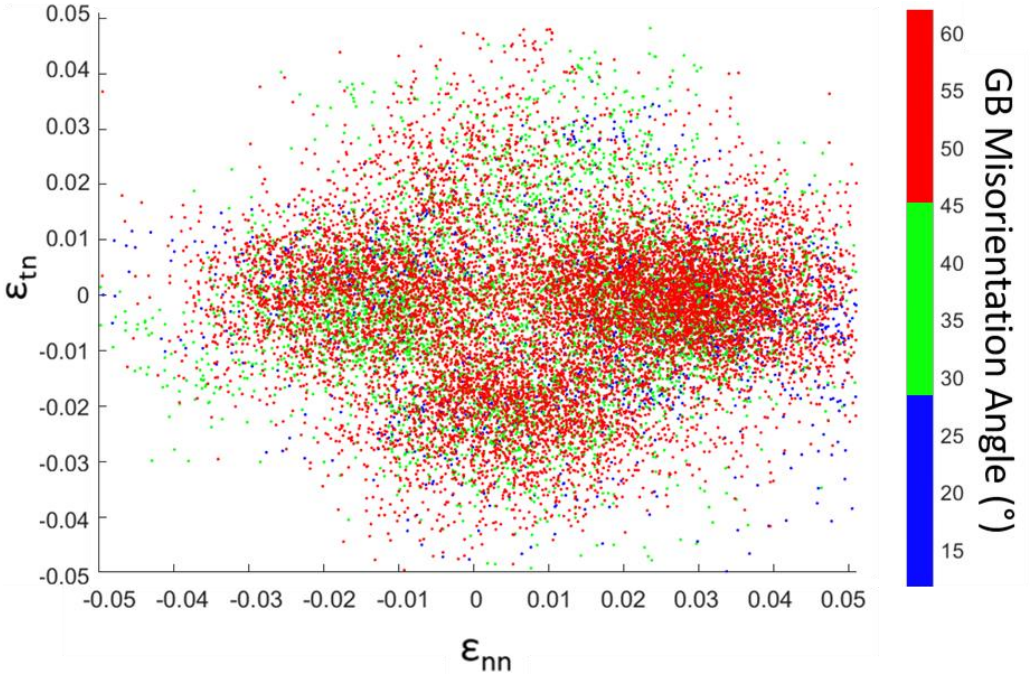

Fig. 6.7. Residual shear vs. normal strains (in GB coordinates) for every mantle point of sample 1; each dot represents one mantle point and is colored by its corresponding misorientation angle.

The second variable considered was the GB inclination angle, defined as the complementary geometric angle between the local grain boundary and the vertical loading axis (or the angle between the GB and the horizontal). The plots shown in Fig. 5.11 (for as-received samples) already indicated that there is a possible relation between the strain levels at the mantle and the GB inclination. The results obtained below also corroborate what was measured earlier:

Fig. 6.8 shows a scatter plot of ε_{tn} vs. ε_{nn} colored by the GB inclination angle of each mantle point of sample 1. Note that exactly the same set of strain measurement data points are shown in the plots of Fig. 6.7 and Fig. 6.8. Each mantle point was colored according to the GB inclination of its corresponding grain boundary, following the thresholds shown in the legend. It is clear that low-GB-inclination boundaries (boundaries perpendicular to the loading axis) present relatively high tensile normal strains and relatively low shear strains, while high-GB-inclination boundaries (parallel to loading axis) produce relatively high compressive normal strains and relatively low shear strains. Slanted boundaries (around 45° angle with loading axis) presented relatively high shear strains with low normal strains. This is a very intuitive result, which can be understood as a GB-based quasi Schmid factor with horizontal boundaries mostly being pulled apart during loading, vertical boundaries mostly being compressed together and slanted boundaries attempting to slide to accommodate straining.

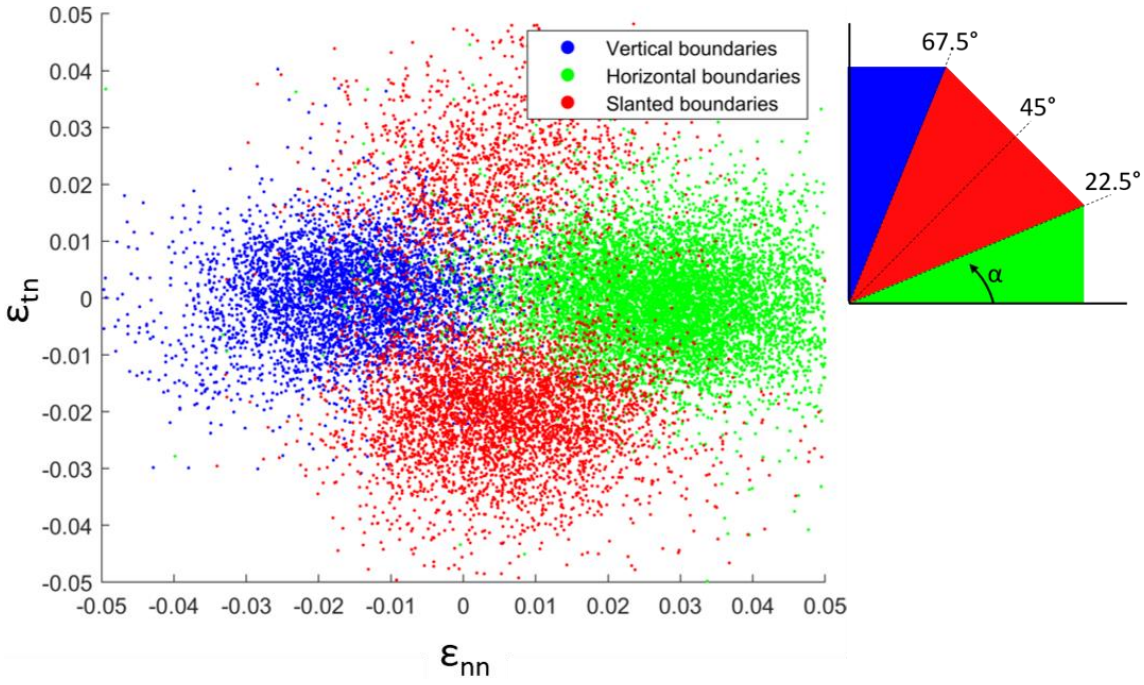

Fig. 6.8. Residual shear vs. normal strains (in GB coordinates) for every mantle point of sample 1; each dot represents one mantle point and is colored by its corresponding GB inclination (α).

Based on the stronger correlation exhibited in Fig. 6.8 than Fig. 6.7, the choice of the GB inclination seemed like the best starting point for as a sole input parameter training of a neural network to recognize the patterns present in each sample, since they all had the same nominal material and loading parameters. At this stage, including an input variable with lower correlation (such as the misorientation angle) would make convergence of the training procedure harder. Gurney (1997) recommends separating high and low correlation input parameters when designing a neural network. Thus, the next section covers the architecture of a single-input fitting neural network and how it is built and trained to predict mantle strains from GB inclination. However, this does not imply that GB inclination angle is expected to be able to predict every local mantle strain value or that other parameters have no influence on local response. It is a starting point that is to be investigated for this large-grain sample as a first step with a plan to expand to additional inputs if this high-correlation input prediction succeeds.

6.6 Single-Input Fitting Neural Network

Here a single-input fitting neural network will be trained to make predictions on the local mantle strain levels based on the GB inclination angle as a predictor. As mentioned above, a neural network consists as a series of simple processing units (neurons or nodes) that have values (weights and biases) associated to them, which are multiplied and added to the input to create an output. Each node can be understood as a line graph that takes an input, multiplies it by a weight and adds a bias to the result to obtain an output. Fig. 6.9a shows a sketch of the structure of the fitting neural network used to predict the mantle strains in the GB coordinate frame. It consists of a double layered neural network, each layer containing 20 nodes, with a single input (the GB inclination angle, α) and three outputs (strain components). During the process of feeding an input through the network to obtain a guess for the outputs (called ‘forward propagation’), each node’s value

(identified as N_{ij}, where i is the layer number and j the node number within the layer) is obtained by adding the summation of all previous connected nodes multiplied by their associated weights and added to a bias value, with the first layer normalized with a sigmoidal function as shown in Fig. 6.9b.

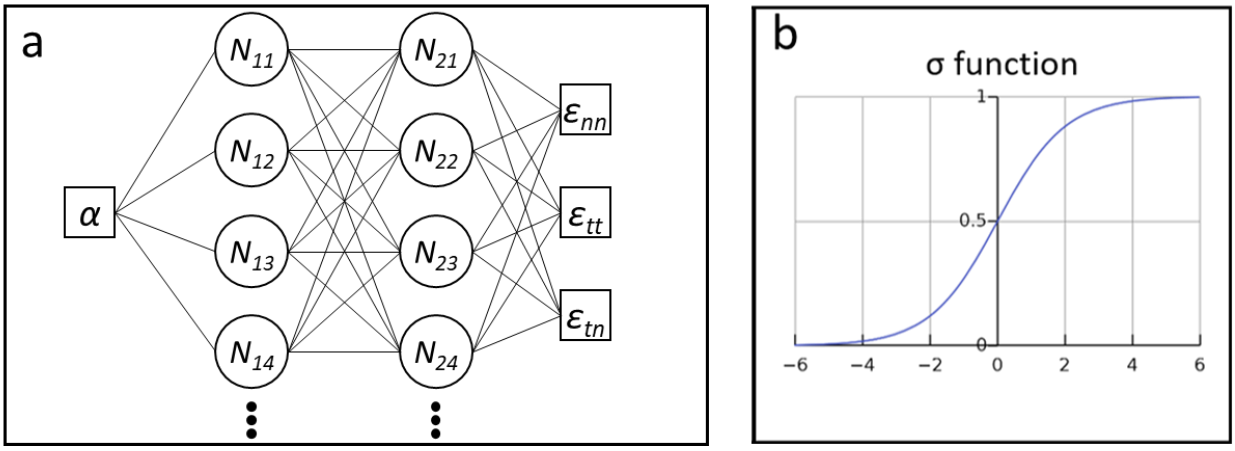

Fig. 6.9. (a) Sketch of the structure of the fitting neural network (nodes are identified as N_{ij} where i is the layer number and j the node number within the layer); (b) Sigmoidal function used to scale the results of the first layer.

The process of training the neural network consists of adjusting the values of these weights and biases so that the neural network produces outputs that are as close as possible to real values contained in the training data. This minimization procedure starts with each weight and bias for all nodes being initialized at random values. Then, a series of input values, for which the outputs (targets) are known, are supplied to the neural network and forward propagated to produce guesses for the outputs. The error between the guessed outputs and the target values is calculated as the mean squared error (performance parameter). Finally, the iterative procedure of adjusting the values of the weights and biases follows a quasi-newton method (Marquardt, 1963), which is implemented in the machine-learning toolbox of Matlab (MathWorks, 2020). For each case studied, the experimental data was randomly divided into 3 subsets, with training data (70% of the experimental results) being presented to the neural network during each minimization iteration,

validation data (15%) being used to check for improvement of the performance parameter after each iteration and test data (15%) being used to check for generality after training is complete (no effect on training). Training was stopped after a gradient below 10^{-7} was obtained for the performance parameter for the validation data or after 6 consecutive iterations without improvement in the performance parameter. Table 6.1 shows all the training parameter used for all neural networks discussed in the following sections.

Table 6.1. Neural network training parameters.

Parameter	Specification
No. of inputs	1
No. of hidden layers	2
No. of neurons in each hidden layer	20
No. of outputs	3
Training data	N1 = 70% of experimental data
Validation data	N2 = 15% of experimental data
Test data	N3 = 15% of experimental data
Training function	Levenberg-Marquardt (*trainml* from Matlab machine-learning toolbox)
Performance function	Mean squared error over validation data $\sum_{N2}(output-target)^2 / N2$
Neuron normalization function	Hyperbolic tangent sigmoid (*tansig* from Matlab machine-learning toolbox)
Minimum performance gradient	1.0×10^{-7}
Maximum validation failures	6

This neural-network design allows each mantle point of the sample to be used as a data point, and thus a single sample can produce a large quantity of training data (around 30,000 mantle correlation points per sample). Different combinations of the experimental data were used to train various neural networks, with the next sections going over the resulting predictions.

6.7 Neural-Network Predictions

6.7.1 From a Single Sample

The initial results presented here start from a case where only one sample might be available for study, in which case data from one half of the sample area (say the left side) might be used as training data for a neural network that is posteriorly used to predict the entire strain field. In addition to its usefulness when limited experimentation might be feasible, this initial approach of using only one sample serves as a proof of concept for the method, since using the data from a single sample will eliminate possible variations from one sample to another. The top row of Fig. 6.10 shows the measured residual strains in the local grain boundary (n,t) coordinates for the mantle regions of sample 1. The right half of the contours is greyed out to indicate that only the left half of the data was used as input for the training of the neural network. The results of the now-trained neural network are shown in the bottom row of Fig. 6.10. The predictions are made over the entire sample area, including the left side that was used for training, and show generally good agreement with the measured strains, with the left half presenting better agreement than the right half. Although what appear as 2D contours are useful for visualization, as stated earlier (Section 6.4), we are going to treat the mantles as unidimensional entities, and because of this the contours for the predicted strains shown no variation across the mantle. Therefore, a better quantitative comparison of predictions and measurements can be made using line plots along specific boundaries. Fig. 6.11 shows the grain boundaries of sample 1 with color coded arrows for four different directions along which line plots of the measured and predicted local shear strain component are presented (points to the left of the vertical dashed line were used in the training procedure). The four boundaries chosen all reside in the right-hand side of the area of sample 1 and therefore were not used as part of the training data. To the extent that the individual sample

allows, one boundary was chosen to be approximately horizontal (number 1), one boundary approximately at 45° (number 2) and two boundaries approximately vertical (numbers 3 and 4), i.e., the latter were aligned with the loading axis. The predictions for all four boundaries show, on average, good agreement with the measured strains. The neural network was not able to predict large variations of average strain along the boundaries, as is clear from the line plots for boundaries 3 and 4, where the predicted strain was a constant value while the measured average strain varied. Another interesting observation is that the neural network was able to predict local strain peaks and valleys along boundary 1.

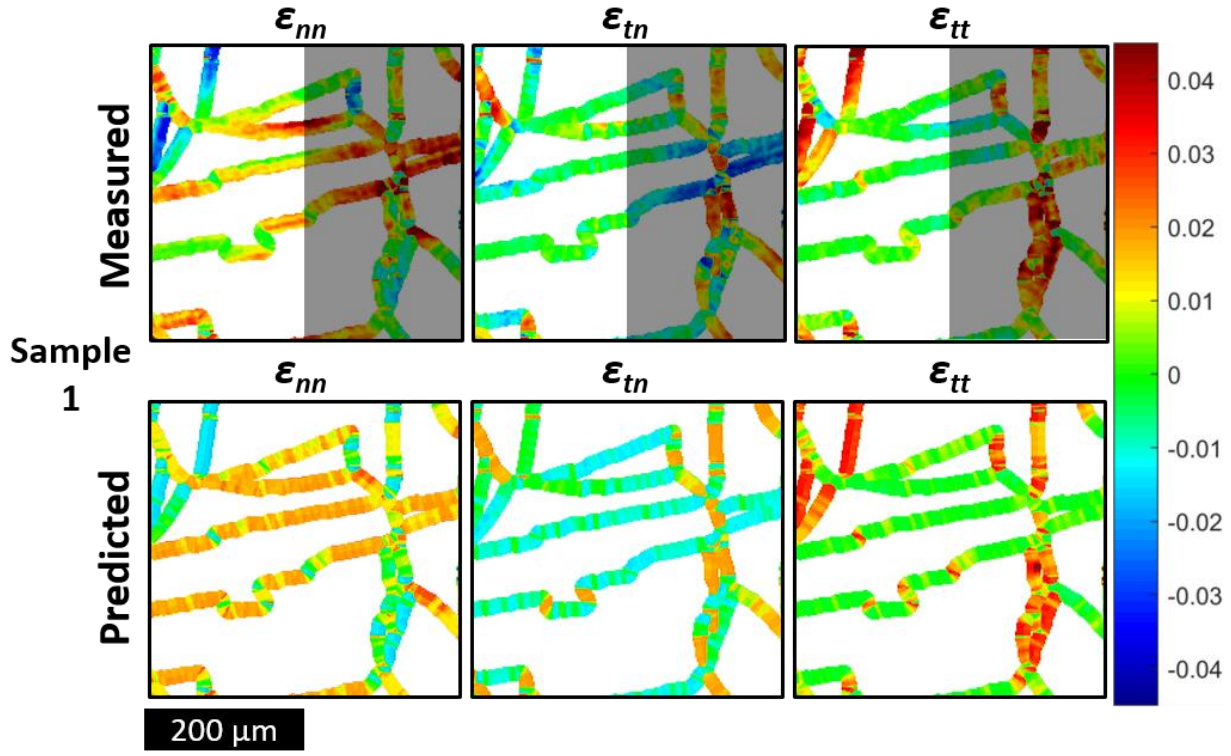

Fig. 6.10. Measured and Predicted grain-boundary coordinate residual strains at mantle regions for sample 1 (neural network trained on left half of sample 1).

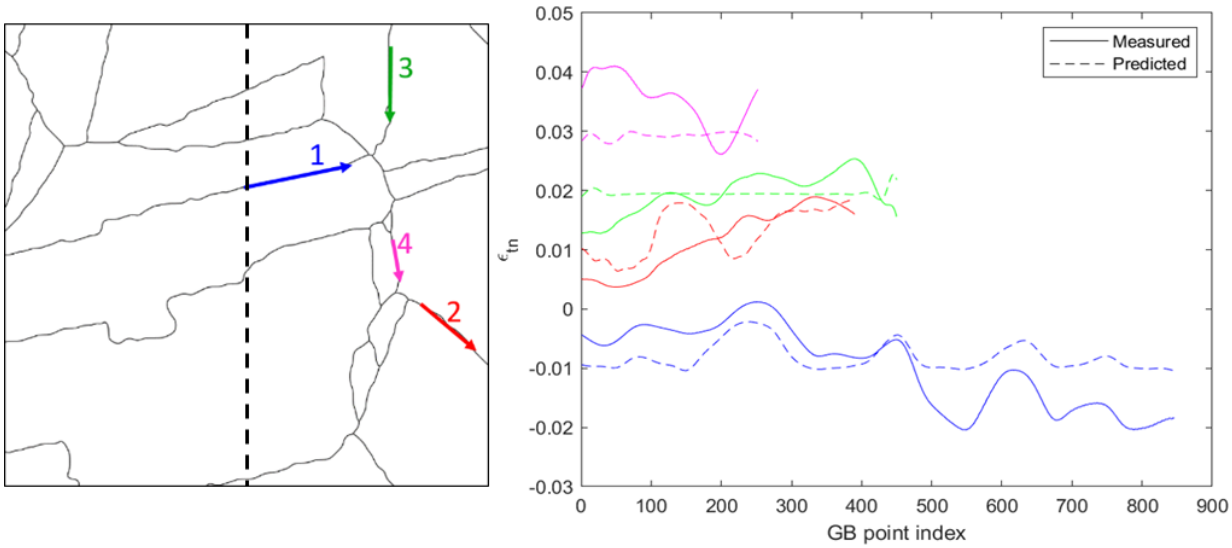

Fig. 6.11. Grain boundaries and color-coded arrows of 4 boundaries from sample 1 (points to the left of the vertical dashed line were used in the training procedure) and line plots showing measured and predicted values for the shear strains of each boundary.

It is clear from both ways of visualizing the predictions (Fig. 6.10Fig. 6.11) that the neural network is capable of predicting average strain levels in the mantle regions. Although this result is quite promising, in order to evaluate the robustness of the approach when predicting strain fields, some validation tests were performed, to verify the predictions from the neural network.

6.7.2 Validation Tests

The first of these validation tests consisted of passing random values as inputs (GB inclination) for the neural network, which resulted in a non-converging trainment procedure, making it clear that the predictions were not a product of the design of the network by itself, but actually results from the correlation between the input (GB inclination) and the targets (strain components). The second validation test consisted of attempting to use the same neural network design to predict the strains in the core region of the grains, which again resulted in a non-converging trainment, indicating that the grain boundary inclination angle is not a good predictor for core strains, as was expected. Again, this second test made it clear that the underlying

correlation between GB inclination and mantle strains is what makes the predictions possible. The final validation test consisted of using the neural network trained on mantle data to predict core strains resulting in very low correlations between predicted and measured core strains, as expected. These three validation tests made it clear that the predictions of mantle strains from the GB inclination were not a coincidence, but an actual result of the underlying correlation between the two variables (GB inclination and strains). The inclusion of more input parameters that present good correlation with core strain accumulation is part of the proposed future work presented in Chapter 7.

6.7.3 From Multiple Samples

Additional neural networks were trained using four different combinations of training data sets based on data from three samples. One neural network each was trained using the totality of the mantle points in each of the three samples considered here, resulting in three different neural networks. The fourth network was trained using the left third of the mantle points from all of the samples *combined*. (When training combined data from all three samples, we used 1/3 of the data points in each sample in order to keep the number of training data points the same in all 4 neural network cases). Each of these four differently trained neural networks can predict the strains for each of the 3 samples, allowing us to analyze how well each neural network performs under training conditions that are now also influenced by sample variability. The top and bottom rows of Fig. 6.12, Fig. 6.13 and Fig. 6.14 show mantle local contour plots for the measured and predicted (by the combined neural network) residual strain fields for samples 1, 2 and 3 respectively.

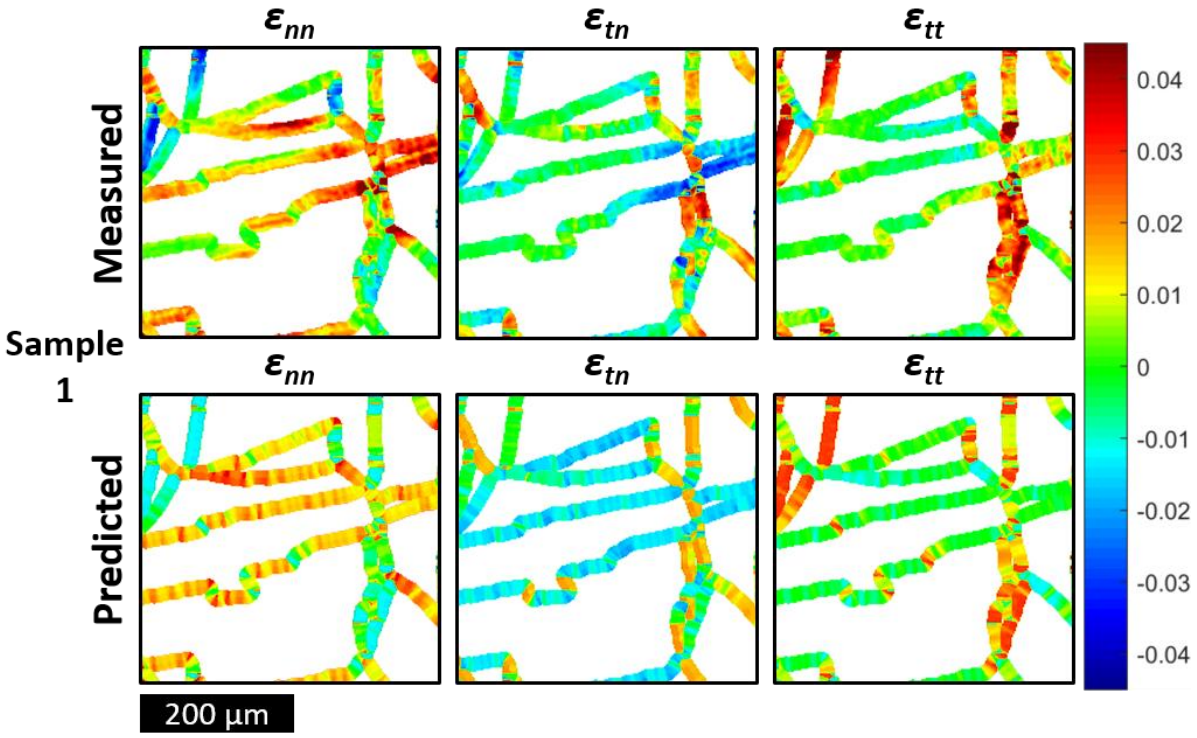

Fig. 6.12 Measured and Predicted grain-boundary coordinate residual strains at mantle regions for sample 1 (neural network trained on combined data from left third of all samples).

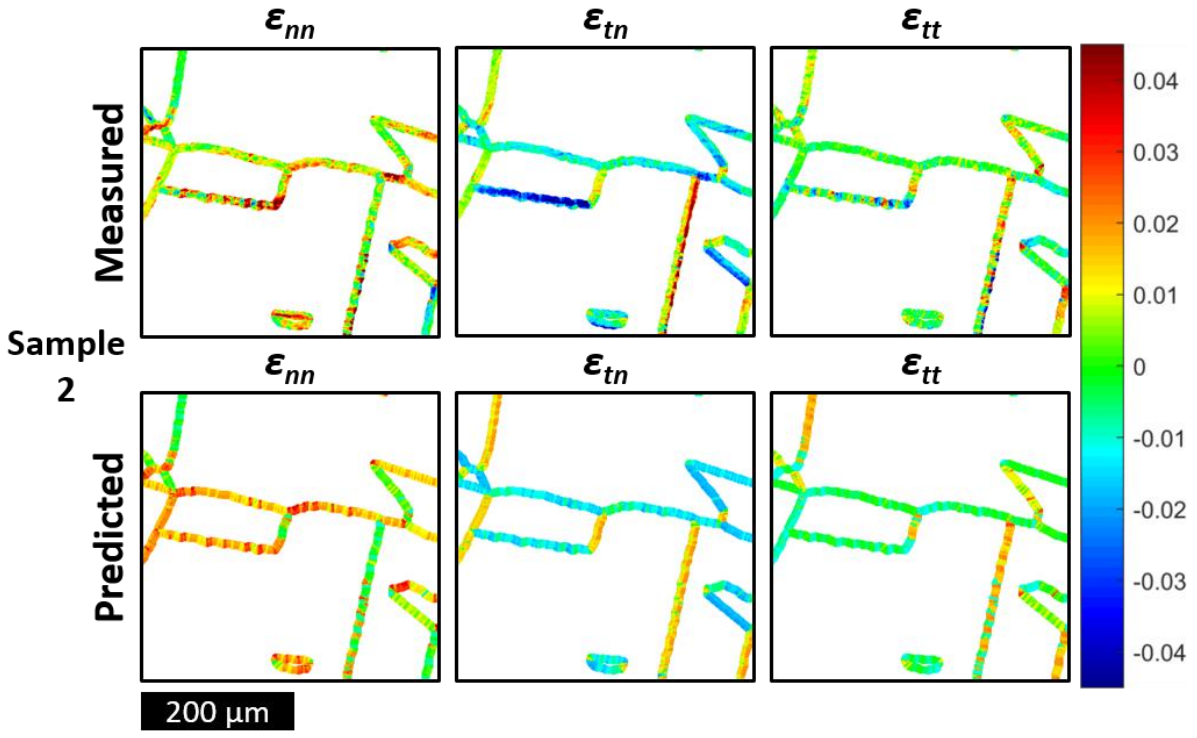

Fig. 6.13 Measured and Predicted grain-boundary coordinate residual strains at mantle regions for sample 2 (neural network trained on combined data from left third of all samples).

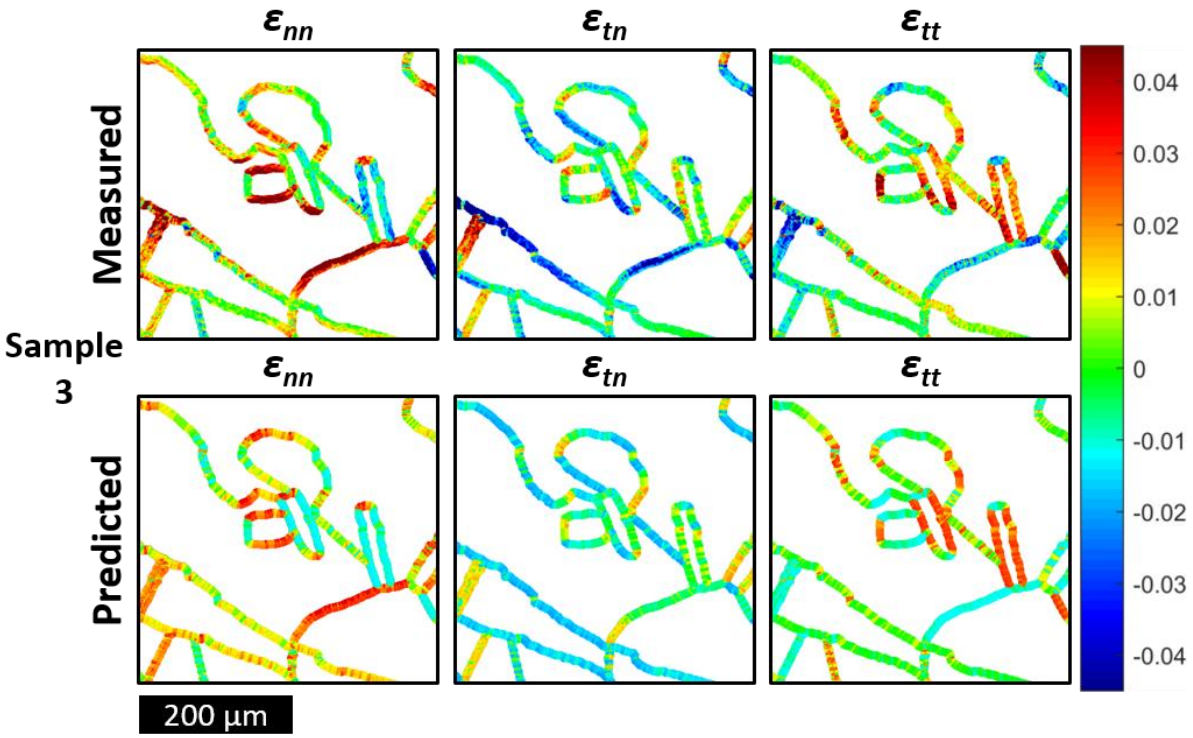

Fig. 6.14 Measured and Predicted grain-boundary coordinate residual strains at mantle regions for sample 3 (neural network trained on combined data from left third of all samples).

These contours show the potential of the neural networks, with a high visual correlation between the measured and predicted residual strains. Being trained on data from all 3 samples, the combined neural network proved to be the best overall in predicting the strains. For almost all boundaries, the best network was the one trained on data from the same sample, with the combined network being the close second, which is why it ends up as the best overall. This result is very intuitive, since the data from each sample should have particularities that are not accounted for by the neural network, such as small variations in loading conditions, specimen geometry and microstructural features (since the samples were taken from different regions of the as-received material and heat treated separately). Fig. 6.15, Fig. 6.16 and Fig. 6.17 show line plots of the results from all 4 neural networks, along with the measured results, for 3 boundaries in each of samples 1, 2 and 3 respectively.

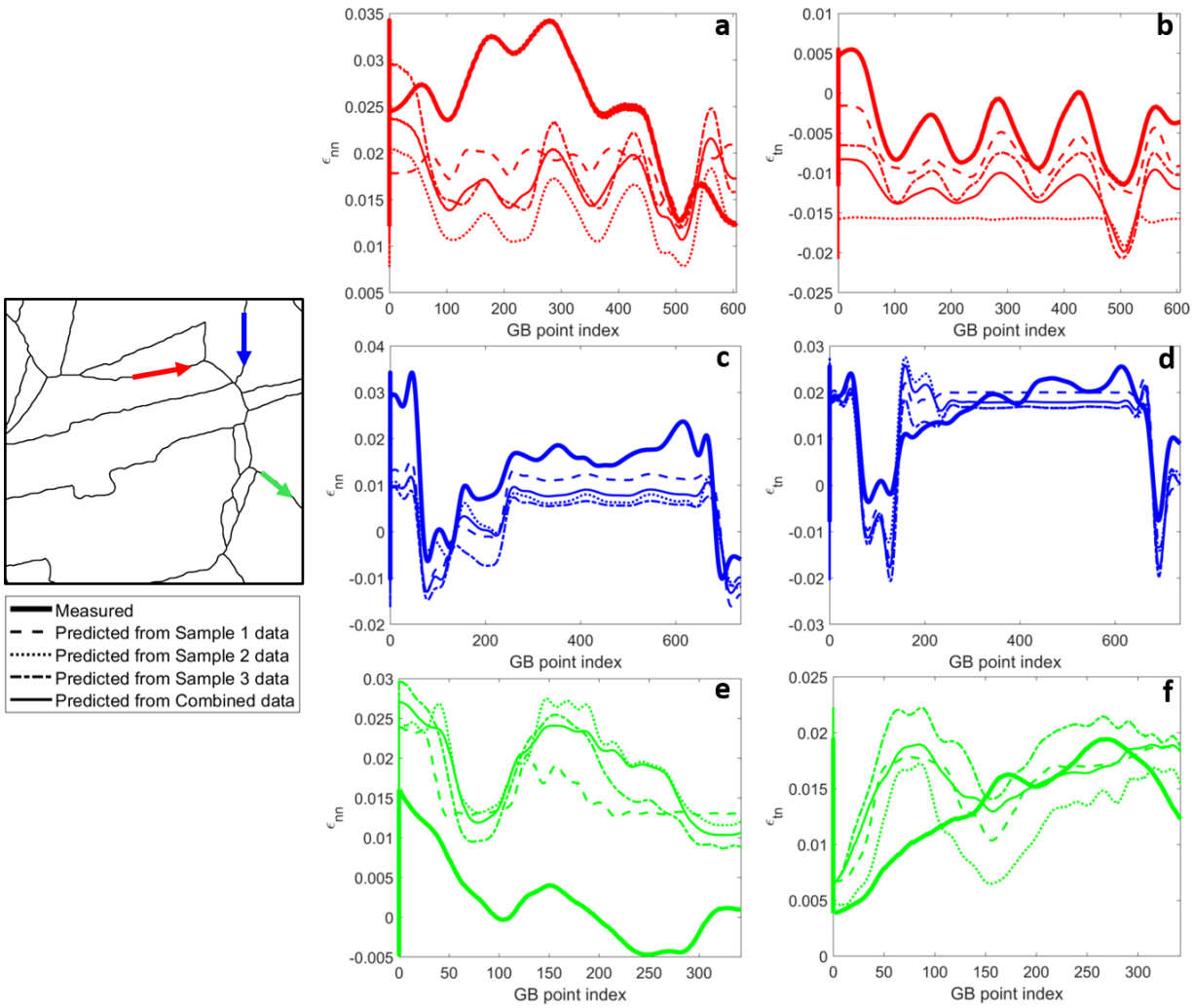

Fig. 6.15. Grain boundaries and color-coded arrows showing the plotted boundaries from sample 1; (a) to (f) Line plots showing residual normal and shear strains measured and predicted by each of the 4 neural networks.

A few observations can be made from these plots. First, all 4 neural networks were capable of predicting the average levels of residual strain for most boundaries of sample 1. Second and even more promising, for most cases the neural networks are also able to predict local peaks and valleys along the boundary with good precision, which is especially visible in Fig. 6.15b. Lastly, the boundaries where the neural networks were least accurate can be explained by the inability of the neural networks to predict drastic changes in the mean strain along a straight boundary, as can be clearly seen in Fig. 6.15a and Fig. 6.15e. As expected, this single parameter fit is never going

to be able to predict such a large change in average strain levels without a corresponding large change on the input inclination angle. In other words, for the cases where the boundary inclination doesn't change much (along the boundary), the neural networks were not capable of producing good predictions for drastic changes in the measured residual normal strain. This shortcoming indicates, as expected, that other microstructural parameters (e.g., the crystal orientations of the neighboring grains, and the corresponding misorientation angle) definitely have an influence on the final local strain fields.

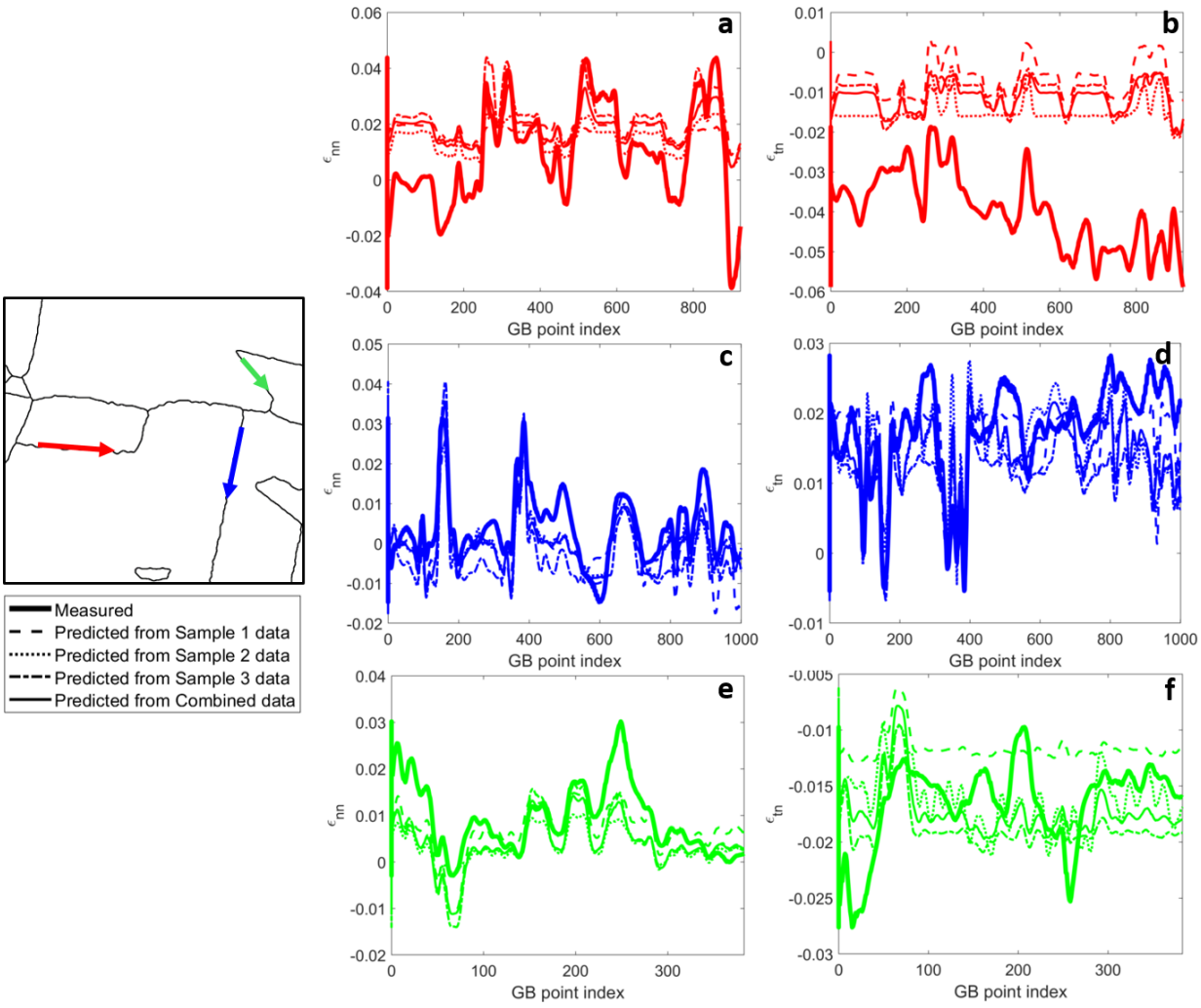

Fig. 6.16. Grain boundaries and color-coded arrows showing the plotted boundaries from sample 2; (a) to (f) Line plots showing residual normal and shear strains measured and predicted by each of the 4 neural networks.

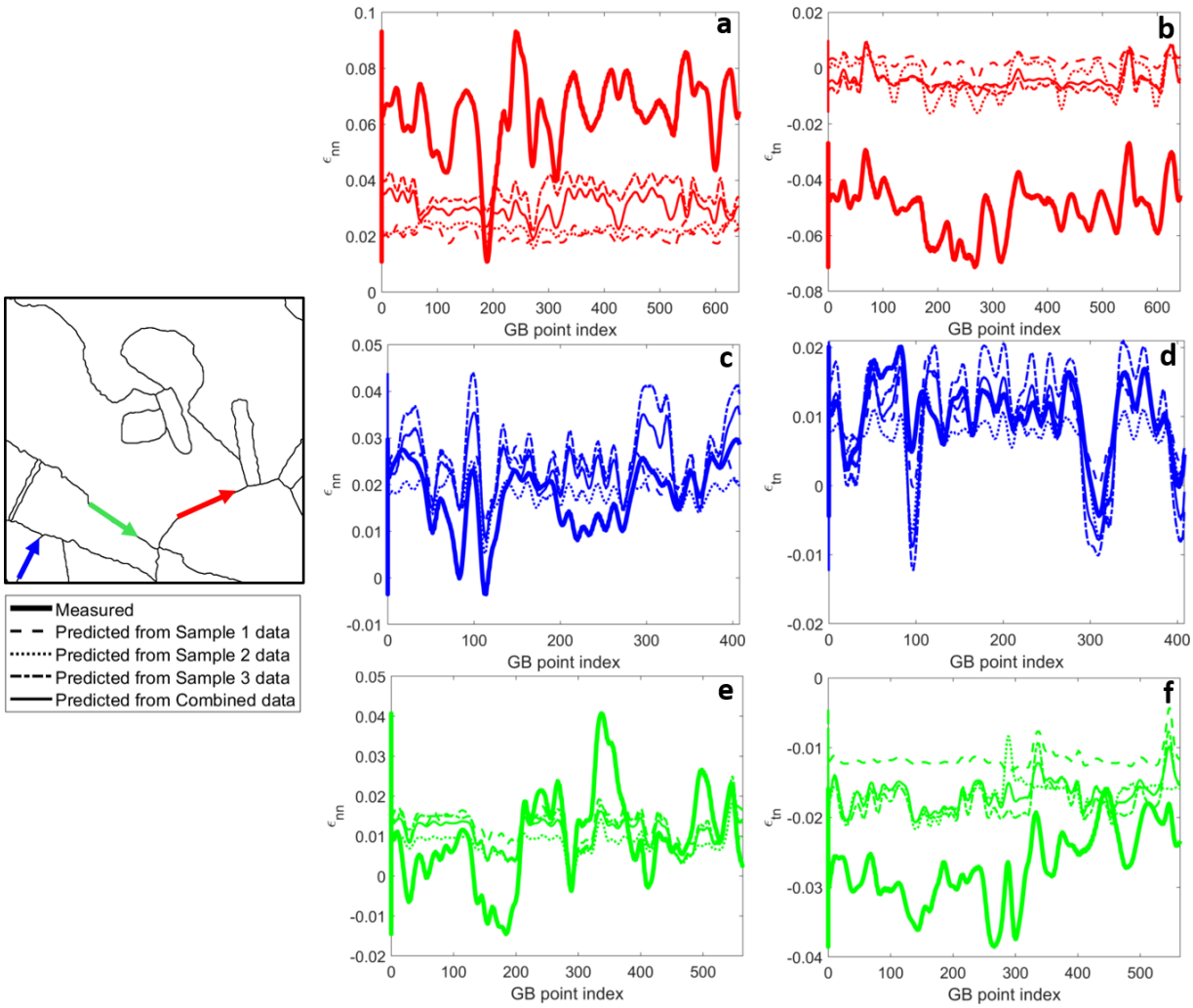

Fig. 6.17. Grain boundaries and color-coded arrows showing the plotted boundaries from sample 3; (a) to (f) Line plots showing residual normal and shear strains measured and predicted by each of the 4 neural networks.

The same observations made for sample 1 are also valid for the results from samples 2 and 3. Apart from those, now a few boundaries also showed relatively high error between the measured and predicted average levels of residual strains, mainly the results seen in Fig. 6.16b and Fig. 6.17a and b. These boundaries are the ones that present a combination of lower values of GB inclination angle (closer to horizontal) and relatively high residual strain levels. This might be part of the explanation to why the neural networks failed to produce good predictions for the average strains,

since low-value inputs are usually harder for the neural network to 'learn', since they may require very high values for the weights and biases.

In terms of comparing the different neural networks, the behavior observed in all samples was generally the same, where the neural network trained on the data of that specific sample performs better than all the other ones, with the combined neural network following as the second-best prediction. This result may have been expected, because even though the samples are nominally identical (same material batch and same nominal loading conditions etc.), they will still contain some uniqueness to them (i.e., there might be some unaccounted for variations of loading conditions or microstructural variations), which can explain why when trained on the same sample a neural network's predictions will outperform the other three networks'. However, the *overall best neural network* across all samples was the one trained with the *combined data*, i.e., the left third of each data set for each of the three samples. This cross-training bequeaths some information from each sample into the neural network, making the combined-trained neural network the close second best performer for most cases.

In order to evaluate how well the *combined* neural network really did in predicting local mantle strain, the correlation between measured and predicted strains (coefficient of the best fit line on a predicted vs. measured scatter plot) was calculated for each interrogated boundary. The average correlation achieved by the *combined* neural network was 0.65 for both normal and shear strains, with values varying from 0.21 (Fig. 6.15a) to 0.92 (Fig. 6.15d), indicating that for some boundaries the prediction was almost perfect, while for others it is not very reliable. Fig. 6.18a and b show the same plots shown in Fig. 6.17c and d, while Fig. 6.18c and d show correlation plots of the predicted vs. measured normal and shear strains, with the best fit lines used to calculate the correlations.

Also shown in Fig. 6.18 are the p-values for testing against the null hypothesis, with values being equal to 0 up to the 4th decimal place (considerably below the usual threshold of 5% for accepting the alternate hypothesis). This means that if there was no underlying correlation between predicted and measured strains (null hypothesis) the probability of obtaining results with the given correlations is very low, leading to the acceptance of the hypothesis that the neural network is statistically able to predict to some degree the measured residual strains (alternate hypothesis).

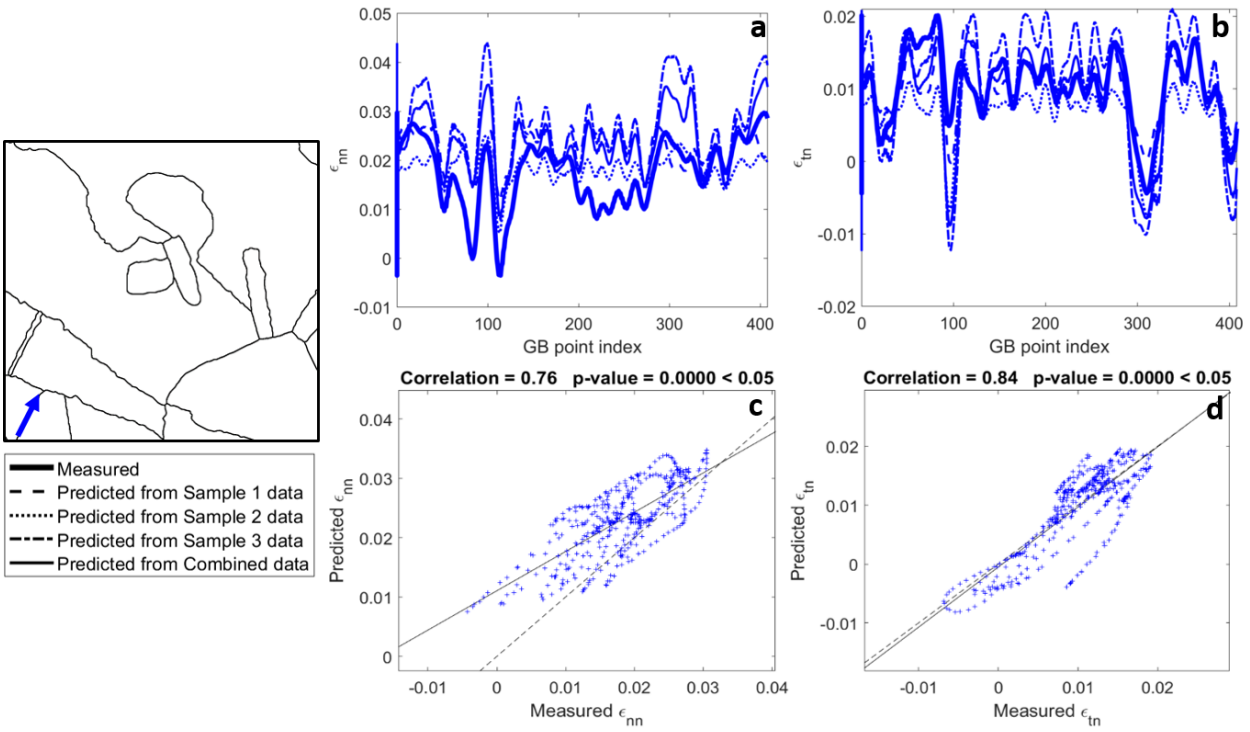

Fig. 6.18. Grain boundaries and color-coded arrow showing the plotted boundary from sample 3; (a) and (b) Line plots showing residual normal and shear strains measured and predicted by each of the 4 neural networks; (c) and (d) Correlation plots of predicted vs. measured normal and shear strains, showing the best-fit line used to calculate the correlation.

Another possible source of error for the proposed neural-network approach comes from sub-surface effects. The inclination angles used as input for the prediction of surface residual strains are measured from the projection of the grain boundaries onto the surface of the sample, as visualized in 2D surface microscopy. Consequently any influence on the inclination angle coming from the third-dimension of the grain structure cannot be accounted for explicitly in the grain

boundary angle. Furthermore, the existence of sub-surface grains and their effect on the strain accumulation at the surface is also not considered in any way, although there may be an indirect effect on the DIC-measured surface strain. The application of experimental techniques that can also resolve both the stress/strain field and the microstructure in three dimensions (such as high energy x-ray diffraction and digital volume correlation) would be needed in order to provide sub-surface 3D information for the training of the neural networks and thus possibly improve the networks' accuracy.

6.8 Summary

In this chapter, the HiDIC technique was used to measure residual strains at the microstructural level of three nominally identical heat treated stainless steel 709 samples. The larger grains resulting from the heat treatment allowed for a much higher grain to subset size ratio than in previous chapters. The residual strain fields were separated into core and mantle, with the results obtained inside the mantle regions being rotated to local GB coordinates (normal and tangential). The relationship between measured residual strains and 2 microstructural parameters (GB inclination and misorientation angle) was analyzed through the use of scatter plots. From this analysis, the GB inclination angle between the boundary and the horizontal was chosen as a candidate input variable for a single-input fitting neural network. Next, the architecture and the training methodology of such a neural network is presented, with a total of 5 different neural networks being trained using different subsets of the experimental data obtained from the 3 samples.

The GB inclination angle was shown to be a good predictor for residual strain levels inside the mantles of these samples (loading parameters such as temperature and maximum load might have an effect on how good of a predictor the GB inclination angle is). All the trained networks

produced statistically significant predictions for the strains, with their main weakness being identified in the situations where the strains varied drastically along the boundary, while the single input parameter was fairly constant along it, resulting in an impossibility of the neural network predicting the correct strains. A secondary weakness was observed in boundaries where the input (GB inclination) was fairly small (near horizontal boundaries), which is known to be a situation where neural networks have a hard time ‘learning’ to produce good predictions. The neural network with highest overall performance had been trained on a dataset that combined parts of all the samples, it achieved an average correlation value of 0.65 between measured and predicted residual strains.

Chapter 7: Conclusions and Future Work

This study presented an investigation of the inhomogeneous strain accumulation at the microstructure of a polycrystalline austenitic stainless steel loaded under plasticity and creep conditions, over a range of different temperatures, maximum stresses, and hold times. Relationships between strain accumulation and microstructural and loading parameters were also explored, with a focus on the role of grain boundaries and how strains accumulate in their vicinity. The comparison of microscale strain fields obtained from creep and plasticity experiments allowed us to investigate the differences between the microstructural response to these different loading conditions, with some observations about their interaction.

7.1 Conclusions

The initial macroscale experiments presented in Chapter 2 investigated the response of stainless steel 709 to plastic, creep and creep-fatigue loading under different loading condition. The results served as baseline for all the work presented subsequently. The main conclusions from this part of the study came from the comparison between room temperature and high temperature (650°C) creep response, which showed that room temperature creep resulted in much lower strain accumulation, with a much longer secondary creep stage, than at 650°C. The creep-fatigue results showed that the introduction of higher temperatures and hold times resulted in shorter lives, indicating that creep and fatigue interactions are present in this alloy's response.

After the macroscale experiments, the microscale response was investigated through the use of HiDIC (Carroll et al., 2010). The technique was successfully applied to measure residual strain fields at the grain scale of alloy 709 at room temperature and at 650°C. Changes on the

alignment procedure between the DIC-obtained strain field and EBSD-generated microstructural data were proposed with an order of magnitude improvement being achieved for the average alignment uncertainty. The resulting microscale strain fields showed that alloy 709 developed highly inhomogeneous strain fields at the microstructure level during plasticity, creep and creep-fatigue. The pattern of inhomogeneities resulting from creep and plasticity were compared, with the localization of residual strains being found to occur primarily in the vicinity of grain boundaries for all loading conditions. Furthermore, these heterogeneities were shown to form during the very early stages of loading, with hot-spots for strain accumulation appearing from the very first cycle and not changing with subsequent loading. Different sequences of creep and plastic loading were investigated and the result was the same for all tested cases.

Motivated by the desire to relate microscale measurements to the macroscale response of the material, the concept of the strain-based RVE was explored. A new method of experimentally measuring strain-based RVEs from residual strain fields obtained from HiDIC was developed as an improvement on methods presented by previous authors (Efstathiou et al., 2010; Ravindran et al., 2017). The proposed stereological method recognizes the strain-based RVE as an intrinsically statistical entity, instead of a deterministic material property, and through this understanding produces more reliable measurements of the strain-based RVE size from a given stain field. Synthetic strain fields generated from a Gaussian noise algorithm were used to demonstrate that the proposed new method required fewer data to produce statistically equivalent RVE-size measurements to a previously proposed method (Ravindran et al., 2017). Since the stereological method treats the RVE as a statistical entity, it comes with the intrinsic advantage of being able to estimate the probability that for a given box size, the average strains will converge to the global average, essentially producing an RVE-size probability distribution.

The stereological method for measuring strain-based RVEs was subsequently used to measure RVE sizes for plastic and creep loading conditions, over a range of different temperatures, maximum stresses and hold times. This allowed for a quantitative comparison between strain fields obtained from each of these conditions, with RVE sizes for plasticity being consistently higher than those obtained from pure creep. The samples that had both plasticity and creep applied to them (identified as plastic creep deformation type, where the sample was plastically loaded and then held at maximum stress for a period of time) had RVE sizes similar to the ones that were subjected to purely plastic loading (without hold time), leading to the conclusion that plasticity dominates the degree of inhomogeneity observed in the resulting strain field. A coordinate transformation from sample coordinates to local GB coordinates (normal and tangential to the boundary) was applied to the strains measured inside mantle regions (in the vicinity of GB), allowing for better visualization of the deformation at those locations. A correlation between RVE-sizes and the normal to shear strain ratios (inside mantle regions) was observed, with evidence being presented that both the RVE size and the local strain ratio are controlled by the underlying deformation mechanisms, suggesting that RVE size might be used as a proxy for the determination of mechanism changes.

During the exploration on the influence of grain boundary strain accumulation on the size of the RVE, some correlation between the GB inclination angle and the level of strains accumulated near grain boundaries was observed. Some further exploration into the correlation between strain accumulation and GB parameters (inclination and misorientation angles) was presented. The conclusion of this exploration was that the GB inclination angle had a very strong correlation with mantle strain levels, while the GB misorientation angle was shown to not have such a strong correlation. Motivated by this study on the correlations between microstructural

features and strain concentration levels, the use of a neural network trained on microstructural data to predict microscale strain fields was proposed. A first step in producing a neural network capable of predicting the entirety of the microscale strains was presented, with a single-input neural-network being deployed to predict strain accumulations in the vicinity of grain boundaries of heat-treated alloy 709 samples. The neural network predictions for residual strains near grain boundaries from the grain boundary inclination angle were shown to correlate well with experimental results. Several neural networks were trained on different combinations of input data, from three nominally identical samples. The neural networks trained on data from each sample were shown to be the best at predicting strain accumulations for that sample, while the neural network trained on the combined data from a portion of each sample was shown to be the overall best performer in predicting mantle strain accumulation. This result can be justified by the fact that the combined neural network received some information from each sample, which made it more capable of perceiving underlying differences in otherwise nominally identical samples (slight changes in loading conditions and microstructural differences resulting from a small number of grains within the region of interest).

7.2 Suggested Future Work

All the DIC measurements presented in this work were made on the surface of specimens. Therefore, there was no ability to identify through thickness effects that might be present due to the underlying microstructure. A suggested line of future work is to combine HiDIC and EBSD techniques with high energy near-field X-ray diffraction for three dimensional microstructural orientation measurements (Turner et al., 2016). The combined data would allow for identification of possible interactions between the underlying microstructure and strain accumulations on the surface. Furthermore, the use of far-field X-ray diffraction could allow for measurements of strains

accumulated below the surface, which could also help in understanding the microscale response of the material.

The development of a technique that allows for *in situ* strain measurements at similar length scales would allow for the measurements presented in this work to be made *during* loading. This would be of value, because the evolution of strain during loading could be explored in real time, instead of after the fact, as was the case for the *ex situ* technique applied here. Real-time measurements of the strain evolution would allow for further exploration of the differences between the microscale response of the material to plasticity and creep, with measurements made at the onset of the development of strain hot-spots. Furthermore, *in situ* measurements would include the elastic portion of the strains, allowing for the extension of the study presented here to the elastic regime.

The application of the stereological method to measure strain-based RVE sizes of different materials, with different crystal structures, or even of non-crystalline materials, could further clarify the relationships between microscale material characteristics (such as the microstructure of crystalline materials or the chain length of polymeric materials, for example) and the degree of inhomogeneity of the microscale strain field. This could serve as a starting point for a comprehensive study seeking to correlate deformation mechanisms and degree of inhomogeneity, which could prove useful for validating mechanism-based models.

Further development of the neural-network approach for predicting strain fields at the microscale based on microstructural information would require further testing and further analysis of the statistical correlations between strains and microstructural parameters. Further input parameters that could be added to the design of the neural network include, misorientation angle, Schmid factor, distance to nearest grain boundary, distance to triple points and orientation of

neighboring grains, among others. The inclusion of core-related microstructural parameters could potentially produce neural networks capable of predicting the entirety of the microscale strain field (not only the mantle strains). Furthermore, if loading parameters would also be included as inputs for the neural network, an even more general neural network capable of predicting strain fields for different microstructures loaded at different conditions could be achieved.

Appendix A: Modeling Creep-Fatigue Behavior of Stainless Steel 709

Modeling of creep-fatigue damage accumulation is an ongoing focus in the field of mechanical behavior of materials. Many models have been proposed for creep-fatigue damage (e.g., Sehitoglu, 1992), but since most of these are empirically obtained they require significant experimental data fitting, which makes the adoption of these models by industry very costly. Because of this, the most widely used model consists of adding fatigue and creep damage linearly, as obtained by Miner's rule and Robinson's rule respectively (American Society of Mechanical Engineers, ASME boiler and pressure vessel code).

$$\left(\Sigma(^{ni}/_{Ni}) + \Sigma(^{tj}/_{Tj}) = 1\right), \tag{A.1}$$

where *ni* is the number of cycles the structure is subjected to at given loading conditions, *Ni* is the number of cycles to failure at same loading conditions, *tj* is the time the structure has been loaded at those loading conditions and *Tj* is the time it would take for the structure to fail, again at the same loading conditions. It is easy to see that such a simple rule does not account for any coupling between fatigue and creep mechanisms. Because of this, for real life applications, empirically determined safety factors need to be applied to account for the expected coupling. For the specific case of austenitic stainless steels, the ASME boiler and pressure vessel code (American Society of Mechanical Engineers, ASME boiler and pressure vessel code), uses an experimentally determined bilinear envelope that restricts safe operation conditions to 0.3 for both fatigue and creep damage (in contrast to the linear rule that would give 0.5 damage for both).

Although we have only a limited number of data points, an attempt has been made to model our creep-fatigue results for stainless steel 709 using the Neu-Sehitoglu model described in (Neu

and Sehitoglu, 1989a, 1989b). In brief, the model consists of 3 damage equations, for the fatigue, creep and oxidation shares of total damage, as well as a unified constitutive equation employed to compute the stresses. The coupling of damage is done indirectly through the constitutive equation.

Unified constitutive equation: The applied constitutive model combines the effects of both creep and plasticity as inelastic strains. At lower stress levels, time dependent creep dominates, while at higher stress states plasticity is the main source of strain.

$$\dot{\varepsilon}^{in} = \begin{Bmatrix} Ao\left(\frac{\sigma}{K}\right)^{n1} exp\left(\frac{-\Delta H^{in}}{RT}\right) & \left(\frac{\sigma}{K}\right) \leq 1 \\ Ao\ exp\left[\left(\frac{\sigma}{K}\right)^{n2} - 1\right] exp\left(\frac{-\Delta H^{in}}{RT}\right) & \left(\frac{\sigma}{K}\right) \geq 1 \end{Bmatrix}, \tag{A.2}$$

where ΔH^{in} is the activation energy for inelastic deformation, A_o is a scaling constant for the inelastic deformation, n_1 is the exponent for creep dominated deformation, n_2 is the exponent for plasticity dominated deformation, T is the temperature in Kelvin, function $K(T)$ is the drag stress which is a function of temperature, R is the universal gas constant and σ is the applied stress. In addition to the inelastic strain rate, the elastic portion of the mechanical strain rate is calculated from Hooke's law while the thermal strain rate is calculated with the help of the uniaxial thermal expansion coefficient.

Fatigue damage: The fatigue damage calculation itself follows the usual Coffin-Manson formulation. It is important to note that the amount of fatigue damage is always calculated at room temperature, which serves to minimize the number of fatigue experiments required to calibrate the model for predictions. The equation below shows the classical relation between the strain range and the number of cycles to failure.

$$\frac{\Delta\varepsilon}{2} = \frac{\sigma_f'}{E}\left(2N_f^{fat}\right)^b + \varepsilon_f'\left(2N_f^{fat}\right)^c, \tag{A.3}$$

where $\Delta\varepsilon$ is the strain range, σ'_f is the fatigue strength coefficient, E is the Young's modulus, b is the fatigue strength exponent, ε'_f is the fatigue ductility coefficient, c is the fatigue ductility exponent and N_f^{fat} is the number of cycles to failure in pure fatigue at room temperature.

Oxidation damage: The second part of the damage comes from oxidation, which is completely neglected by the widely used linear model, but can be very significant in specific conditions.

$$\frac{1}{N_f^{ox}} = \left[\frac{H_{crit}}{\Phi_{ox} K p_{eff}}\right]^{-1/\beta} \frac{2(\Delta\varepsilon_{mech})^{\frac{2}{\beta}+1}}{\dot{\varepsilon}^{1-\frac{B}{\beta}}}, \tag{A.4}$$

where N_f^{ox} is the number of cycles to failure by oxidation, H_{crit} is a constant related to the critical oxide layer thickness, β is the mechanical strain range exponent, B is the thermal strain rate sensitivity exponent, $\Delta\varepsilon_{mech}$ is the mechanical strain range, and

$$Kp_{eff} = \int_0^{tc} Do\ exp\left(\frac{-\Delta H^{ox}}{RT}\right) dt, \tag{A.5}$$

is the effective oxidation constant that describes the growth of oxide thickness in time, with D_o a scaling constant for oxidation, and ΔH^{ox} the activation energy for oxidation. In addition,

$$\Phi_{ox} = \frac{1}{tc}\int_0^{tc} exp\left[-\frac{1}{2}\left(\frac{\dot{\varepsilon}_{th}/\dot{\varepsilon}_{mech}+1}{\xi^{ox}}\right)^2\right] dt, \tag{A.6}$$

is a phasing factor that relates oxidation damage to the ratio of thermal and mechanical strain rates, $\dot{\varepsilon}_{th}$ and $\dot{\varepsilon}_{mech}$ respectively, and ξ_{ox} is the oxidation phasing constant.

Creep damage: The creep damage formulation follows a similar accumulation law as the oxidation damage.

$$\frac{1}{N_f^{cr}} = \int_0^{tc} A_{cr}\ \Phi_{cr}\ exp\left(\frac{-\Delta H^{cr}}{RT}\right)\left(\frac{\alpha_1\sigma + \alpha_2\sigma_h}{K}\right)^m dt, \quad \text{(A.7)}$$

where N_f^{cr} is the number of cycles to failure by creep, A_{cr} is a scaling constant for creep, ΔH^{cr} is the activation energy for creep, α_1 is the stress state constant, α_2 is the hydrostatic stress sensitivity constant, σ and σ_h are the stress and hydrostatic portion of the stress, m is the creep stress exponent, and

$$\Phi_{cr} = \frac{1}{tc}\int_0^{tc} exp\left[-\frac{1}{2}\left(\frac{\dot{\varepsilon}_{th}/\dot{\varepsilon}_{mech}{}^{-1}}{\xi^{cr}}\right)^2\right] dt, \quad \text{(A.8)}$$

is the phasing factor and ξ_{cr} is the creep phasing constant.

These four equations (A.2, A.3, A.4 and A.7) require a total of 23 constants listed in Table A.1. Most of their values were obtained for similar materials found in the references indicated. Only three of the parameters (the scaling constants for plasticity, oxidation, and creep) were fitted to experimental data.

Table A.1. List of material constants used for the Neu-Sehitoglu model.

Constant	Description	Value	Obtained
α	Linear thermal expansion coefficient	1.86e-5 mm/mm-°C	Matweb, for ss316
E	Young's modulus	194994 - 73.855*T MPa (T in Celsius)	American Iron and Steel Institute, for ss316
$n1$	Exponent for creep dominated deformation	5.4	Neu and Sehitoglu (1989b) for 1070 steel
$n2$	Exponent for plasticity dominated deformation	8.3	Neu and Sehitoglu (1989b) for 1070 steel
K	Drag stress	331.7 - 0.2061*T MPa (T in Celsius)	Upadhayay et al. (2018) for ss709
Ao	Scaling constant for inelastic deformation	5e9	Fitted to data
ΔHin	Activation energy for inelastic deformation	277000 J/mol	Alomari et al. (2017) for ss709
$\sigma'f$	Fatigue strength coefficient	738.4 MPa	Non-linear least squares fit to room temperature (RT) fatigue data
b	Fatigue strength exponent	-0.055	
$\varepsilon'f$	Fatigue ductility coefficient	0.04251	
c	Fatigue ductility exponent	-0.3322	
ξox	Oxidation phasing constant	1.3	Calculated from oxidation data from Zamrick et al. (1996) for ss316
B	Thermal strain rate sensitivity	0.75	Sehitoglu and Boismier (1990) for Mar-M247 nickel alloy
β	Mechanical stain range exponent	1.5	
Do	Oxidation scaling constant	8.68e5	Fitted to data
ΔHox	Activation energy for oxidation	260722 J/mol	Calculated from oxidation data from Buscail et al. (2014) for ss316
Hcr	Constant related to critical oxide thickness	2.4e-6 m	Sehitoglu and Boismier (1990) for Mar-M247 nickel alloy
ξcr	Creep phasing constant	0.5	Neu and Sehitoglu (1989b) for 1070 steel
ΔHcr	Activation energy for creep	277000 J/mol	Alomari et al. (2017) for ss709
Acr	Creep scaling constant	5e11	Fitted to data
m	Creep stress exponent	11.34	Neu and Sehitoglu (1989b) approximation of phase 1 creep
$\alpha 1$	Stress state constant	1/3	Assumption of no creep damage under compression
$\alpha 2$	Hydrostatic stress sensitivity constant	1	

Three reference materials were used to estimate the value of all constants. Stainless steel 316 is regarded as the commercially available material most closely related to stainless steel 709; 1070 steel was used for some inelastic properties, mainly regarding the shape of the stress strain curve (not the actual values); and Mar-M247, a nickel alloy was used to estimate some oxidation constants, since both materials are expected to form chemically equivalent oxides.

From the list in Table A.1, of special interest are: ΔHin and ΔHcr were assumed to be the same, in line with the assumption of the constitutive model that both creep and plasticity are treated as inelastic strains; K the drag stress is assumed to be equal to the yield strength; and m the creep exponent that has a higher than normal value (usually within 1-7), this is because with cyclic loading the material has to undergo a portion of primary creep every cycle so the exponent is expected to be higher than the ones calculated for the minimum creep rate.

Fig. A.1 shows the thermomechanical fatigue experimental data obtained for 17 hourglass samples loaded at room temperature (RT) and 650°C (results for experiments with hold times at maximum stress are also shown), along with Coffin-Manson fits for both the RT and 650°C pure fatigue tests. The strain range for these load-control experiments was estimated from the strain range measured at half-life.

Fig. A.2 shows the Neu-Sehitoglu model prediction of experimental creep-fatigue data for fatigue at 650 °C, with no hold time, 2 minutes hold time and 30 minutes hold time. The three curves show, with varying degrees, a transitioning behavior from creep dominated damage at lower strain rates to fatigue dominated damage at higher strain ranges.

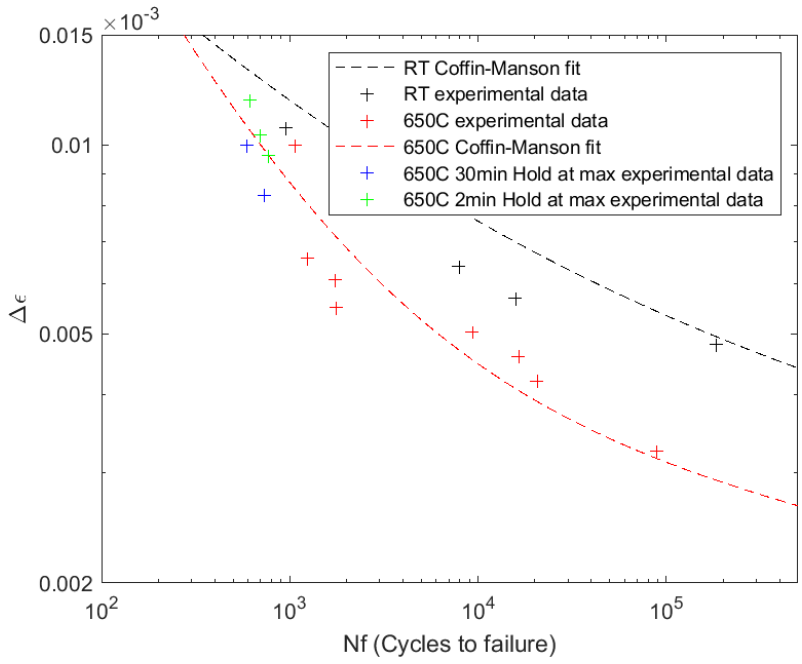

Fig. A.1 Thermomechanical fatigue experimental data along with Coffin-Manson fits for pure fatigue experiments at RT and 650°C.

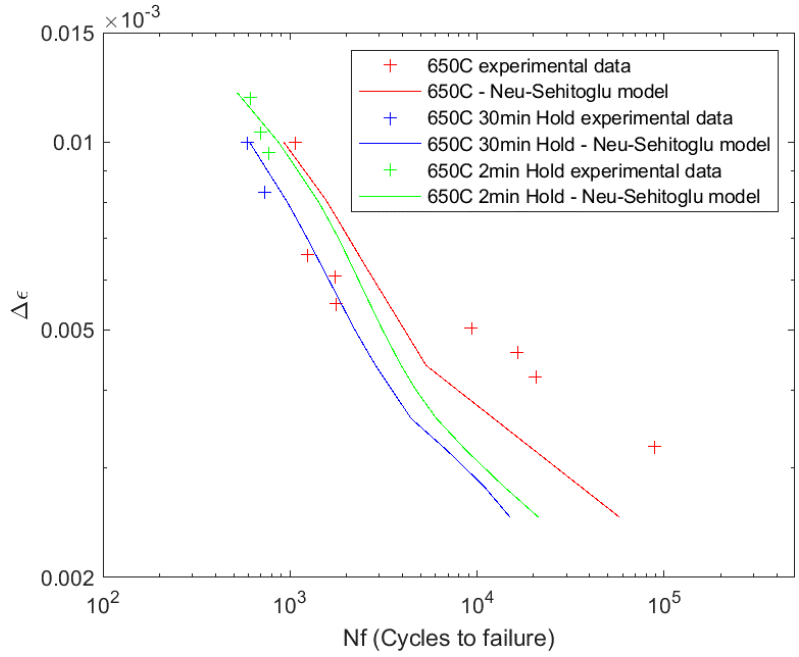

Fig. A.2. Neu-Sehitoglu model predictions along with experimental data.

Finally, in order to assess the validity of the model and to compare it to the well-established linear model, a plot showing fatigue damage vs. creep damage can be constructed, using the data

points with hold times. Fig. A.3 shows a plot of Fatigue damage vs. Creep damage, for the creep-fatigue data points shown in Fig. A.2, calculated using both the linear model and the Neu-Sehitoglu model. Along with the data points, two lines are drawn, showing the assumed limits from the linear model and from the ASME recommended bilinear envelope. For the linear model, the fatigue damage is taken directly from the Coffin-Manson fit of experimental data at 650°C, while the creep damage is calculated using creep data obtained from Potirniche (2019) and Shaber et al. (2019). It is interesting to note that, because of this, the linear model takes an approach that overestimates the fatigue damage, since at high temperatures (even without hold times) there is considerable creep damage occurring, in order to compensate for underestimating creep damage, that is calculated considering uniaxial creep instead of cyclic creep (lower creep exponent and hence less deformation).

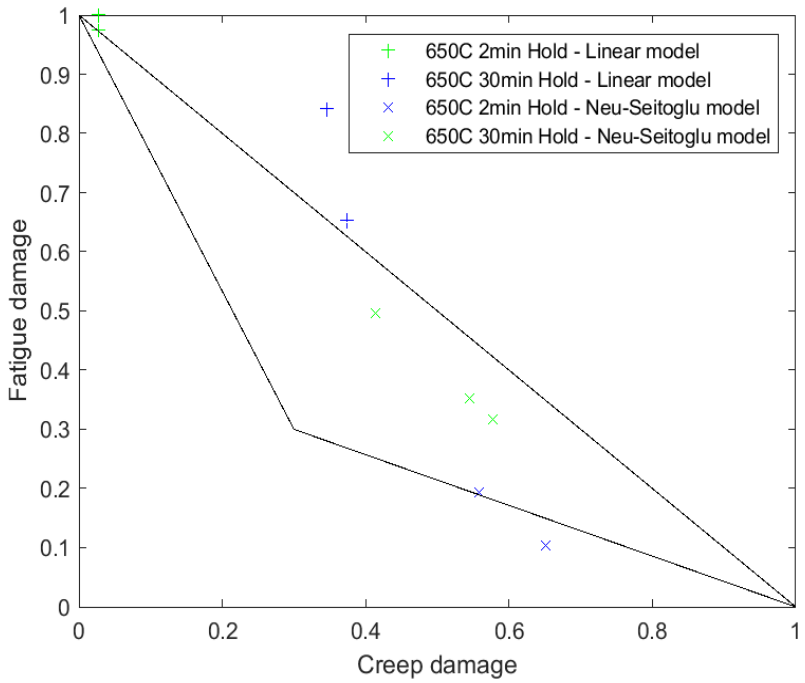

Fig. A.3 Fatigue vs. Creep damage for linear model and Neu-Sehitoglu model.

The results from both models are mostly above the ASME recommended envelope, which is expected, since the ASME code is supposed to give a conservative basis for thermomechanical

fatigue design. That being said, the results for the linear model are further away from the envelope, which would indicate a less conservative approach than the Neu-Sehitoglu model. Since for the same data points the results indicate a more critical combination of fatigue and creep damage. One of the points from the Neu-Sehitoglu model did fall below the ASME recommendation, which would indicate that the code might actually be non-conservative for certain conditions.

Appendix B: Further Exploration on Standard Deviation and Centered Box Growth Methods and Attempted Improvements

This appendix presents a further exploration on the standard deviation (Efstathiou et al., 2010) and centered box growth (Ravindran et al., 2017) methods for experimentally measuring strain-based RVEs. A few attempted improvements for each method are also listed.

B.1 Standard Deviation Method

The main identified disadvantage of the standard deviation method was the fact that it requires a relatively large strain field in order to measure the strain-based RVE (strain field ≥ 2*RVE size). A secondary disadvantage of the method comes from a subjectivity of the line fit to the trailing points in which the method relies to obtain the strain-based RVE size.

The first attempt at improving the method consisted of taking many (e.g., 1,000) boxes randomly selected from within the strain field, instead of taking the boxes in a non-overlapping grid. Fig. B.1a shows an experimental strain field for which the grid-based standard deviation method (Efstathiou et al., 2010) does not prodce a reliable strain-based RVE measurement. Fig. B.1b shows the plot of the standard deviation of box averages vs. box size for the grid-based method. This is a case similar to the one shown in Fig. 4.3, where it is very difficult to fit a line to the trailing end of the plot. Fig. B.1c shows the plot of the standard deviation of box averages vs. box size for 1,000 randomly selected boxes (intead of boxes in a grid). It is possible to see that by selecting multiple random boxes the resulting plot does not decrease to zero at box sizes above half the strain field, because even for large box sizes one can still select 1,000 random boxes from within the field of view (as long as it is allowed that boxes overlap). Even though that is promising

and could lower the field of view requirement of the standard deviation mehod, the secondary disadvantage of the method becomes even more pronounced with the new approach. Fig. B.1c shows two possible line fits to the trailing points of the plot that produce largely different RVE sizes. Both the subjectivity of how many trailing points should be used to fit the line and the subjectivity of how much deviation from linearity is required to estimate the RVE size, make this attempted improvement still unreliable at producing strain-based RVE measurements.

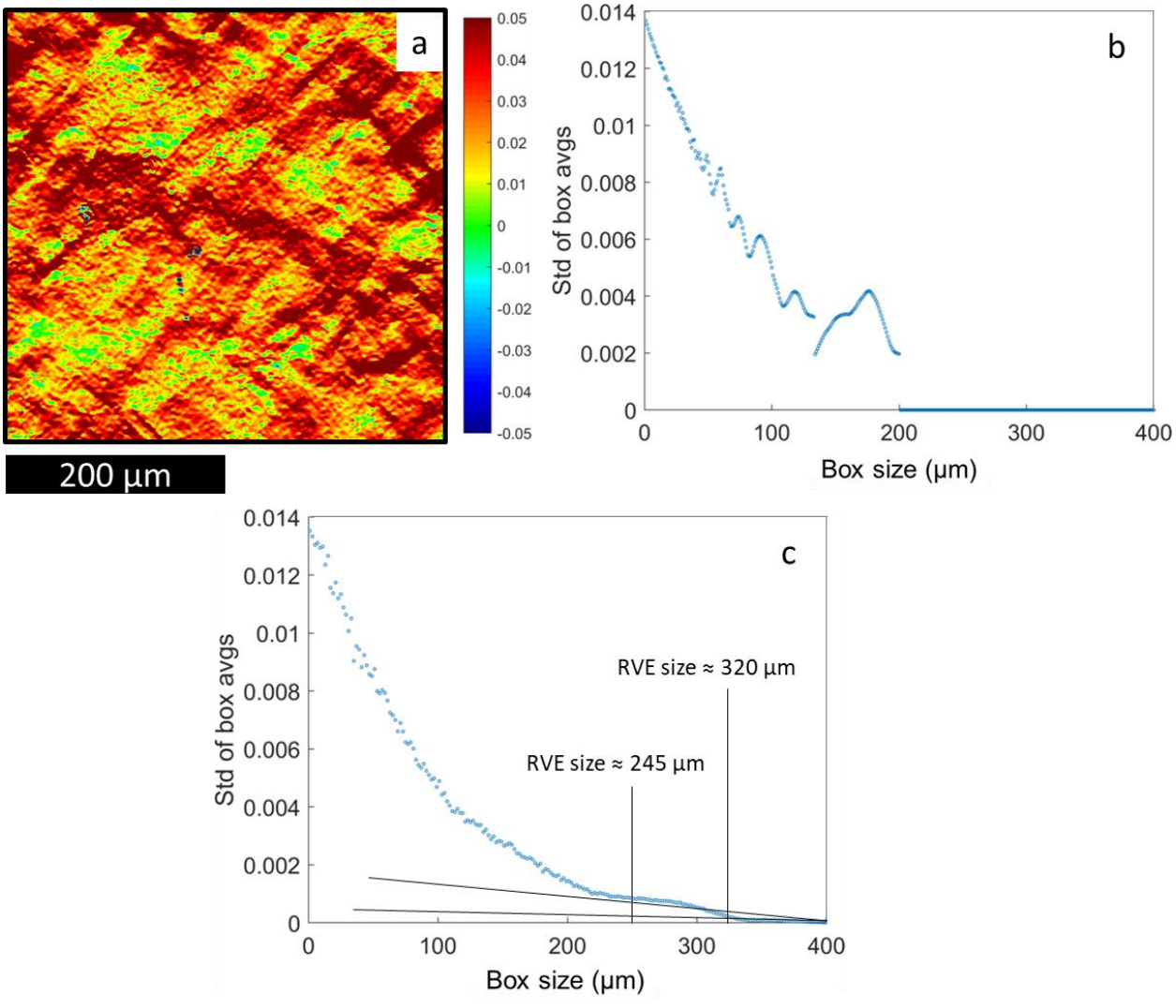

Fig. B.1. (a) Experimental strain field for which the grid-based standard deviation method cannot produce a reliable RVE measurement; (b) Standard deviation of box averages vs. box size plot for boxes taken in a grid; and (c) the same, but for 1,000 randomly selected, along with two possible line fits that result in very different RVE sizes.

In order to further explore the issue that arises from the line fit to these trailing points, a study using fully randomized strain fields taken from normal distributions with different means and standard deviation values was performed. Fig. B.2a shows a random field taken from the normal distribution with mean = 0.008 and standard deviation = 0.025, while Fig. B.2b shows a random field taken from the normal distribution with mean = 0.05 and standard deviation = 0.05. Fig. B.2c and d show the standard deviation of box averages vs. box size plot (from 1,000 randomly selected boxes) for the fields shown in Fig. B.2a and Fig. B.2b respectively.

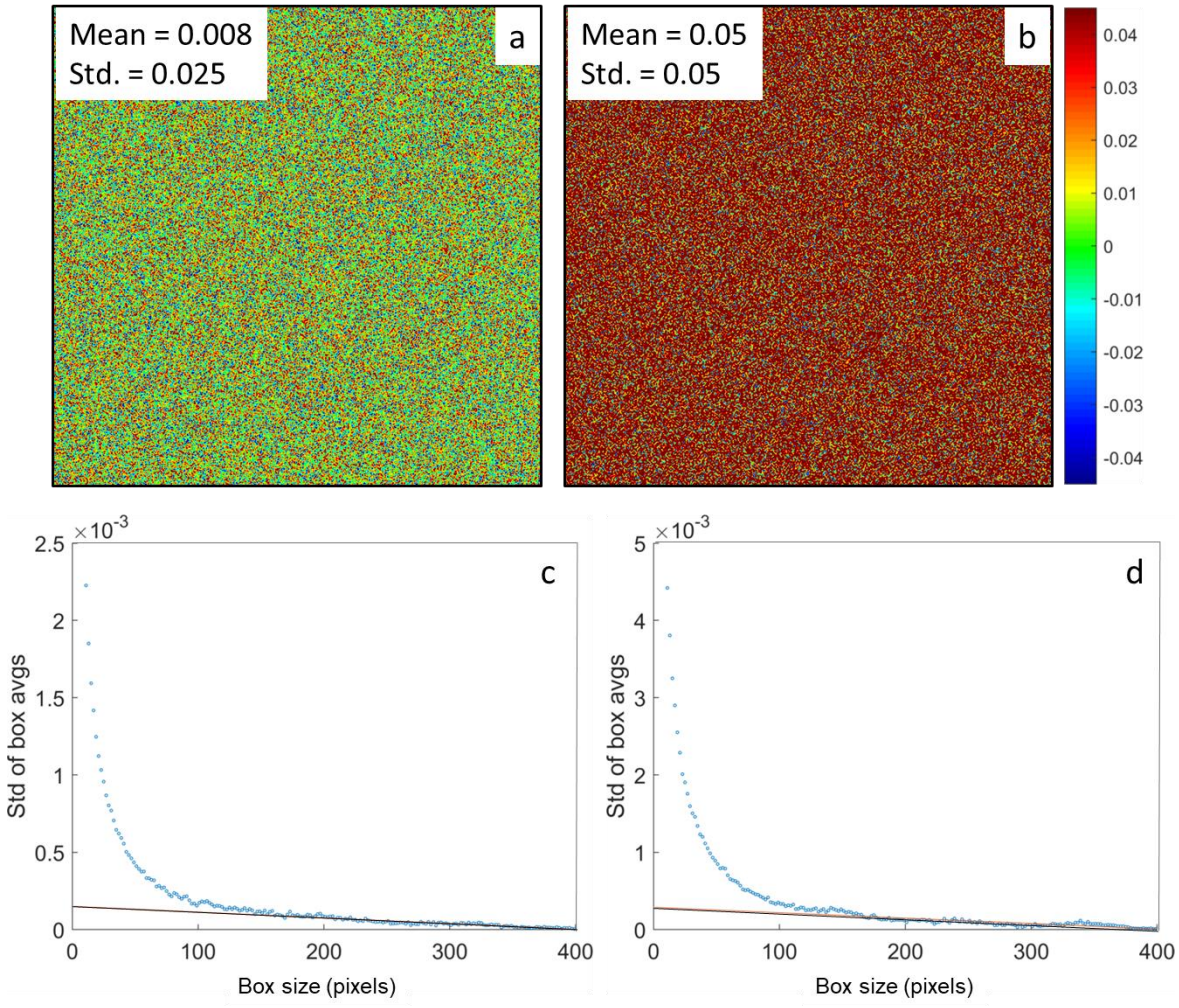

Fig. B.2. (a) Random strain field taken from the normal distribution with mean = 0.008 and standard deviation = 0.025; (b) mean = 0.05 and standard deviation 0.05; (c) Standard deviation of box averages vs. box size plot for the strain field of (a); and (d) Standard deviation of box averages vs. box size plot for the strain field of (b).

The idea behind using random fields taken from the normal distribution was that by changing the standard deviation, the resulting size of the RVE could be directly controlled. The immediate observation from these results is that even with idealized fully randomized "strain" fields, the plots do not reach a plateaus, and therefore there is still the need to fit a line to the trailing points of the plot. Furthermore, the subjectivity of the line fit is still present, making the RVE size prediction still unreliable. Similar results were obtained for a wide range of tested means and standard deviations for the normal distribution from which the random fields were generated.

B.2 Centered Box Growth Method

The main identified disadvantage of the centered box growth method was the fact that it is highly dependent on the location of the strains measurements within the sample. The example shown in Fig. 4.5, where the average strains inside the centered box coincidentally converged to the global average for very small box sizes, is only one of the possible situations where the method fails to produce reliable strain-based RVE size measurements. Fig. B.3a, b and c show three more cases where the centered box growth method cannot estimate the correct strain-based RVE size. All three cases were taken from synthetic strain fields with a scale factor of 8, generated as described in Section 4.3.1. The stereological method (with 10,000 randomly selected boxes from 1 scale-factor 8 synthetic strain field) and the centered box growth method (with 10,000 different scale-factor 8 synthetic strain fields) predict an RVE size of ~200 pixels for these strain fields (considering the 80% threshold and a ±5% margin from the global average strain). It is easy to see that none of the plots in Fig. B.3 produce a strain-based RVE size measurement of ~200 pixels. The plot in Fig. B.3a appears to converge at around 100-150 pixels, but then jumps out of the margin, coming back only at around 450 pixels. The plot in Fig. B.3b enters the margin at around 150-200 pixels, but overshoots it, only coming back at around 480 pixels. The plot in Fig. B.3c

converges to some value just outside the margin at around 150 pixels, but only really falls within the margin at around 450 pixels. In all three cases, judging convergence introduces some degree of subjectivity, hurting the reliability of the method.

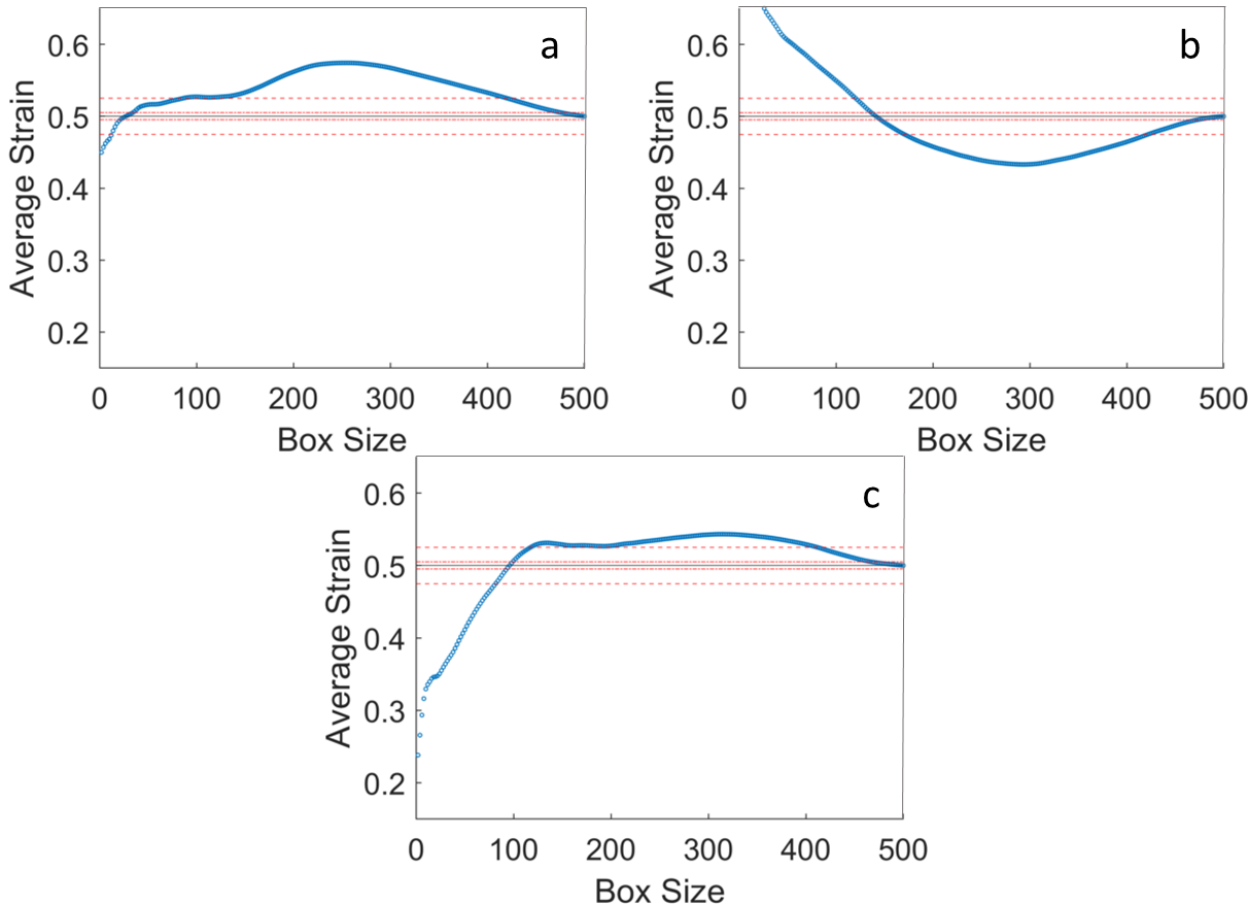

Fig. B.3. Average strain vs. box size plots for three more cases where the centered box growth method fails to produce reliable strain-based RVE measurements.

The final test that gave rise to the idea behind the stereological method (of considering the RVE an inherently statistical entity) is shown in Fig. B.4, where the average strain vs. box size plots for 1,000 different scale-factor 8 synthetic strain fields are plotted on the same axis. The statistical nature of the RVE can be easily grasped from this plot, which essentially shows that for 100% of the 1,000 synthetic strain fields, a box size of ~410 pixels converges to the global average (for a margin of ±5%), while for 80% of the 1,000 synthetic strain fields, a box size of ~210 pixels

converges to the global average (again using the margin of ±5%). The stereological method uses the same logic, but with the advantage of not requiring such a large number of strain fields to produce these probability distributions.

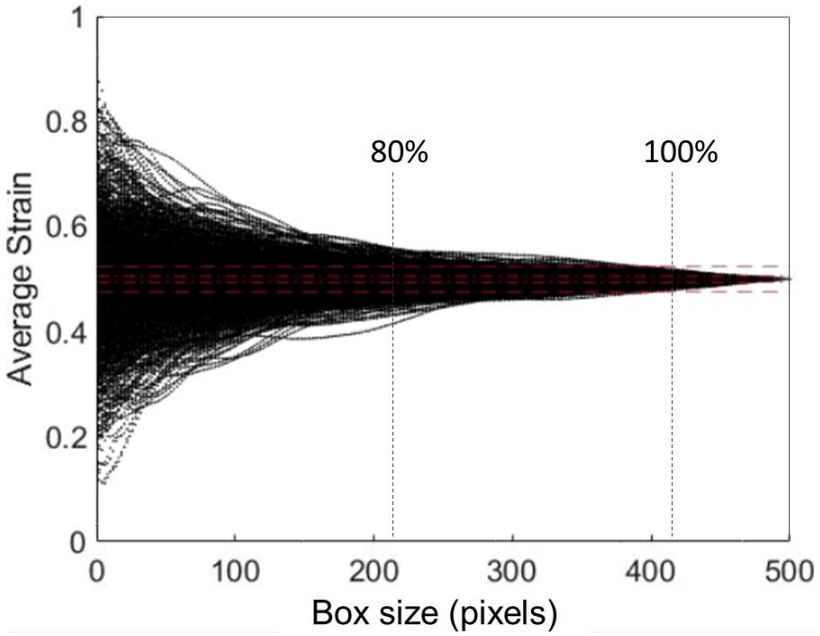

Fig. B.4. Average strain vs. box size plots for 1,000 different scale-factor 8 synthetic strain fields, with vertical dashed lines showing the box sizes where 80% and 100% of the strain fields converge to within a ±5% margin from the global average.

Appendix C: Study of Grain Growth during Heat Treatment of Alloy 709

In this appendix, a detailed study of the grain growth during heat treatment of alloy 709 is presented. The heat-treatment used to generate the large-grain samples used in Chapter 6 was selected after performing this study.

C.1 Uniaxial Tensile Tests of Heat-Treated Samples

Four dog-bone samples were heat treated for 48 hours under 700, 1100, 1150 and 1200°C. Uniaxial tensile tests were conducted under displacement control with a strain rate of 0.05% s^{-1}. The resulting stress vs. strain curves are shown in Fig. C.1, along with a curve obtained for an as-received sample. These tests were conducted to certify that even after the heat-treatment, the samples could still be loaded using the same experimental setup described in Chapter 2.

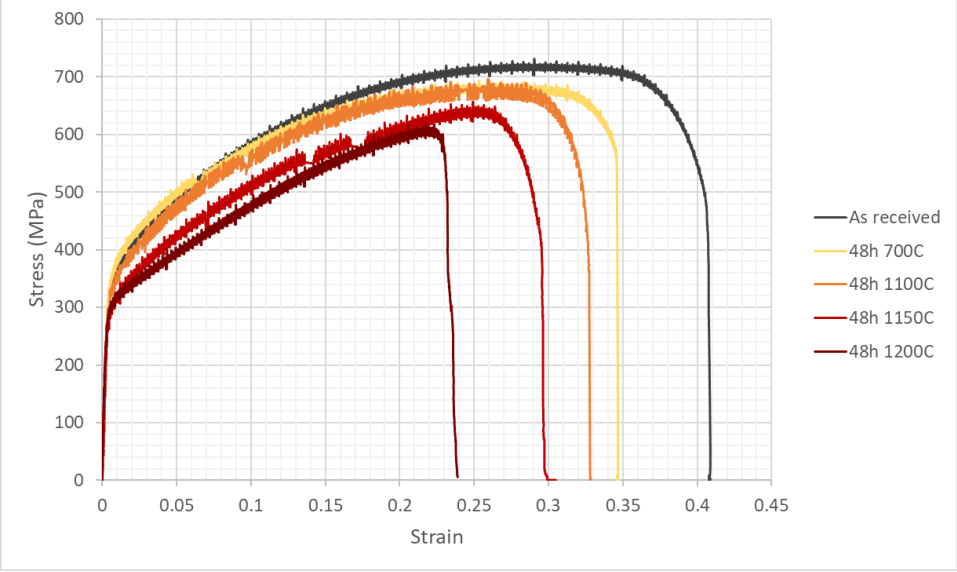

Fig. C.1. Stress vs. strain curves for 5 dog-bone samples, including an as-received sample and four samples heat-treated for 48 h at 700, 1100, 1150 and 1200°C.

C.2 Grain Growth

After optical microscopy inspection of the samples tested in the previous section, it was clear that the temperatures below 1200°C had very little impact on grain size. Fig. C.2 shows an optical image taken of the etched surface (etching procedure is described in Section 3.1.3) of an as-received sample, followed by five optical images taken of samples heat treated at 1100°C for 12, 24, 48, 96 and 192 hours. Some growth was observed, but not enough to drastically change the grain to subset size ratio as was required for the study in Chapter 6.

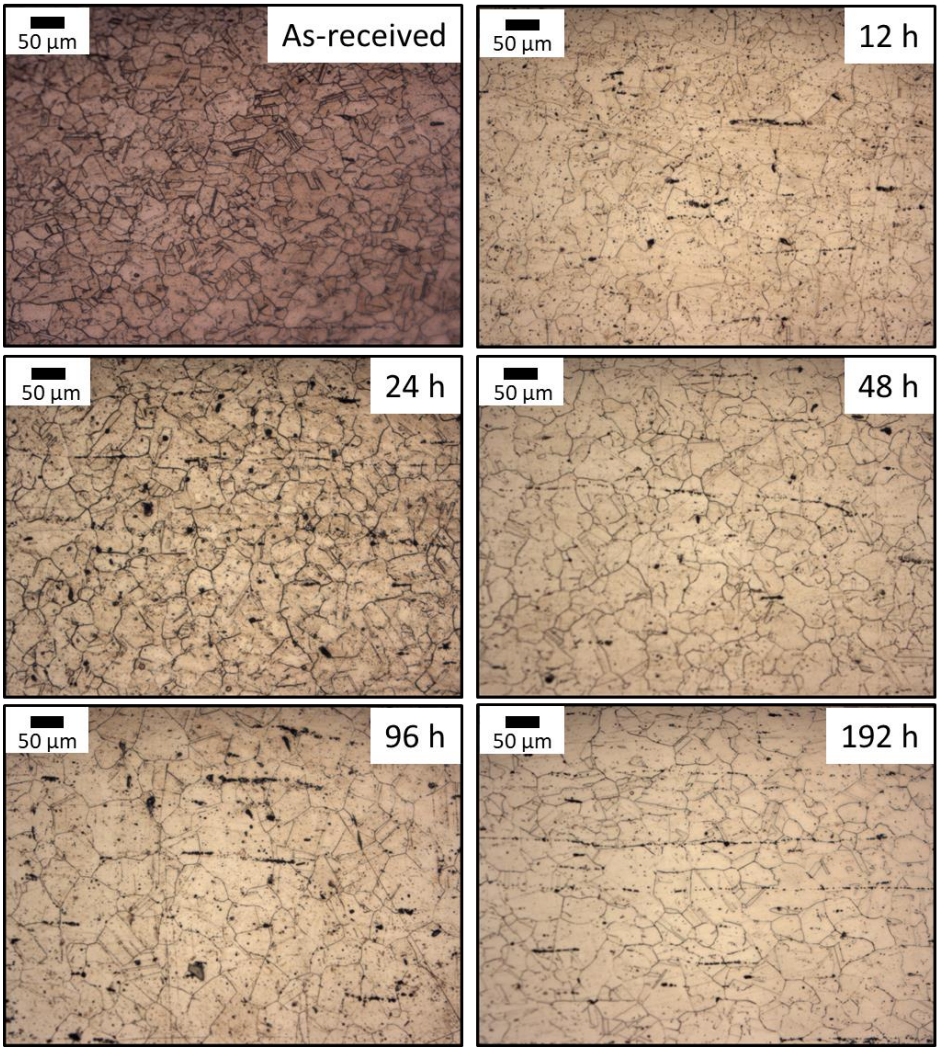

Fig. C.2. Optical images of the etched surface of an as-received sample and five samples heat treated at 1100°C for 12, 24, 48, 96 and 192 hours.

Fig. C.3 shows the optical images of the etched surface from two samples heat treated at 1200°C for 24 and 48 hours. Note that the scale used in Fig. C.3 is a larger than the scale used in Fig. C.2, indicating that at 1200°C the material suffered a drastic increase in grain size. Fig. C.4 shows the average grain size vs. heat-treatment time for alloy 709 samples heat treated at 1100 and 1200°C. The average grain sizes reported here were measured using the line intercept tool built into Fiji-ImageJ (Schindelin et al., 2012), and because of that are not as reliable as the sizes reported in Fig. 6.1 (measured using EBSD).

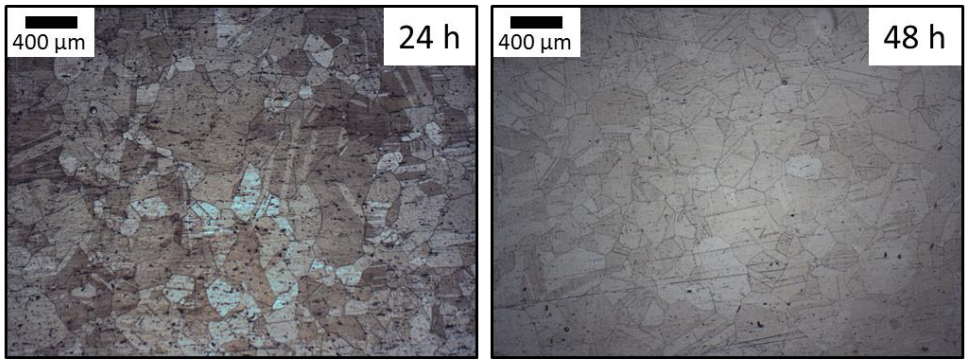

Fig. C.3. Optical images of the etched surface of two samples heat treated at 1200°C for 24 and 48 hours.

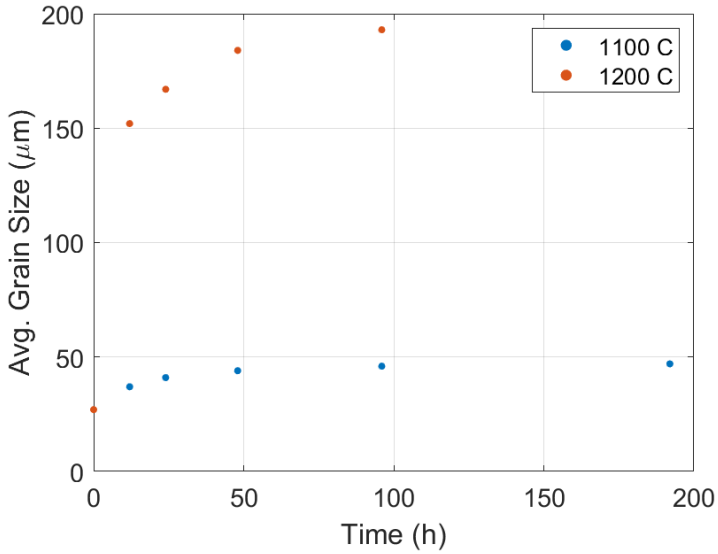

Fig. C.4. Average grain size vs. heat treatment time for alloy 709 samples heat treated at 1100 and 1200°C.

References

Abueidda, D. W., Koric, S., Sobh, N. A. and Sehitoglu, H., 2021. Deep learning for plasticity and thermo-viscoplasticity. *International Journal of Plasticity,* Volume 136: 102852.

Abuzaid, W. Z., Sangid, M. D., Carroll, J. D., Sehitoglu, H. and Lambros, J., 2012. Slip transfer and plastic strain accumulation across grain boundaries in Hastelloy X. *Journal of the Mechanics and Physics of Solids,* 60(6), pp. 1201-1220.

Abuzaid, W. Z., Sehitoglu, H. and Lambros, J., 2013. Plastic strain localization and fatigue micro-crack formation in Hastelloy X. *Materials Science and Engineering: A,* Volume 561, pp. 507-519.

Abuzaid, W. Z., Sehitoglu, H. and Lambros, J., 2016. Localisation of plastic strain at the microstructurlal level in Hastelloy X subjected to monotonic, fatigue, and creep loading: the role of grain boundaries and slip transmission. *Materials at High Temperatures,* 33(4-5), pp. 384-400.

Alomari, A., Kumar, N. and Murty, K. L., 2017. *Investigation on Creep Mechanisms of Alloy 709.* Proceedings of the ASME 2017 Nuclear Forum collocated with the ASME 2017 Power Conference Joint With ICOPE-17, the ASME 2017 11th International Conference on Energy Sustainability, and the ASME 2017 15th International Conference on Fuel Cell Science, Engineering and Technology. ASME 2017 Nuclear Forum. Charlotte, North Carolina, USA. June 26–30, 2017.

Alsmadi, Z. Y., Alomari, A., Kumar, N. and Murty, K. L., 2020. Effect of hold time on high temperature creep-fatigue behavior of Fe–25Ni–20Cr (wt.%) austenitic stainless steel (Alloy 709). *Materials Science and Engineering: A,* Volume 771, p. 138591.

Alsmadi, Z. Y. and Murty, K. L., 2021. Effect of Strain Range on High Temperature Creep-Fatigue Behaviour of Fe-25Ni-20Cr (wt.%) Austenitic Stainless Steel (Alloy 709). *Materials at High Temperatures,* 38(1), pp. 47-60.

American Iron and Steel Institute, *High-temperature characteristics of stainless steels,* Washington D.C.: Nickel Development Institute.

American Society of Mechanical Engineers, *ASME boiler and pressure vessel code,* New York: American Society of Mechanical Engineers, Boiler and Pressure Vessel Committee.

Ashby, M. F., 1972. A first report on deformation-mechanism maps. *Acta Metallurgica,* Volume 20(7), p. 887-897.

Bagri, A., Weber, G., Stinville, J. C., Lenthe, W., Pollock, T., Woodward, C. and Gosh, S., 2018. Microstructure and Property-Based Statistically Equivalent Representative Volume Elements for Polycrystalline Ni-Based Superalloys Containing Annealing Twins. *Metallurgical and Materials Transactions A,* 49(11), pp. 5727-5744.

Bargmann, S., Klusemann, B., Markmann, J., Scnabel, J. E., Schneider, K., Soyarslan, C. and Wilmers, J., 2018. Generation of 3D representative volume elements for heterogeneous materials: A review. *Progress in Materials Science,* Volume 96, pp. 322-384.

Bartali, A. E., Aubin, V. and Degallaix, S., 2009. Surface observation and measurement techniques to study the fatigue damage micromechanisms in a duplex stainless steel. *International Journal of Fatigue,* 31(11), pp. 2049-2055.

Bouchedjra, M., Kanit, T., Boulemia, C., Amrouche, A. and Belouchrani, M. E. A., 2018. Determination of the RVE size for polycrystal metals to predict monotonic and cyclic elastoplastic behavior: Statistical and numerical approach with new criteria. *European Journal of Mechanics and Solids,* Volume 72, pp. 1-15.

Brnic, J., Canadija, M., Turkalj, G. and Lanc, D., 2010. Structural Steel ASTM A709—Behavior at Uniaxial Tests Conducted at Lowered and Elevated Temperatures, Short-Time Creep Response, and Fracture Toughness Calculation. *Journal of Engineering Mechanics,* 136(9), pp. 1083-1089.

Buscail, H., Rolland, R. and Perrier, S., 2014. Cyclic oxidation of AISI 316 stainless steel - influence of water vapour between 800 and 1000°C. *Corrosion Engineering, Science and Technology,* 49(3), pp. 169-179.

Carroll, J. D., Abuzaid, W. Z., Lambros, J. and Sehitoglu, H., 2010. An experimental methodology to relate local strain to microstructural texture. *Review of Scientific Instruments,* 81(8), 083703.

Carroll, J. D., Abuzaid, W. Z., Lambros, J. and Sehitoglu, H., 2013. On the interactions between strain accumulation, microstructure, and fatigue crack behavior. *International Journal of Fracture,* Volume 180, pp. 223-241.

Carter, J. L. W., 2012. *Exploration of Local Strain Accumulation in Nickel-based Superalloys,* (Document No. osu1344646905)[Doctoral dissertation, Ohio State University]: OhioLINK Electronic Theses & Dissertations Center.

Carter, J., Zhou, N., Sosa, J., Shade, P., Pilchak, A., Kuper, M., Wang, Y., Fraser, H., Uchich, M. and Mills, M. , 2012. Characterization of Strain Accumulation at Grain Boundaries of Nickel-Based Superalloys. In Superalloys 2012 (eds E.S. Huron, R.C. Reed, M.C. Hardy, M.J. Mills, R.E. Montero, P.D. Portella and J. Telesman).

Chen, B., Hu, J. N., Wang, Y. Q., Kabra, S., Cocks, A. C. F., Smith, D. J. and Flewitt P. E. J., 2015. Internal strains between grains during creep deformation of an austenitic stainless steel. *Journal of Materials Science,* Volume 50, pp. 5809-5816.

Cheong, K.-S. and Busso, E. P., 2006. Effects of lattice misorientations on strain heterogeneities in FCC polycrystals. *Journal of the Mechanics and Physics of Solids,* 54(4), pp. 671-689.

Critchfield, T. R. and Johnson, O. K., 2020. Representative and statistical volume elements for grain boundary networks: A stereological approach. *Acta Materialia,* Volume 188, pp. 166-180.

Delaire, F., Raphanel, J. L. and Rey, C., 2000. Plastic heterogeneities of a copper multicrystal deformed in uniaxial tension: Experimental study and finite element simulations. *Acta Materialia,* Volume 48, pp. 1075-1087.

Di Gioacchino, F. and Quinta da Fonseca, J., 2013. Plastic Strain Mapping with Sub-micron Resolution Using Digital Image Correlation. *Experimental Mechanics,* Volume 53, pp. 743-754.

Ding, R., Yan, J., Li, H., Yu, S., Rabiei, A. and Bowen, P., 2019. Deformation microstructure and tensile properties of Alloy 709 at different temperatures. *Materials and Design,* Volume 176, 107843.

Echlin, M. P., Mottura, A., Wang, M., Mignone, P. J., Riley, D. P., Franks, G. V. and Pollock, T. M., 2014. Three-dimensional characterization of the permeability of W–Cu composites using a new “TriBeam” technique. *Acta Materialia,* Volume 64, pp. 307-315.

Efstathiou, C., Sehitoglu, H. and Lambros, J., 2010. Multiscale strain measurements of plastically deforming polycrystalline titanium: Role of deformation heterogeneities. *International Journal of Plasticity*, 26(1), pp. 93-106.

Eshelby, J. D., Frank, F. C. and Nabarro, F. R. N., 1951. The equilibrium of linear arrays of dislocations. *Philosophical Magazine,* Volume 42(327), pp. 351-364.

Githens, A., Ganesan, S., Chen, Z., Allison, J., Sundararaghavan, V. and Daly, S., 2020. Characterizing microscale deformation mechanisms and macroscopic tensile properties of a high strength magnesium rare-earth alloy: A combined experimental and crystal plasticity approach. *Acta Materialia,* Volume 186, pp. 77-94.

Gurney, K., 1997. *An introduction to neural networks.* London: UCL Press.

Hall, E. O., 1951. The deformation and aging of mild steel:III. Discussion of results. *Proceedings of the Physical Society. Section B,* 64(9), pp. 747-753.

Hielscher, R. and Schaeben, H., 2008. A novel pole figure inversion method: specification of the MTEX algorithm. *Journal of Applied Crystallography,* 41, pp. 1024-1037.

Hild, F. and Roux, S., 2012. Comparison of local and global approaches to digital image correlation. *Experimental Mechanics,* 52, pp. 1503-1519.

Hill, R., 1963. Elastic properties of reinforced solids: Some theoretical principles. *Journal of the Mechanics and Physics of Solids,* 11(5), pp. 357-372.

Jones, R. E., Templeton, J. A., Sanders, C. M. and Ostien, J. T., 2018. Machine Learning Models of Plastic Flow Based on Representation Theory. *Computer Modeling in Engineering and Sciences,* Volume 117(3), pp. 309-342.

Kang, J. Y., Choi, B.I., Lee, H.J., Kim, J. S. and Kim K. J, 2006. Neural network application in fatigue damage analysis under multiaxial random loadings. *International Journal of Fatigue,* 28(2), pp. 132-140.

Koohbor, B., Ravindran, S. and Kidane, A., 2016. Experimental Determination of Representative Volume Element (RVE) Size in Woven Composites. *Optics and Lasers in Engineering,* Volume 90, pp. 59-71.

Lall, A., Sarkar, S., Ding, R., Bowen, P. and Rabiei, A. , 2019. Performance of Alloy 709 under creep-fatigue at various dwell times. *Materials Science and Engineering: A,* Volume 761, p. 138028.

Lee, D. W., Hong, S. H., Cho, S. S. and Joo, W. S., 2005. A study on fatigue damage modeling using neural networks. *Journal of Mechanical Science and Technology*, 19(7), pp. 1393-1404.

Li, H.Y, Wang, X. F., Wei, D. D., Hu, J. D. and Li, Y. H. , 2012. A comparative study on modified zerilli–armstrong, arrhenius-type and artificial neural network models to predict high-temperature deformation behavior in t24 steel. *Materials Science and Engineering: A,* Volume 536, pp. 216-222.

Lin, Y. C., Zhang, J. and Zhong, J., 2008. Application of neural networks to predict the elevated temperature. *Computational Materials Science,* 43(4), pp. 752-758.

Liu, C., 2005. On the Minimum Size of Representative Volume Element: An Experimental Investigation. *Experimental Mechanics,* 45(3), pp. 238-243.

Mandelbrot, B. B. and van Ness, J. W., 1968. Fractional Brownian motions, fractional noises and applications. *SIAM Review,* 10(4), pp. 422-437.

Marquardt, D. W., 1963. An Algorithm for Least-Squares Estimation of Nonlinear Parameters. *SIAM Journal on Applied Mathematics,* 11(2), pp. 431-441.

Martinez, M. J. and Ponce, M. A., 2019. Fatigue damage effect approach by artificial neural network. *International Journal of Fatigue,* Volume 124, pp. 42-47.

MathWorks, 2020. *Deep Learning Toolbox: User's Guide (R2020b).* [Online] Available at: from https://www.mathworks.com/help/pdf_doc/deeplearning/nnet_ug.pdf [Accessed 22 October 2020].

Matweb, *AK Steel 316 Austenitic Stainless Steel Thermal Properties.* [Online] [Accessed January 2021].

McCulloch, W. S. and Pitts, W., 1943. A logical calculus of the ideas immanent in nervous activity. *Mathematical Biophysics,* Volume 5, pp. 115-133.

Mello, A. W., Nicolas, A. and Sangid, M. D., 2017. Fatigue strain mapping via digital image correlation for Ni-based superalloys: The role of thermal activation on cube slip. *Materials Science and Engineering: A,* Volume 695, pp. 332-341.

Meyersm, M. A. and Ashworth, E., 1982. Model for the effect of grain size on the yield stress of metals. *Philosophical Magazine A,* 46(5), pp. 737-759.

Mitchell, T., 1997. *Machine Learning.* New York: Mc Graw-Hill.

Motaman, S. A. H., Roters, F. and Haase, C., 2020. Anisotropic polycrystal plasticity due to microstructural heterogeneity: A multi-scale experimental and numerical study on additively manufactured metallic materials. *Acta Materialia,* Volume 185, pp. 340-369.

Mozaffar, M., Bostanabad, R., Chen, W., Ehman, K., Cao, J. and Bessa, M.A. , 2019. Deep learning predicts path-dependent plasticity. *Proceedings of the National Academy of Sciences* Dec 2019, 116 (52), pp. 26414-26420

Nakamachi, E., Tam, N. N and Morimoto, H., 2007. Multi-scale finite element analyses of sheet metals by using SEM-EBSD measured crystallographic RVE models. *International Journal of Plasticity,* Volume 23, pp. 450-489.

Naoi, H., Mimura, H., Ohgami, M., Sakakibara, M., Araki, S., Sogoh, Y., Ogawa, T., Sakurai, H. and Fujita, T., 1993. Development of tubes and pipes for ultra-supercritical thermal power plant boilers. *Nippon Steel Technical Report,* Volume 57, pp. 22-27.

Neu, R. W. and Sehitoglu, H., 1989a. Thermo-Mechanical Fatigue, Oxidation and Creep: Part I - Experiments. *Metallurgical Transactions,* Volume 20A, pp. 1755-1767.

Neu, R. W. & Sehitoglu, H., 1989b. Thermo-mechanical fatigue, oxidation and creep: Part II - life prediction. *Metallurgical Transactions,* Volume 20A, pp. 1769-1783.

Özdemir, I. and Yalçinkaya, T., 2014. Modeling of dislocation–grain boundary interactions in a strain gradient crystal plasticity framework. *Computational Mechanics,* Volume 54, pp. 255-268.

Padilla, H. A., Lambros, J., Beaudoin, A. J. and Robertson, I. M., 2012. Relating inhomogeneous deformation to local texture in zirconium through grain-scale digital image correlation strain mapping experiments. *International Journal of Solids and Structures,* 49(1), pp. 18-31.

Parker, J. D. and Stratford, G. C., 1996. Strain localization in creep testing of samples with heterogeneous microstructures. *International Journal of Pressure Vessels and Piping,* 68(2), pp. 135-143.

Park, J., Yoon, S., Kwon, T.-H. and Park, K., 2017. Assessment of speckle-pattern quality in digital image correlation based on gray intensity and speckle morphology. *Optics and Lasers in Engineering,* Volume 91, pp. 62-72.

Petch, N. J., 1953. The cleavage strength of polycrystals. *Journal of the Iron and Steel Institute,* Volume 174, pp. 25-28.

Porter, T. D.,Wang, Z., Gilbert, E. P., Kaufman, M. J., Wright, R. N. and Findley, K. O. , 2021. Microstructure evolution of alloy 709 during static-aging and creep-fatigue testing. *Materials Science & Engineering A,* Volume 801, p. 140361.

Potirniche, G., Stephens, R., Charit, I., Shaber, N., Ramirez, J., Taylor, M., Pugesek, H., Malmquist, P., and Glazoff, M.., 2019, Characterization of Creep-Fatigue Crack Growth in

Alloy 709 and Prediction of Service Lives in Nuclear Reactor Components (Final Report). United States: N.

Pujol, J. C. F. and Pinto, J. M. A., 2011. A neural network approach to fatigue life prediction. *International Journal of Fatigue,* 33(3), pp. 313-322.

Raabe, D., Sachtleber, M., Zhao and Z., Zaefferer, S. 2001. Micromechanical and macromechanical effects in grain scale polycrystal plasticity experimentation and simulation. *Acta Materialia,* Volume 49, pp. 3433-3441.

Randle, V. and Engler, O., 2000. *Introduction to Texture Analysis.* Boca Raton: CRC Press.

Ranganathan, S. I. & Ostoja-Starzewski, M., 2008. Scale-dependent homogenization of inelastic random polycrystals. *Journal of Applied Mechanics,* 75(5), 051008.

Rao, K. B. S., Sandhya, R. and Mannan, S. L., 1993. Creep-Fatigue Interaction Behavior of Type-308 Stainless-Steel Weld Metal and Type-304 Stainless-Steel Base-Metal. *International Journal of Fatigue,* 15(3), pp. 221-229.

Ravindran, S., Koohbor, B. and Kidane, A., 2017. Experimental characterization of meso-scale deformation mechanisms and the RVE size in plastically deformed carbon steel. *Strain,* 53(1), e12217.

Remy, L. and Petit, J., 2002. *Temperature-Fatigue Introduction.* s.l.:Elsevier.

Rotella, J. and Sangid, M. D., 2020. Microstructural-based strain accumulation during cyclic loading of Ni-based superalloys: The role of neighboring grains on interconnected slip bands. *Fatigue & Fracture of Engineering Materials & Structures,* 43(10), pp. 2270-2286.

Roters, F., Eisenlohr, P., Hantcherli, L., Tjahjanto, D.D., Bieler, T.R. and Raabe, D., 2010. Overview of constitutive laws, kinematics, homogenization and multiscale methods in crystal

plasticity finite-element modeling: Theory, experiments, applications. *Acta Materialia*, Volume 58, pp. 1152-1211.

Sachtleber, M., Zhao, Z. and Raabe, D., 2002. Experimental investigation of plastic grain interaction. *Materials Science and Engineering A*, Volume 336, pp. 81-87.

Salahouelhadj, A. and Haddadi, H., 2010. Estimation of the size of the RVE for isotropic copper polycrystals by using elastic–plastic finite element homogenisation. *Computational Materials Science*, 48(3), pp. 447-455.

Schindelin, J., Arganda-Carreras, I., Frise, E., V., Kaynig, Longair, M., Pietzsc, T., Preibisch, S., Rueden, C., Saalfeld, S., Schmid, B., Tinevez, J., White, D.J., Hartenstein, V., Eliceiri, K., Tomancak, P. and Cardona, A., 2012. Fiji: an open-source platform for biological image analysis. *Nature Methods*, 9(7), pp. 676-682.

Sehitoglu, H., 1992. Thermo-mechanical fatigue life prediction methods. in *Advances in Fatigue Lifetime Predictive Techniques*, ed. M. Mitchell and R. Landgraf (West Conshohocken, PA: ASTM International), pp. 47-76.

Sehitoglu, H. and Boismier, D. A., 1990. Thermo-Mechanical Fatigue of Mar-M247: Part 2—Life Prediction. *J. Eng. Mater. Technol.*, 112(1), pp. 80-89.

Shaber, N., Stephens, R., Ramirez, J., Potirniche, G. P., Taylor, M., Charit, I. and Pugesek, H., 2019. Fatigue and creep-fatigue crack growth in alloy 709 at elevated temperatures. *Materials at High Temperatures*, 36(6), pp. 562-574.

Slone, C. and Mills, M., 2016. Analysis of Strain Localization at High Angle Grain Boundaries During Creep of a Polycrystalline Superalloy Using SEM-Based Digital Image Correlation. *Microscopy and Microanalysis*, 22(3), pp. 2018-2019.

Sourmail, T., Bhadeshia, H. K. D. H. and MacKay, D. J. C., 2002. Neural network model of creep strength of austenitic stainless steels. *Materials Science and Technology,* Volume 18(6), pp. 655-663.

Stinville, J. C., Lenthe, W. C., Echlin, M. P., Callahan, P. G., Texier, D. and Pollock, T. M., 2017. Microstructural statistics for fatigue crack initiation in polycrystalline nickel-base superalloys. *International Journal of Fracture,* Volume 208, pp. 221-240.

Stinville, J. C., Lenthe, W. C., Miao, J. and Pollock, T. M., 2016. A combined grain scale elastic–plastic criterion for identification of fatigue crack initiation sites in a twin containing polycrystalline nickel-base superalloy. *Acta Materialia,* Volume 103, pp. 461-473.

Sutton, M. A., Orteau, J.-J. and Schreier, H. W., 2009. *Image Correlation for Shape Motion and Deformation Measurements: Basic Concepts, Theory and Applications.* New York: Springer.

Sutton, M. A., Wolters W. J., Peters, W. H., Ranson W. F. and McNeill, S. R., 1983. Determination of displacements using an improved digital correlation method. *Image and vision computing,* 1(3), pp. 133-139.

Swaminathan, S. and Ghosh, S., 2006. Statistically Equivalent Representative Volume Elements for Unidirectional Composite Microstructures: Part II - With Interfacial Debonding. *Journal of Composite Materials,* 40(7), pp. 605-621.

Swaminathan, S., Ghosh, S. and Pagano, N., 2006. Statistically Equivalent Representative Volume Elements for Unidirectional Composite Microstructures: Part I - Without Damage. *Journal of Composite Materials,* 40(7), pp. 583-604.

Taylor, M., Ramirez, J., Charit, I., Potirniche, G. P., Stephens, R. and Glazoff, M. V., 2019. Creep behavior of Alloy 709 at 700 °C. *Materials Science and Engineering: A,* Volume 762, p. 138083.

Turner, T. J., Shade, P. A., Bernier, J. V., Li, S. F., Schuren, J. C., Lind, J., Lienert, U., Kenesei, P., Suter, R. M., Blank, B. and Almer, J., 2016. Combined near- and far-field high-energy diffraction microscopy dataset for Ti-7Al tensile specimen elastically loaded *in situ*. *Integrating Materials and Manufacturing Innovation*, Volume 5, pp. 94-102.

Upadhayay, S., Li, H., Bowen, P. and Rabiei, A., 2018. A study on tensile properties of Alloy 709 at various temperatures. *Material Science and Engineering A*, Volume 733, pp. 338-349.

van Beers, P. R. M., McShane, G. J., Kouznetsova, V. G. and Geers, M. G. D., 2013. Grain boundary interface mechanics in strain gradient crystal plasticity. *Journal of the Mechanics and Physics of Solids*, 61(12), pp. 2659-2679.

Vieira, R. B. and Lambros, J., 2021a. Measuring representative volume elements from high-resolution grain-scale strain fields. *In preparation*.

Vieira, R. B. and Lambros, J., 2021b. Machine Learning Neural-Network Predictions for Grain-Boundary Strain Accumulation in a Polycrystalline Metal. *Experimental Mechanics*, Published online 20 January 2021.

Vieira, R. B., Sehitoglu, H. and Lambros, J., 2021. Representative Volume Elements for Plasticity and Creep Measured from High-Resolution Microscale Strain Fields. *Submitted to Acta Materialia.*

Walley, J., Wheeler, R., Uchic, M. D. and Mills, M. J., 2012. Local strain accommodation in polycrystalline Ni-base superalloys. In: Proulx T. (eds) *Time Dependent Constitutive Behavior and Fracture/Failure Processes*, Volume 3. Conference Proceedings of the Society for Experimental Mechanics Series. Springer, New York, NY

Yang, S., Dirrenberger, J., Monteiro, E. and Ranc, N., 2019. Representative volume element size determination for viscoplastic properties in polycrystalline materials. *International Journal of Solids and Structures*, Volume 158, pp. 210-219.

Yi, P. C., Jiang, C. C., Dong, Z., Song, X. L., Jia, J. and Xiang, Z. D., 2019. Rationalization of Short-Term Creep Test Data and Prediction of Long-Term Creep Strengths of a Fe-20Cr-25Ni (Wt Pct) Austenitic Stainless Steel (Alloy 709). *Metallurgical and Materials Transactions A,* Volume 50, pp. 3452-3457.

Zamrick, S., Davis, D. and Firth, L., 1996. Isothermal and Thermomechanical Fatigue of Type 316 Stainless Steel. in *Thermomechanical Fatigue Behavior of Materials: Second Volume*, ed. M. Verrilli and M. Castelli (West Conshohocken, PA: ASTM International, 1996), pp. 96-116.

Zhao, Y., Zhao, J. and Li, X., 2011. Microstructural evolution and change in hardness during creep of NF709 austenitic stainless steel. *Acta Metallurgica Sinica,* 24(3), pp. 220-224.